Multidimensional Coherent Spectroscopy: Probing the Strain Tensor in Diamond and the Effects of Correlated Dephasing

by

Kelsey M. Bates

A dissertation submitted in partial fulfillment
of the requirements for the degree of
Doctor of Philosophy
(Physics)
in the University of Michigan
2024

Doctoral Committee:

> Professor Steven T. Cundiff, Chair
> Professor Paul R. Berman
> Associate Professor Parag B. Deotare
> Professor Jennifer P. Ogilvie
> Assistant Professor Christopher L. Smallwood

Kelsey M. Bates

kelseymb@umich.edu

ORCID iD: 0000-0003-2496-1124

To the little things:

To finding elusive signals

To stable lasers

To complete sets of screwdrivers

To tea time, and τ, T, and t times

To putting pixel art into LabVIEW code

To the sound that optical tables make when your hand moves quickly over the top

. . . wokka wokka wokka wokka . . .

ACKNOWLEDGEMENTS

There are many people who have helped me on this journey during the past six and a half years. It would be impractical to include everyone, but there are a few people I'd particularly like to thank.

First, I would like to thank my advisor, Steve Cundiff, for giving me the opportunity to dive deeply into this field of physics, and helping me to grow as a person and as a researcher. I'm exceptionally thankful for his direction and encouragement the many times I got stuck on a problem, as well as his flexibility when I expressed a desire to work remotely on a theory project.

I'm deeply grateful to Christopher Smallwood for his mentorship and guidance, which persisted long after he left the University of Michigan. He was always willing to give advice, both on research topics and on my professional growth. Thank you to the rest of my committee members, for their questions and feedback on this work. I'm also appreciative of Tom Schwarz, for helping me grow as a teacher and allowing me to have a voice in the design and running of a course.

I'm tremendously grateful to Matt Day, for his patience and guidance as I grew as an experimentalist. He was instrumental in teaching me about our experiment, both from a big picture and theoretical perspective, and its day-to-day operation and technological quirks. Thank you to Torben Purz, for many helpful discussions and troubleshooting suggestions, and to Grace Kerber, for being a source of advice throughout my time at Michigan. I'm additionally grateful to many other current and former members of the group, especially Adam Alfrey, Albert Liu, Allison Earnhardt, Blake Hipsley, Chris Ayala, Cesar Perez, Eric Martin, Joel Greenfield, Rachel Owen, Xiaoyan Ding, Xin Wen, and Yiming Gong for the

variety of ways in which they've helped me in the lab, and the many conversations we had outside of it at lunch or tea. It has been a pleasure working with you all.

I'm also thankful for the support that I've received outside of the lab. My board game friends, including Aidan Herderschee, Avik Mondal, Ben Sheff, Chris Dessert, Francesco Sessa, James Boggs, Jon Wang, Jordan Roth, and Karan Desai, provided a fantastic source of distraction and regular social interaction, even when the games were forced to move online. Regular video calls with Matt Sorensen, Natalie Frank, Rasika Bhalero, and Tyler Yeats, were a welcome distraction. My knitting group, the Kerrytown Crafters, was an excellent creative and social outlet. Thank you also to the many people who have worked on the Physics Graduate Council during my time at Michigan, for helping foster a friendly department climate through regular social events such as coffee hour and picnics.

I'm especially grateful to my family, for all of their love and support. Thank you to my mom, Dawn Bates, for always being willing to talk, and my dad, Kevin Casey Bates, for his many pieces of advice. Both of my parents have been instrumental in helping me grow into the person I've become, by always encouraging me to be myself and pursue what interests me most, and by instilling in me an appreciation of education and creativity. Thank you to my sister, McKenna Bates, for listening when I needed to vent, and for inspiring me to be a braver person.

Finally, I'm thankful for my partner, Will Dana, for his unceasing support and encouragement. Thank you for believing in me when I couldn't, making me laugh when I needed it, and keeping me together every time the world fell apart.

TABLE OF CONTENTS

LIST OF FIGURES

LIST OF APPENDICES

LIST OF ACRONYMS

AOM acousto-optic modulator

CVD chemical vapor deposition

CW continuous wave

FPGA field programmable gate array

HPHT high-pressure high-temperature

MDCS multidimensional coherent spectroscopy

NV nitrogen-vacancy

SiV silicon-vacancy

Ti:sapph titanium-sapphire

TMDC transition-metal dichalcogenide

TPC two-pulse correlation

ZPL zero-phonon line

ABSTRACT

This work covers two main results united by multidimensional coherent spectroscopy (MDCS): one experimental and one theoretical. MDCS is a nonlinear optical technique in which a sample is probed using a series of ultrashort pulses. Measurements are made while varying the relative time delays between the pulses, and the resulting spectra yield a much richer set of information compared to traditional linear spectroscopies.

The experimental work concerns the negatively charged silicon-vacancy (SiV) center in diamond. We use two-pulse correlation (TPC) spectroscopy and rephasing MDCS to probe a diamond sample with a high density of implanted SiV centers. These spectra reveal a large number of spectral peaks, which can be grouped into two families of SiV centers using the MDCS spectra. By comparing spectra from two polarizations of the incident light, we associate the two families with two orientation groups within the diamond.

We link the differences in the frequencies of the spectral peaks to strain intrinsic to our sample, and use the peak locations from both families to solve for the full strain tensor local to the laser spot. By measuring TPC spectra at multiple points on the sample, we track changes in the measured strain. We observe non-zero strain on the order or 1×10^{-5} at every measured location, and observe variation in both the normal and shear strain in the sample. We interpret the strain as likely to be due to the high implantation density of silicon in the diamond. These results could be useful when using SiV centers as a strain gauge.

The theoretical work uses simulations to calculate spectra. The simulations developed here begin by recursively generating a list of Feynman diagrams for a given signal pathway and system. The contributions due to each Feynman diagram are calculated and combined to find the complete spectrum. The code is designed to be very flexible, and can be used to

simulate arbitrary types of MDCS spectra and energy level diagrams.

We then apply the simulations to investigate the effects of correlated dephasing due to scattering events in the Markovian limit on MDCS of interacting systems. We derive a mathematical expression to represent the dephasing rate of a coherence in terms of the dephasing rates of the coherences from the constituent energy transitions and the correlation matrix of these transitions. This expression is applied to simulate double-quantum and higher-order n-quantum spectra of multiple interacting systems. For double-quantum spectra, correlated dephasing results in a higher double-quantum dephasing rate, and anticorrelated dephasing results in a lower double-quantum dephasing rate. Similar results are found for the n-quantum dephasing rate. Generally, for certain configurations, the many-body dephasing rate can be arbitrarily low, and the n-quantum linewidth can be arbitrarily narrow, although this requires some form of anticorrelation. These results could be useful in creating quantum sensors with higher sensitivities, since one limit of the sensitivity is the decoherence time of the system.

CHAPTER 1

Introduction

Multidimensional coherent spectroscopy (MDCS) is a nonlinear optical technique in which a series of optical pulses are sent to a sample. By varying the times between the pulses and taking appropriate Fourier transforms, we can achieve a spectrum whose intensity is measured as a function of multiple frequencies. These multidimensional spectra yield richer information compared to traditional linear spectroscopy.

I have worked on a variety of experimental projects during my doctoral work involving MDCS, some of which are documented in References [62], [5], [14], and [53]. Many of these projects concern the silicon-vacancy (SiV) center in diamond. This point defect in the diamond lattice has been the source of much scientific interest recently due to its potential use in quantum information and sensing applications [7].

The first half of this thesis will focus on one experimental result, regarding how the SiV center responds to strain within the diamond. Strain is a measure of the deformation of a material, and previous work has described how the spectrum of a SiV center changes due to sample strain [45]. My work discussed in this dissertation uses these existing strain equations to calculate the full strain tensor in our diamond [5]. We employ MDCS to aid in identifying the peaks in our spectra, since the strain occurs in multiple families of SiV centers which can be difficult to distinguish. We measure spectra at multiple points across the sample surface to asses how much the strain changes.

The second main result included in this thesis is of a theoretical nature. Consider an en-

semble of quantum oscillators, with the same initial starting state. At first, all the oscillators will be fairly synchronized. However, over time their relative phases may gradually shift, possibly due to collisions with other atoms or phonons, until all of the individual phases are effectively random. Such dephasing can be caused by Markovian scattering events, in which we assume the scattering occurs quicker than other relevant timescales in the experiment. We consider the possibility that the scattering events of different electronic states can be correlated. Correlated dephasing has been observed previously in excitons [21], but for many interacting systems, the magnitude and type of correlation may be controllable by adjusting the distance between the systems. In this work I wrote MDCS simulation software and applied it to analyze the effects of correlated dephasing on interacting systems. In particular, I found that anti-correlated dephasing can lengthen the dephasing time for certain coherences, which manifests as an arbitrarily narrow linewidth on an MDCS spectrum.

Another uniting theme of this work is quantum sensing, which is relevant to the applications of both of the main results. Quantum sensing measures a physical property using a quantum system or effect [16]. There are a wide variety of types of quantum sensors. Trapped ions can be used as highly sensitive electric and magnetic field sensors [44]. The Laser Interferometer Gravitational-Wave Observatory (LIGO) uses squeezed light to improve the sensitivity of their gravitational-wave detectors [54]. The nitrogen-vacancy (NV) center has been used to image magnetic fields of microscopic structures, such as biological cells [37]. The experimental SiV center work discussed here could be useful in using SiV centers as a strain gauge, and the work with correlated dephasing may be able to improve sensitivity of some quantum sensors.

Since it is necessary for understanding both of the main results in this thesis, Chapter 2 will focus on MDCS. This chapter will begin by outlining the theory behind the technique, and will include descriptions of some of the main types of MDCS spectra. Next we will discuss some methods used to experimentally obtain MDCS spectra, with a focus on the methods I used in the work presented here.

The next two chapters concern the experimental SiV center work. Chapter 3 provides a background on the SiV center itself. We will focus on both its physical and electronic properties, and special attention is given to previous results concerning how the SiV center responds to strain. There will also be some discussion of using MDCS to measure interactions between nearby SiV centers. Chapter 4 discusses my experimental results. This chapter will give some additional experimental details, before discussing the interpretation of the various measured spectra, and how they can be used the calculate the strain present in the diamond sample.

What follows concerns simulation and theoretical results. Chapter 5 describes some of the key simulation code used in this work. We will start with code used to generate double-sided Feynman diagrams, and later discuss how to use these diagrams to simulate the different types of MDCS spectra. The chapter will include both how to use the software, and the theory behind its implementation. Chapter 6 will discuss the correlated dephasing results. This chapter starts by building a mathematical framework to understand correlated scattering events and how they affect spectra. This is later applied to both double-quantum, and higher-order n-quantum spectra, which are types of MDCS spectra that can be used to measure interactions between multiple systems.

CHAPTER 2

Multidimensional Coherent Spectroscopy

Spectroscopy is the study of interactions between light and matter. Typically, the technique involves measuring light as a function of its wavelength or frequency, for instance by separating white light into its component colors [51]. One early success of spectroscopy was the discovery of dark lines in the spectrum of light from the sun [70, 22], which are known today to be primarily due to frequencies absorbed by elements in the sun's atmosphere. While the spectrometers of today are more sophisticated, spectroscopy still has a variety of uses, ranging from identifying compounds in a mixture [4, 2], to measuring the atmospheres of distant planets [10], to investigating the properties of novel materials [33, 74].

Two common forms of spectroscopy are absorption and photoluminescence spectroscopies. In an absorption spectrum, light is sent through a material. The spectra of the light before and after the material are compared to determine what frequencies of light were absorbed by the material. For photoluminescence spectra, light is sent to and absorbed by a material. The material may then emit its own light, called photoluminescence, and the spectrum of the emitted light is measured.

While the spectra of absorption and photoluminescence signals are often collected using a prism or (more commonly) a grating to separate light into its different frequencies, this is not the only way to measure spectra. We can alternatively measure spectra in the time domain using short optical pulses [48]. One example is a two-pulse experiment, in which the first pulse creates some sort of excitation, and the second pulse probes the response as

a function of the time delay between the two pulses. In the coherent spectroscopies used in this dissertation, we can take a Fourier transform of the data to convert a time domain spectrum into the frequency domain.

As mentioned in Chapter 1, much of this thesis will focus on MDCS, which is a nonlinear form of coherent spectroscopy [12, 61, 29, 38]. It uses a series of optical pulses (typically three or more) which interact with the quantum states in a material. Since there are multiple time delays that can be varied, we can manipulate the quantum states in a variety of ways. This gives us the ability to measure a much richer set of information than the linear spectroscopies described above. In particular, MDCS spectra can be used to differentiate between homogeneous and inhomogeneous broadening [62], identify coupling between electromagnetic transitions [5, 41], and observe interactions between nearby systems [14].

This chapter will begin by approaching MDCS from a theoretical background in Section 2.1. We will discuss how density matrices can be used to understand the nonlinear interactions occurring during a measurement, and use double-sided Feynman diagrams to represent these interactions in a more visual manner. In Section 2.2, we will use this framework to describe some common implementations of MDCS and how they are used. Finally, in Section 2.3, we will describe the experimental implementation used in this thesis, including its collinear design and available detection schemes.

2.1 Theoretic Approach

MDCS is a nonlinear optical technique. First we will define

$$E_i\left(t, \mathbf{x}\right) = \hat{E}_i\left(t\right) e^{i\mathbf{k}_i \cdot \mathbf{x} - i\omega_i t}, \tag{2.1}$$

in which a complex-valued electric field $E_i\left(t, \mathbf{x}\right)$ is described using an envelope function $\hat{E}_i\left(t\right)$, angular wave vector $\mathbf{k}_i$, position $\mathbf{x}$, angular frequency ω_i, and time t. We can then

write the electric field of a single optical pulse, distinguished by the subscript i, as

$$E_{i,\text{pulse}}(t, \mathbf{x}) = 2\hat{E}_i(t)\cos(\mathbf{k} \cdot \mathbf{x} - \omega_i t)$$

$$= \hat{E}_i(t) e^{i\mathbf{k}_i \cdot \mathbf{x} - i\omega_i t} + \hat{E}_i^*(t) e^{-i\mathbf{k}_i \cdot \mathbf{x} + i\omega_i t} \tag{2.2}$$

$$= E_i + E_i^*.$$

The most common MDCS techniques are of third-order, so we will consider the sum of three such pulses which strike a particular sample

$$E_{\text{tot}} = E_A + E_A^* + E_B + E_B^* + E_C + E_C^* \tag{2.3}$$

as well as the third-order polarization

$$P = \chi^{(1)} E_{\text{tot}} + \chi^{(2)} E_{\text{tot}}^2 + \chi^{(3)} E_{\text{tot}}^3 + \cdots . \tag{2.4}$$

If we insert Equation 2.3 into Equation 2.4, we will get a variety of third-order terms. In a typical MDCS experiment, we will attempt to isolate a single one of these terms, and the isolated term typically includes contributions from each optical pulse [39]. For example, consider one such term

$$E_A^* E_B E_C \propto e^{-i\mathbf{k}_A \cdot \mathbf{x} + i\omega_A t} e^{i\mathbf{k}_B \cdot \mathbf{x} - i\omega_B t} e^{i\mathbf{k}_C \cdot \mathbf{x} - i\omega_C t}$$

$$= e^{i(-\mathbf{k}_A + \mathbf{k}_B + \mathbf{k}_C) \cdot \mathbf{x}} e^{-i(-\omega_A + \omega_B + \omega_C)t}. \tag{2.5}$$

This equation shows the direction $(-\mathbf{k}_A + \mathbf{k}_B + \mathbf{k}_C)$ and frequency $(-\omega_A + \omega_B + \omega_C)$ of the emitted four wave mixing signal. Note that both the direction and frequency are dependent on the conjugation of the pulses used (i.e. E_A vs. E_A^*). This particular signal pathway is used when measuring rephasing spectra, which is the most commonly used form of MDCS. A variety of other signal pathways can be used, as will be described in Section 2.2.

The arrival time of each optical pulse in an MDCS experiment can be varied. We will

define τ as the time between pulses A and B, T as the time between pulses B and C, and t as the time between either a local oscillator or a fourth pulse D, depending on the type of detection used, as described in Section 2.3.2.

To measure a MDCS spectrum, we will vary several (typically two) of the time delays, and then Fourier transform with respect to these time delays to get data in terms of several frequencies. Figure 2.1 shows an example spectrum, both in the time-domain and Fourier transformed frequency-domain. The main power of MDCS lies in its ability to relate several frequencies contributing to a given signal in a single plot.

However, before investigating the different types of MDCS spectra in more detail, we will find it useful to better understand the density matrix and how it can be used to represent nonlinear interactions.
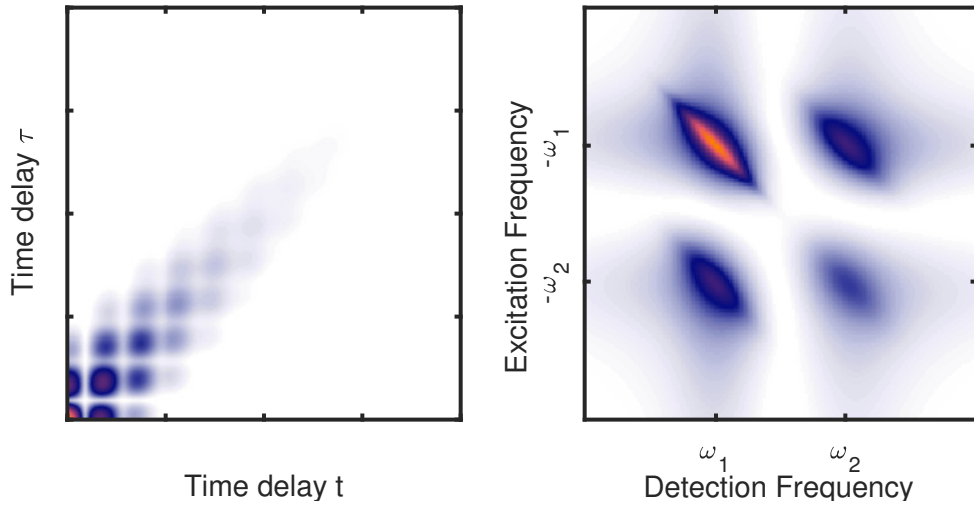
Figure 2.1: A sample MDCS spectrum, with magnitudes plotted in both the time and frequency domains.

2.1.1 Density Matrix

The density operator allows us to represent a quantum ensemble with known statistics. If we have quantum states $|\psi_i\rangle$ which occur with fractional populations or probabilities w_i, then

the density operator is defined as [58, pgs. 180-184]

$$\rho = \sum_i w_i \left| \psi_i \right\rangle \left\langle \psi_i \right|. \tag{2.6}$$

It will be useful to represent the density operator as a matrix. Assume the system Hamiltonian H_0 has eigenvectors $\left| a \right\rangle$, and write $\left| \psi_i \right\rangle$ in this basis as

$$\left| \psi_i \right\rangle = \sum_a c_a \left| a \right\rangle. \tag{2.7}$$

Thus we see that

$$\rho = \sum_{i,a,b} w_i c_a c_b^* \left| a \right\rangle \left\langle b \right|. \tag{2.8}$$

For this basis, the matrix elements can be found using

$$\rho_{a,b} = \left\langle a \right| \rho \left| b \right\rangle = \sum_i w_i c_a c_b^*. \tag{2.9}$$

As a more concrete example, consider an ensemble of two-level systems where each system has basis states $\left| 0 \right\rangle = \left(\begin{smallmatrix} 1 \\ 0 \end{smallmatrix} \right)$ and $\left| 1 \right\rangle = \left(\begin{smallmatrix} 0 \\ 1 \end{smallmatrix} \right)$. If all systems in our ensemble are in the ground $\left| 0 \right\rangle$ state, we can represent the system with the density matrix

$$\rho = \left| 0 \right\rangle \left\langle 0 \right| = \begin{pmatrix} 1 \\ 0 \end{pmatrix} \begin{pmatrix} 1 & 0 \end{pmatrix} = \begin{pmatrix} 1 & 0 \\ 0 & 0 \end{pmatrix}, \tag{2.10}$$

and if all systems in our ensemble are in the excited $\left| 1 \right\rangle$ state, we can represent the system with the density matrix

$$\rho = \left| 1 \right\rangle \left\langle 1 \right| = \begin{pmatrix} 0 \\ 1 \end{pmatrix} \begin{pmatrix} 0 & 1 \end{pmatrix} = \begin{pmatrix} 0 & 0 \\ 0 & 1 \end{pmatrix}. \tag{2.11}$$

These are called pure states, since all systems in our ensemble have the same state. If half of

the systems in our ensemble are in the ground state, and half are in the excited state, then we have

$$\rho = \frac{1}{2} \left| 0 \right\rangle \left\langle 0 \right| + \frac{1}{2} \left| 1 \right\rangle \left\langle 1 \right| = \begin{pmatrix} \frac{1}{2} & 0 \\ 0 & 0 \end{pmatrix} + \begin{pmatrix} 0 & 0 \\ 0 & \frac{1}{2} \end{pmatrix} = \begin{pmatrix} \frac{1}{2} & 0 \\ 0 & \frac{1}{2} \end{pmatrix}, \tag{2.12}$$

which is a mixed state, since there are multiple states represented among the different systems. Note that all of the density matrices shown so far are diagonal, since the only states represented have been energy eigenstates. However, consider instead that all systems in our ensemble are identical superpositions of the ground and excited state. Then we have

$$\rho = \left(\frac{1}{\sqrt{2}} \left(\left| 0 \right\rangle + \left| 1 \right\rangle \right) \right) \left(\frac{1}{\sqrt{2}} \left(\left\langle 0 \right| + \left\langle 1 \right| \right) \right) = \begin{pmatrix} \frac{1}{\sqrt{2}} \\ \frac{1}{\sqrt{2}} \end{pmatrix} \begin{pmatrix} \frac{1}{\sqrt{2}} & \frac{1}{\sqrt{2}} \end{pmatrix} = \begin{pmatrix} \frac{1}{2} & \frac{1}{2} \\ \frac{1}{2} & \frac{1}{2} \end{pmatrix}. \tag{2.13}$$

This is a pure state, since all systems in the ensemble have the same state, namely $\frac{1}{\sqrt{2}} \left(\left| 0 \right\rangle + \left| 1 \right\rangle \right)$. However, we also see that this density matrix has nonzero off-diagonal elements due to the eigenstate superposition.

We will want to observe how the density matrix evolves with time during a MDCS experiment. Using the Schrödinger equation, we see that, for a general Hamiltonian H,

$$\begin{aligned} \frac{\partial \rho}{\partial t} &= \frac{\partial}{\partial t} \sum_i w_i \left| \psi_i \right\rangle \left\langle \psi_i \right| \\ &= \sum_i w_i \left(\left(\frac{\partial}{\partial t} \left| \psi_i \right\rangle \right) \left\langle \psi_i \right| + \left| \psi_i \right\rangle \left(\frac{\partial}{\partial t} \left\langle \psi_i \right| \right) \right) \\ &= \sum_i w_i \left(\frac{H}{i\hbar} \left| \psi_i \right\rangle \left\langle \psi_i \right| - \left| \psi_i \right\rangle \left\langle \psi_i \right| \frac{H}{i\hbar} \right) \\ &= \frac{1}{i\hbar} \left(H \sum_i w_i \left| \psi_i \right\rangle \left\langle \psi_i \right| - \sum_i w_i \left| \psi_i \right\rangle \left\langle \psi_i \right| H \right) \\ &= \frac{1}{i\hbar} \left(H\rho - \rho H \right) \\ &= -\frac{i}{\hbar} \left[H, \rho \right] \\ \frac{\partial \rho_{a,b}}{\partial t} &= -\frac{i}{\hbar} \left[H, \rho \right]_{a,b}. \end{aligned} \tag{2.14}$$

9

This is known as the Liouville-von Neumann equation [29, eq. 3.20]. Note that we have made the assumption that the w_i terms do not vary over time. However, certain processes can cause $\rho_{a,b}$ to decay. To account for this, we will add a term to our equation [29, eqs. 3.26, 29]

$$\frac{\partial \rho_{a,b}}{\partial t} = -\frac{i}{\hbar} [H, \rho]_{a,b} - \gamma_{a,b} \rho_{a,b}, \tag{2.15}$$

where $\gamma_{a,b}$ represents the rate of decay or dephasing.

Next we will rewrite H as the sum of the system Hamiltonian H_0, and the interaction with the electric field $V(t)$ to get

$$H = H_0 + V(t). \tag{2.16}$$

Substituting this into Equation 2.15 gives [29, eq. 3.29]

$$\frac{\partial \rho_{a,b}}{\partial t} = -\frac{i}{\hbar} [H_0, \rho]_{a,b} - \frac{i}{\hbar} [V(t), \rho]_{a,b} - \gamma_{a,b} \rho_{a,b}. \tag{2.17}$$

For the first term, since $|a\rangle$ and $|b\rangle$ are eigenvectors, we see that

$$
\begin{aligned}
[H_0, |a\rangle \langle b|] &= H_0 |a\rangle \langle b| - |a\rangle \langle b| H_0 \\
&= E_a |a\rangle \langle b| - |a\rangle \langle b| E_b \\
&= (E_a - E_b) |a\rangle \langle b|,
\end{aligned} \tag{2.18}
$$

where E_a and E_b are the eigenenergies, thus

$$[H_0, \rho]_{a,b} = \rho_{a,b} (E_a - E_b). \tag{2.19}$$

To represent a nonlinear process, we will use perturbation theory to write $\rho = \rho^{(0)} + \rho^{(1)} + \rho^{(2)} + \rho^{(3)} + \cdots$. Here, $\rho^{(0)}$ is the initial state of the system (which we will assume is diagonal and does not contain any coherences), and each successive $\rho^{(n)}$ corresponds to

another interaction with the electric field. For instance,

$$\frac{\partial \rho_{a,b}^{(1)}}{\partial t} = -\frac{i}{\hbar} \left(E_a - E_b \right) \rho_{a,b}^{(1)} - \gamma \rho_{a,b}^{(1)} - \frac{i}{\hbar} \left[V\left(t \right), \rho^{(0)} \right]_{a,b}, \tag{2.20}$$

or more generally [38, eq. 2.4]

$$\frac{\partial \rho_{a,b}^{(n)}}{\partial t} = -\frac{i}{\hbar} \left(E_a - E_b \right) \rho_{a,b}^{(n)} - \gamma \rho_{a,b}^{(n)} - \frac{i}{\hbar} \left[V\left(t \right), \rho^{(n-1)} \right]_{a,b}, \tag{2.21}$$

If we define

$$\omega_{a,b} = \frac{E_a - E_b}{\hbar},$$

$$\Omega_{a,b} = \omega_{a,b} - i\gamma_{a,b}, \tag{2.22}$$

we can rewrite this as

$$\frac{\partial \rho_{a,b}^{(n)}}{\partial t} = -i\Omega_{a,b} \rho_{a,b}^{(n)} - \frac{i}{\hbar} \left[V\left(t \right), \rho^{(n-1)} \right]_{a,b}. \tag{2.23}$$

This differential equation can be solved for $\rho_{a,b}^{(n)}$ as [38, eq. 2.7]

$$\rho_{a,b}^{(n)} \left(t \right) = \int_{-\infty}^{t} -\frac{i}{\hbar} \left[V\left(t' \right), \rho^{(n-1)} \right]_{a,b} e^{-i\Omega_{a,b}(t-t')} \, dt'. \tag{2.24}$$

The electric field due to all pulses interaction can be written using the field as defined in Equation 2.2

$$V\left(t \right) = -\mu \sum_i E_{i,\text{pulse}} \left(t, \mathbf{x} \right) = -\mu \sum_i \left(\hat{E}_i \left(t \right) e^{i\mathbf{k}_i \cdot \mathbf{x} - i\omega_i t} + \hat{E}_i^* \left(t \right) e^{-i\mathbf{k}_i \cdot \mathbf{x} + i\omega_i t} \right). \tag{2.25}$$

The transition dipole operator μ is an off-diagonal matrix, that is, all of its diagonal elements are zero. This means that to find $\left[\mu, \rho^{(n-1)} \right]_{a,b}$, we need elements of $\rho^{(n-1)}$ other than $\rho_{a,b}^{(n-1)}$. If we divide the commutator into its two terms, we also see that $\left(\mu \rho^{(n-1)} \right)_{a,b}$ depends on the

11

bth column of $\rho^{(n-1)}$, and $\left(-\rho^{(n-1)}\mu\right)_{a,b}$ depends on the ath row of $\rho^{(n-1)}$.

Looking at Equation 2.24, we see that if we know our starting state $\rho^{(0)}$, we can apply the equation repeatedly until we reach $\rho^{(n)}$, which is the state of the density matrix after the nth interaction with the electric field, which occurs at time t'. After each interaction, the system can evolve according to $e^{-i\Omega_{a,b}(t-t')}$ until time t.

However, with each iteration of Equation 2.24, the number of terms in our expression increases. Each application corresponds to another interaction between an optical pulse and our sample, and each interaction could be due to one of many pulses, and either conjugation of a given pulse. Furthermore, each application of the commutator $\left[\mu, \rho^{(n-1)}\right]$ can have two terms, $\mu\rho^{(n-1)}$ and $-\rho^{(n-1)}\mu$, and the electronic structure of the measured system can also add additional complexity.

Fortunately, in a given experiment, we do not typically have to worry about each of these terms. Some terms can be removed due to time ordering, i.e. if pulse A impinges on the sample first, it cannot interact after pulse B does. Often we assume that each pulse acts once. We can also isolate a given signal pathway, such as in the example described in Equation 2.5, which constrains the possible pulse conjugations.

2.1.2 Feynman Diagrams

To tabulate the terms that contribute in a given experiment, we will find it useful to use double-sided Feynman diagrams [48, 29]. These show how each interaction affects the density matrix, and depict the possible states of the system at each step of the experiment.

To motivate double-sided Feynman diagrams, we will revisit Equation 2.24. We will simplify the notation by assuming the interaction term is due to a single predetermined pulse $E_n + E_n^*$, instead of writing the full summation from Equation 2.25. We first need to

deal with the commutator

$$\left[V\left(t'\right),\rho^{(n-1)}\right]_{a,b} = -\left[\mu,\rho^{(n-1)}\right]_{a,b}\left(\hat{E}_n\left(t\right)e^{i\mathbf{k}_n\cdot\mathbf{x}-i\omega_n t}+\hat{E}_n^*\left(t\right)e^{-i\mathbf{k}_n\cdot\mathbf{x}+i\omega_n t}\right)$$

$$= -\left(\left(\mu\rho^{(n-1)}\right)_{a,b}-\left(\rho^{(n-1)}\mu\right)_{a,b}\right)$$

$$\left(\hat{E}_n\left(t\right)e^{i\mathbf{k}_n\cdot\mathbf{x}-i\omega_n t}+\hat{E}_n^*\left(t\right)e^{-i\mathbf{k}_n\cdot\mathbf{x}+i\omega_n t}\right) \quad (2.26)$$

$$= -\left(\sum_c \mu_{a,c}\rho_{c,b}^{(n-1)}-\sum_c \rho_{a,c}^{(n-1)}\mu_{c,b}\right)$$

$$\left(\hat{E}_n\left(t\right)e^{i\mathbf{k}_n\cdot\mathbf{x}-i\omega_n t}+\hat{E}_n^*\left(t\right)e^{-i\mathbf{k}_n\cdot\mathbf{x}+i\omega_n t}\right).$$

Each term of this equation will correspond to a different Feynman diagram, d. If we sum over all the individual $\rho_{a,b;d}^{(n)}$, we should recover $\rho_{a,b}^{(n)}$. Each Feynman diagram will show one of the sets of density matrix elements $\rho_{a',b'}^{(m)}$, where $m < n$, that contribute to a final state $\rho_{a,b}^{(n)}$.

A double-sided Feynman diagram consists of rows of density matrix elements with arrows pointing toward and away from the center. The bottom row represents the initial state of the system, $|k_0\rangle\langle b_0|$ and each subsequent row, $|k_n\rangle\langle b_n|$, represents the system at a later time, or after the nth interaction. Each arrow represents an electric field interaction, which occur between adjacent density matrix element rows. There are several rules used to build Feynman diagrams, which are described as follows and illustrated in Figure 2.2.

First we will look at the two terms of the commutator $\left[\mu,\rho^{(n-1)}\right]$, which we will represent by $\zeta_{n,d}$. If μ acts on the left, as in $\mu\rho^{(n-1)}$, then the interaction arrow will be on the left side
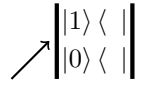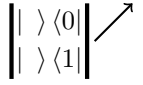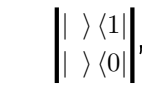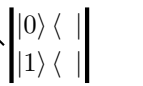
		Excitation	De-excitation
E_n		$\nearrow \begin{Vmatrix}|1\rangle\langle\;|\\|0\rangle\langle\;|\end{Vmatrix}$	$\begin{Vmatrix}|\;\rangle\langle 0|\\|\;\rangle\langle 1|\end{Vmatrix}\nearrow$
		$\eta=1,\zeta=1$	$\eta=1,\zeta=-1$
E_n^*		$\begin{Vmatrix}|\;\rangle\langle 1|\\|\;\rangle\langle 0|\end{Vmatrix}\searrow$	$\searrow\begin{Vmatrix}|0\rangle\langle\;|\\|1\rangle\langle\;|\end{Vmatrix}$
		$\eta=-1,\zeta=-1$	$\eta=-1,\zeta=1$

Figure 2.2: A table showing the four possible interactions that can occur in double-sided Feynman diagrams, and how they would affect the density matrix elements.

of the Feynman diagram, and $\zeta_{n,d} = 1$. Looking at Equation 2.26, we see that the row of the relevant density matrix element changes, and the column stays the same, so $k_{n-1} \neq k_n$ and $b_{n-1} = b_n$. If μ acts on the right, as in $-\rho^{(n-1)}\mu$, then the interaction arrow will be on the right side of the Feynman diagram, and $\zeta_{n,d} = -1$. Similarly, we see that the column of the relevant density matrix element changes, and the row stays the same, so $b_{n-1} \neq b_n$ and $k_{n-1} = k_n$.

Next we have the two conjugations of the pulse, $E_n = \hat{E}_n(t) e^{-i\mathbf{k}_n \cdot \mathbf{x} + i\omega_n t}$ and $E_n^* = \hat{E}_n^*(t) e^{i\mathbf{k}_n \cdot \mathbf{x} - i\omega_n t}$, which we will represent by $\eta_{n,d}$. On the Feynman diagram, the pulse conjugation is represented by the direction that the arrow is pointing. If the unconjugated pulse E_n is used, then the arrow is pointed to the right ($\nearrow$) and $\eta_{n,d} = 1$, and if the conjugated pulse E_n^* is used, then the arrow is pointed to the left ($\nwarrow$) and $\eta_{n,d} = -1$.

We can use the variables we have defined here to relate an individual Feynman diagrams back to a term of Equation 2.24. As previously stated, after n interactions, the relevant density matrix element of a Feynman diagram d is $|k_n\rangle \langle b_n|$, which we can represent as $\rho_{k_n,b_n;d}^{(n)}$. We will also use our definitions for $\zeta_{n,d}$ and $\eta_{n,d}$. Putting all of this together with the results of Equation 2.26, we get [38, eqs. 2.10-2.13]

$$\rho_{k_n,b_n;d}^{(n)}(t) = \zeta_{n,d} \frac{i\mu_{\zeta_{n,d}}}{\hbar} e^{i\eta_{n,d}\mathbf{k}_n \cdot \mathbf{x}} \int_{-\infty}^{t} \hat{E}_n^{\eta_{n,d}}(t') e^{-i\eta_{n,d}\omega_n t'} e^{-i\Omega_{k_n,b_n}(t-t')} \rho_{k_{n-1},b_{n-1},d}^{(n-1)}(t') \, dt',$$

(2.27)

where if $\zeta_{n,d} = 1$, then $\mu_{\zeta_{n,d}} = \mu_{k_n,k_{n-1}}$, and if $\zeta_{n,d} = -1$, then $\mu_{\zeta_{n,d}} = \mu_{b_{n-1},b_n}$, and $\hat{E}_n^{\eta_{n,d}}$ corresponds to $\hat{E}_n$ for $\eta_{n,d} = 1$ and $\hat{E}_n^*$ for $\eta_{n,d} = -1$.

The next rule for Feynman diagram formation is a consequence of the rotating wave approximation. Essentially, if the interaction arrow is pointing toward the center of the Feynman diagram, then that side of the density matrix element will be excited, or moved to a higher energy state. If the arrow is pointing away from the center of the Feynman diagram, then that side of the density matrix element will be de-excited, or moved to a lower energy state.

Finally, the last interaction arrow of a Feynman diagram often represents the emitted coherent third-order (or more generally odd-order) signal. In this case, the last interaction arrow is drawn with a wavy arrow pointing away from the Feynman diagram. This signal is only emitted if the final density matrix element of the Feynman diagram has the same state for the ket and the bra, so $k_n = b_n$. The emitted electric field is proportional to [38, eqns. 2.17-19]

$$E_d^{(n)}(t) \propto -\zeta_{n,d}\frac{\partial}{\partial t}\mu_{\zeta_{n,d}}\rho_{k_{n-1},b_{n-1};d}^{(n)}(t).$$ (2.28)

Alternatively, the signal can be measured using an incoherent fourth-order (or more generally even-order) signal, in this thesis from the photoluminescence due to a decaying population state. After a final fourth optical pulse, the system must be in a population state, such that $k_n = b_n$ are in the same excited state. Here, the emitted intensity is proportional to $\rho_{k_n,b_n;d}^{(n)}(t)$. This will be discussed further in Section 2.3.2.

2.2 Varieties of MDCS Spectra

Next we will apply Feynman diagrams to a variety of spectra. Through this we can see how Feynman diagrams are used in practice, and observe the diverse uses of MDCS spectra.

2.2.1 Two-Pulse Spectra

Two-pulse correlation (TPC) spectra are useful as a simple example to start with, but also have experimental utility [5], as will be shown in Chapter 4. Consider a single pulse incident on a two-level system, with states $|0\rangle$ and $|1\rangle$, as shown in Figure 2.3 (a). Since we are working with a single pulse impinging on the sample, this is a linear measurement. We will look for the signal that propagates in the same direction as the laser, so the interaction due to the first pulse is unconjugated (E_A).

The pulse sequence as well as a visual depiction of the system at each step of the sequence is shown in Figure 2.3 (b), and the corresponding Feynman diagram is shown in Figure 2.3
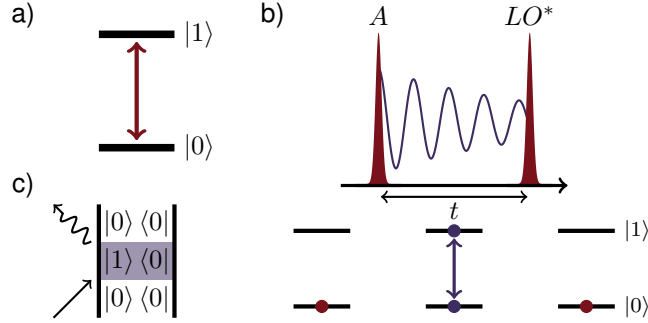
Figure 2.3: (a) The energy level diagram of a two-level system. (b) A TPC pulse sequence. (c) The corresponding double-sided Feynman diagram.

(c). Before the pulse arrives, the system starts out in the ground state, so the first row of the Feynman diagram is $|0\rangle \langle 0|$.

Since the system starts out in the ground state, the first pulse interaction should be an excitation, and we also know that the pulse is unconjugated. Referring to Figure 2.2, we see that this first interaction must be on the left side, and should point toward the center of the Feynman diagram, which is what is shown in Figure 2.3 (c). Due to the excitation on the left side, the second row of the Feynman diagram is forced to be $|1\rangle \langle 0|$. Thus, the pulse will drive the system into a coherent superposition between the ground and excited states, as depicted in the bottom of Figure 2.3 (b).

Lastly, we have the emitted signal, which is depicted with a wavy arrow in the Feynman diagram. We know that this emission arrow must point away from the diagram, so it corresponds to a de-excitation. Since the ket $|1\rangle$ is excited and the bra $\langle 0|$ is not, this de-excitation must occur from the left, as is shown in Figure 2.3 (c). It will also bring the system back to the ground state $|0\rangle \langle 0|$.

Notably, a second pulse is shown in Figure 2.3 (b). Here, it is labeled as a local oscillator, meaning it does not interact with the sample, but instead interferes with the emitted signal to enable heterodyne detection. Unfortunately, it will also interfere with pulse A, which is likely stronger than the emitted signal from the sample, making it difficult to detect the sample response. The TPC spectra in Chapter 4 were taken using photoluminescence detection,

which makes it easier to filter out the incident laser. The differences between the different detection schemes will be explored in Section 2.3.2.

2.2.2   Rephasing Spectra

The most common type of MDCS spectrum is the rephasing spectrum. This uses the same third-order pathway described in Equation 2.5, namely $E_A^* E_B E_C$, so the first pulse has the opposite conjugation of the second two pulses [61].

The pulse sequence is shown in Figure 2.4 (a), which is depicted here using an example two-level system. Initially, the system starts out in the ground state. The first pulse A^* will create a coherent superposition between the ground and excited states. The second pulse will create a population, here in the excited state. The third pulse will create another coherent superposition between the ground and excited states. Lastly, the final interaction is the emission, which brings the system back to the ground state, and is probed with a heterodyne pulse which is assumed to not interact with the sample.

This qualitative picture is useful to conceptualize the rephasing pulse sequence, but several details are better explained using the corresponding Feynman diagram, which is shown in Figure 2.4 (b). The Feynman diagram is also color coded for each of the time delays in the pulse sequence. Again, the system starts in the ground state, or $|0\rangle \langle 0|$. Using similar logic to
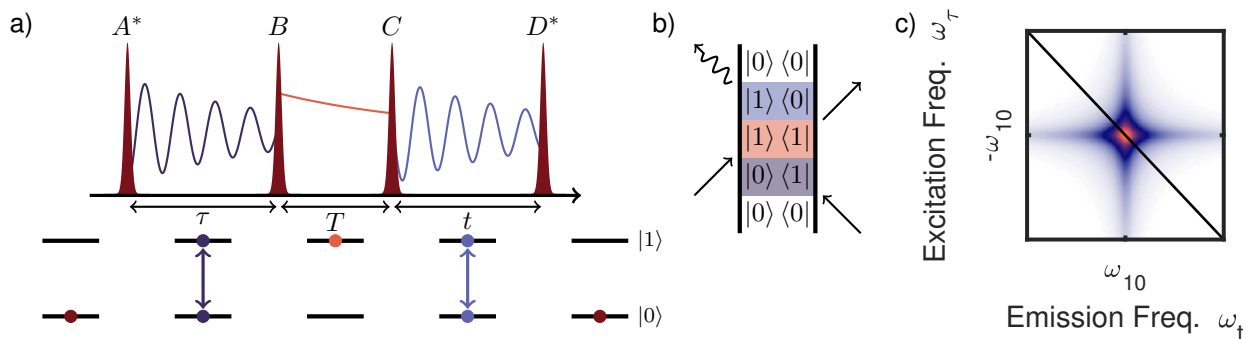
Figure 2.4: (a) A pulse sequence for a rephasing spectrum. (b) The corresponding double-sided Feynman diagram. (c) The rephasing spectrum for this system, where the magnitudes of the complex valued data are plotted.

the two pulse case, the first interaction is an excitation from the right, putting the system in the state $|0\rangle\langle 1|$, which is the first superposition state. For the second interaction, we actually have a choice. Since the pulse is un-conjugated, we know that the interaction arrow must point to the right. However, this could be an excitation from the left with corresponding state $|1\rangle\langle 1|$, or a de-excitation to the right with corresponding state $|0\rangle\langle 0|$. The Feynman diagram shown here chooses the former, but the latter choice is also associated with a valid Feynman diagram. Moving on, the third interaction is forced to be a de-excitation from the right, putting the system in the state $|1\rangle\langle 0|$. Lastly, we have the arrow corresponding to emission, where that emission can again be measured using heterodyne detection.

For a rephasing spectrum, we measure data as a function of the time delays τ and t, and take a Fourier transform of the data with respect to these time delays to get a spectrum, such as that in Figure 2.4 (c). Since the state during the τ time delay is $|0\rangle\langle 1|$, according to Equation 2.27, this state evolves as $e^{-i\Omega_{01}\tau} = e^{-i\omega_{01}\tau - \gamma_{01}\tau}$. Thus, the vertical ω_τ axis probes this evolution. Similarly, the state during the t time delay is $|1\rangle\langle 0|$, which evolves as $e^{-i\Omega_{10}t} = e^{-i\omega_{10}t - \gamma_{10}t}$, and the horizontal ω_t axis probes this evolution. Note that $\gamma_{10} = \gamma_{01}$, so the dephasing rate is the same during both time delays. However, by Equation , $\omega_{10} = -\omega_{01}$, so the phase evolution during these two time delays is opposite. Thus, we will take the convention that the vertical ω_τ axis is negative, so the diagonal for which the excitation and emission frequencies are equal is the downward sloping diagonal depicted with a black line in Figure 2.4 (c).

One consequence of this is the ability to distinguish between homogeneous and inhomogeneous broadening [39]. The homogeneous linewidth is the width of the spectral peak of a single system, and for our two-level system, this is determined by γ_{10}. The inhomogeneous linewidth is the width of a spectral peak of an ensemble of systems. An ensemble is inhomogeneously broadened if the inhomogeneous linewidth is larger than the homogeneous linewidth. One example of inhomogeneous broadening is Doppler broadening in a gas. Each molecule of a specific gas has a very similar homogeneous linewidth. However, when we ob-
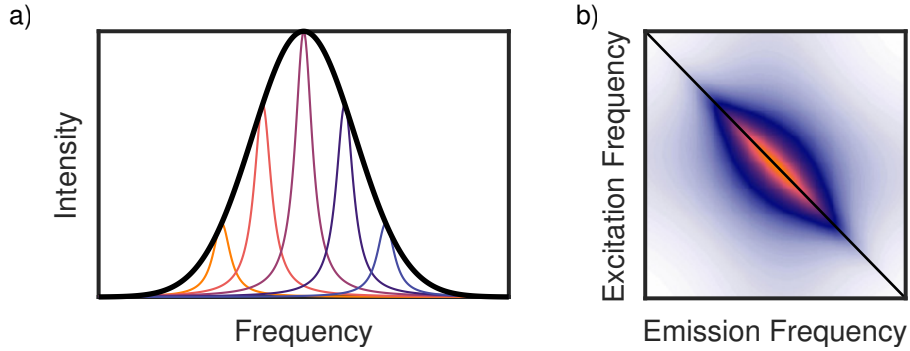
Figure 2.5: (a) An inhomogeneously broadened 1D spectrum. (b) An inhomogeneously broadened 2D spectrum

serve an ensemble, some molecules are moving toward us and others are moving away from us, causing their frequencies to shift up or down, respectively. This makes the spectrum of the ensemble much broader than the spectrum of individual molecules, as is shown in Figure 2.5 (a). Here, the homogeneous linewidth is the width of one of the colored curves, and the inhomogeneous linewidth is the width of the black curve.

Now consider the rephasing spectrum of an inhomogeneously broadened ensemble. As before, the evolution during time τ is $e^{i\omega_{10}t-\gamma_{10}\tau}$, and the evolution during time t is $e^{-i\omega_{10}t-\gamma_{10}t}$. Each system in our inhomogeneously broadened ensemble will have a slightly different value for ω_{10}, so during the τ time delay the different systems will become out of phase with respect to each other. However, due to the pulse conjugation and the resulting sign difference in the phase evolution, during the t time delay this process will reverse and the systems will be brought back in phase with each other. Thus, a strong signal can be measured for $\tau \approx t$, even in the presence of strong inhomogeneity. This signal is often referred to as a photon echo [1]. Note that inhomogeneous broadening behaves differently compared to the homogeneous dephasing γ_{10}, which cannot be reversed in this manner. We can obtain both linewidths from a single rephasing spectrum in the frequency domain, as the inhomogeneous linewidth is the width along the downward sloping, or main diagonal, and the heterogeneous linewidth is the width along the upward sloping, or cross diagonal.

To better understand rephasing spectra, we will now consider the V-shaped three-level
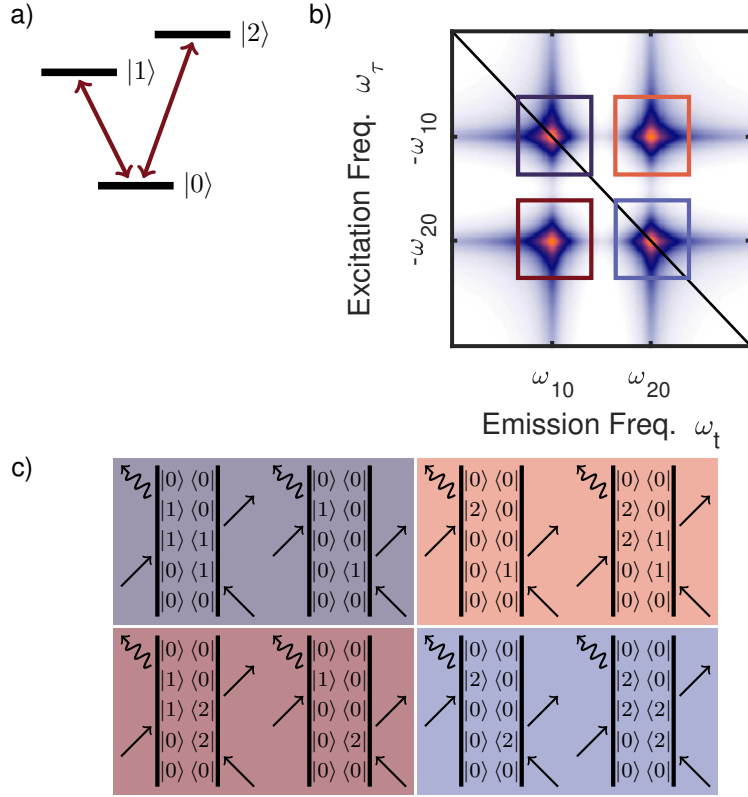
Figure 2.6: (a) The energy level diagram of a V-shaped three-level system. (b) The rephasing spectrum for this system. (c) The Feynman diagrams corresponding to this spectrum.

system shown in Figure 2.6 (a). We see that the corresponding spectrum in Figure 2.6 has a total of four peaks, which follow directly from the Feynman diagrams in Figure 2.6 (c). Each Feynman diagram will contribute to one of the peaks in the spectrum, where the excitation frequency ω_τ corresponds to the state during the τ time delay, and the emission frequency ω_t corresponds to the state during the t time delay. The two peaks on the main (downward sloping) diagonal are due to the Feynman diagrams where the τ and t coherences are between the same two states. For this V-shaped three-level system, that means only one of the excited states, $|1\rangle$ or $|2\rangle$, contributes. The remaining off-diagonal peaks are due to the Feynman diagrams where the τ and t coherences are between different sets of states, so both excited states must contribute.

These off-diagonal peaks only occur when the two relevant electronic transitions are coupled [39], which for the system in Figure 2.6 is achieved by having a shared ground state. If

the energy level diagram instead consisted of two disjoint two level systems, the off-diagonal peaks in Figure 2.6 would be absent, and only the two on-diagonal peaks would remain. This makes MDCS particularly useful in untangling complicated spectra by identifying which electronic transitions are coupled. This will be used in Chapter 4 to better understand spectra of several families of SiV centers.

2.2.3 Zero-Quantum Spectra

One may notice by inspecting Figure 2.6 (c) that some of the Feynman diagrams contain a coherence during the T delay. These coherences cannot be probed using a single rephasing spectrum, although sometimes a series of rephasing spectra are taken at different T time delays do so, forming a sort of three-dimensional spectrum. One alternate option is to use a single two-dimensional zero-quantum spectrum.

Zero-quantum spectra use the same third-order pathway $E_A^* E_B E_C$ as rephasing spectra, so the pulse sequence is the same as that of Figure 2.4 (a). However, while the time delays varied for rephasing spectra are τ and t, the time delays varied for zero-quantum spectra are T and t [61].

Since the third-order pathway for zero-quantum spectra is the same as for rephasing spectra, the Feynman diagrams are also the same. Figure 2.7 (a) shows a zero-quantum spectrum for the V-shaped three-level system depicted in Figure 2.6 (a), and Figure 2.7 (b) reproduces the Feynman diagrams from Figure 2.6 (c). We can again associate the different Feynman diagrams to different peaks in the spectrum. The emission frequency ω_t is determined by the state during the t time delay, as before. The mixing frequency ω_T therefore corresponds to the state during the T time delay. Since most Feynman diagrams have a population state during the T time delay ($|0\rangle \langle 0|$, $|1\rangle \langle 1|$, or $|2\rangle \langle 2|$), the mixing frequency is simply zero. However, two of the diagrams have coherences during the T time delay, $|2\rangle \langle 1|$ and $|1\rangle \langle 2|$, which manifests as two peaks with nonzero mixing frequencies, ω_{21} and $\omega_{12} = -\omega_{21}$.

These coherences are sometimes referred to as zero-quantum coherences, since the states in the coherence are zero quanta apart. Here, both states in the coherence are excited states, but zero-quantum spectra can also be used to probe split ground states. We can similarly use the term single-quantum coherence to describe the coherences probed during the t time delay of zero-quantum spectra, or during the τ and t time delays of rephasing spectra.
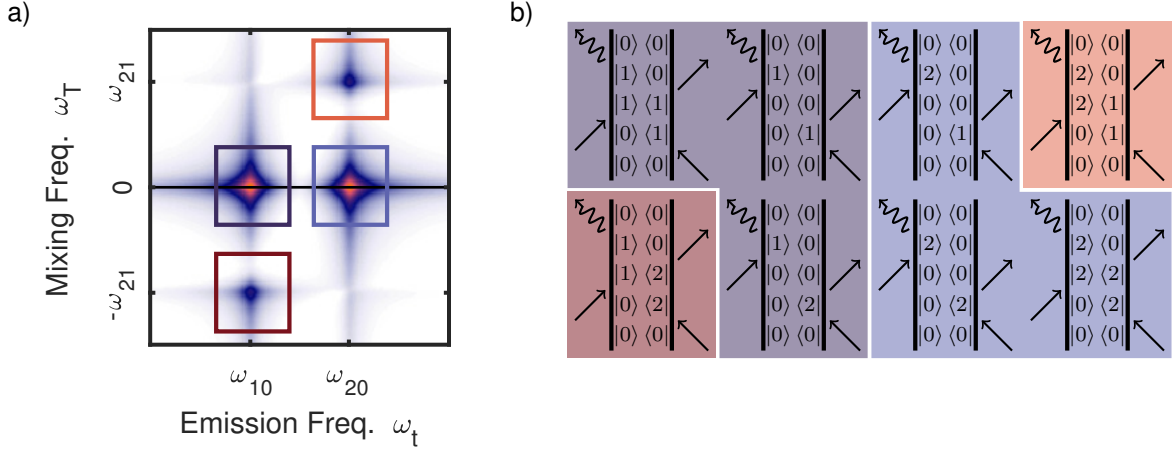
Figure 2.7: (a) The zero-quantum spectrum for the V-shaped three-level system in Figure 2.6 (a). (b) The Feynman diagrams corresponding to this spectrum.

2.2.4   Double-Quantum Spectra

The third type of MDCS spectra we will discuss is double-quantum spectra, which is predictably used to probe double-quantum coherences. This uses a different third-order pathway, specifically $E_A E_B E_C^*$, and the varied time delays in this case are T and t [61, 71].

To investigate double-quantum spectra, we will require a doubly excited state, so we will use the three-level system depicted in Figure 2.8 (a). The double-quantum pulse sequence is shown in Figure 2.8 (b), and the possible Feynman diagrams are shown in Figure 2.8 (c). As before, the system will start in the ground state. The first two pulses are both unconjugated, so according to Figure 2.2 they must either be an excitation to the left, or a de-excitation from the right. Since the bra $\langle 0|$ is in the ground state, the first pulse must be an excitation from the left, and since this interaction does not affect the bra, the second
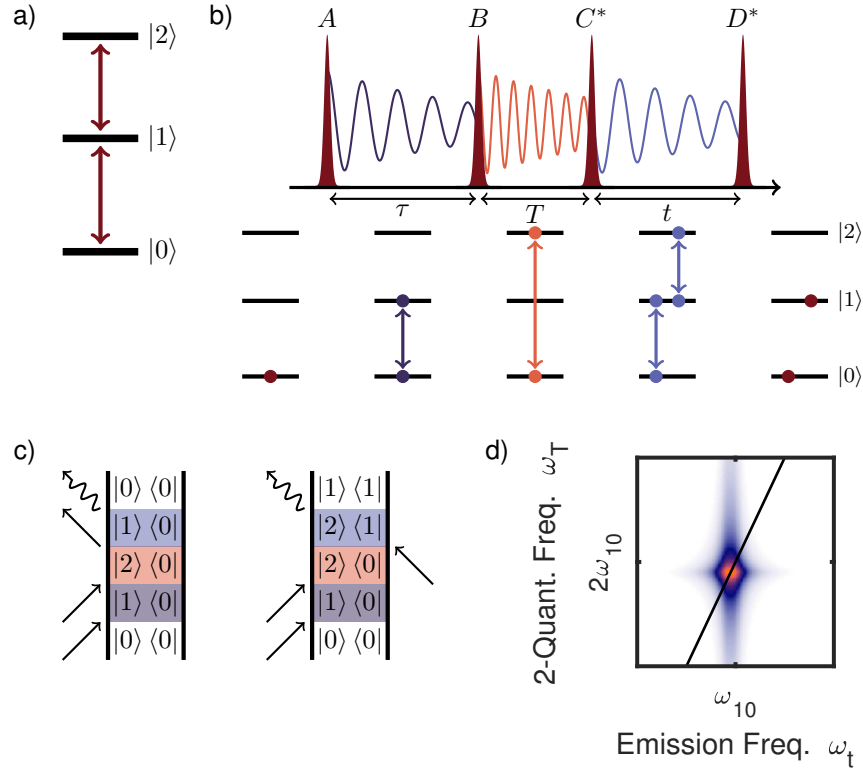
Figure 2.8: (a) A three-level system with a doubly excited state. (b) A pulse sequence for a double-quantum spectrum. (c) The two corresponding double-sided Feynman diagrams. (d) The double-quantum spectrum for this system.

pulse must also be an excitation from the left. Thus, after the first pulse, the system is in a coherent superposition between the ground and the first excited state, and after the second pulse, the system is in a coherent superposition between the ground and the doubly excited state. Moving on, the third pulse is conjugated, so it can either be an excitation from the right or a de-excitation to the left. Both of these can yield valid Feynman diagrams, and will result in a single-quantum coherence. As before, the last interaction arrow corresponds to emission which can be measured using heterodyne detection.

The location of the peak in the double-quantum spectrum again can be found using the coherences in the Feynman diagram. The emission frequency ω_t is once again determined by the state during the t time delay. The double-quantum frequency is predictably determined by the state during the T time delay, which will have evolution frequency $\omega_{20} \approx 2\omega_{10}$. Unlike

23

for the rephasing spectrum, this frequency is positive, so the vertical axis is also positive. In the spectrum shown in Figure 2.8 (d), the plotted diagonal is $\omega_T = 2\omega_t$.

It is worth emphasizing the importance of the doubly excited state to a double-quantum spectrum. We saw that for the double-quantum pathway, valid Feynman diagrams require a double-quantum coherence after the second pulse. Thus a double-quantum signal will only exist if a doubly excited state exists.

While double-quantum spectra can be used to probe a single system with a doubly excited state, it is more commonly used to measure interactions between multiple systems. Consider two two-level systems, which can combine to form a single diamond-shaped four-level system, as is shown in Figure 2.9. The differences between the ground and singly excited states in the four-level system are the same as for the individual two-level systems. However, the difference between the ground and doubly excited states is not simply the sum of the energy differences for the two two-level systems, instead it is reduced by a term Δ due to the interaction between the systems.

Recall our two Feynman diagrams from Figure 2.8 (c). Recall also that the leading sign of Equation 2.27 is due only to the side of the interaction, notated by $\zeta_{n,d}$. For the first Feynman diagram, all interactions act on the left side, and for the second diagram, all but one of the interactions act on the left side. Thus, the signal due to these two diagrams have opposite signs. If the energy difference between the ground and first excited state and the energy difference between the first and doubly excited states are equal, or if $\omega_{10} = \omega_{21}$, then
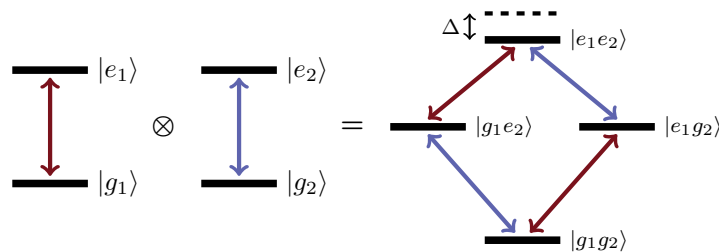
Figure 2.9: A depiction of two two-level systems combining to form a single four-level system. Due to interactions, the energy of the doubly excited state $|e_1 e_2\rangle$ is reduced by Δ.

the signals from the two Feynman diagrams will cancel, and no signal will be measured. This means that an interaction term such as Δ is required to observe a double-quantum signal [42]. Double-quantum spectra, therefore, provide a background-free measurement of interacting systems, and seeing a double-quantum signal generally implies the existence of interactions.

Lastly, we will note that higher order n-quantum spectra can be obtained by allowing pulses B and C^* to interact with the system multiple times, allowing us to probe a coherence between a ground and nth excited state. This will be expanded upon in Chapter 6.3.1.

2.3 Experimental Realization

The experiment I primarily worked on for this thesis is a collinear MDCS experiment. It is capable of heterodyne, photoluminescence, and photocurrent detection schemes [49], although I primarily worked with photoluminescence detection. A schematic of the experiment is shown in Figure 2.10. A pulsed titanium-sapphire (Ti:sapph) laser is fed through nested Mach-Zehnder interferometer to create the four optical pulses needed for an MDCS experiment. These pulses are each tagged using an acousto-optic modulator (AOM), before being recombined to a single collinear beam, which is then sent to the sample. Regardless of detection scheme, the final signal is measured using a photodetector and a lock-in amplifier. In the following sections we will explore some of the specifics of the experimental setup in more detail.

2.3.1 Collinear Multidimensional Coherent Spectroscopy

As expressed in Section 2.1, in a MDCS experiment it is very important to isolate the desired third-order signal. Originally, this was done with k-vector selection. In this method the three pulses A, B, and C strike the sample from different directions and the signal is emitted in a fourth direction [12]. For instance, for a rephasing spectrum the signal is emitted in the
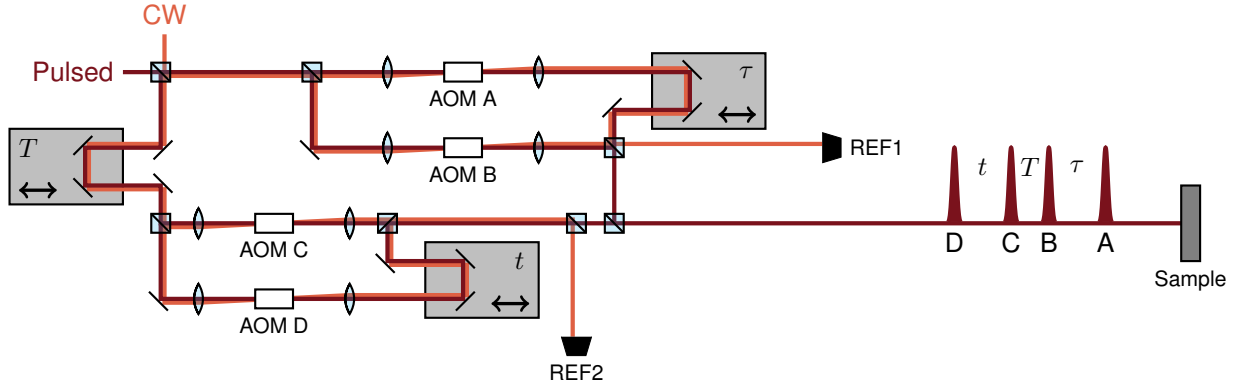
Figure 2.10: A schematic of a collinear MDCS experiment.

$-\mathbf{k}_A + \mathbf{k}_B + \mathbf{k}_C$ direction. However, the complex geometry this requires can be tricky to align and uses a large spot size on the sample, making any sort of imaging impractical. Active phase stabilization is also required, which can be finicky to implement. Furthermore, photoluminescence detection is not possible with this experimental configuration, since the photoluminescence will not be emitted in any particular direction, so the desired signal pathway cannot be isolated.

Instead, our experiment uses a collinear design, which was first demonstrated in Reference [65]. Since the incident beams are collinear, we can no longer isolate the desired third-order signal spatially. Rather, AOMs are used to tag each beam with a different frequency, as shown in Figure 2.10. The first order diffraction from each AOM will be modulated at the driving frequency of the AOM, which has the effect of shifting the laser frequency by this driving frequency. Since each pulse is shifted by a different amount, the phases of the four beams will shift with respect to each other. The phase shift between two beams will cycle at a rate of the difference between their respective driving frequencies. This results in modulations of the different third-order signals, each determined similarly to the k-vector selection directions [49].

To enable more specificity, let the AOM frequencies for the four beams be ω_A, ω_B, ω_C, and ω_D. The rephasing signal will be modulated at frequency $-\omega_A + \omega_B + \omega_C - \omega_D$ and the double-quantum signal will be modulated at frequency $\omega_A + \omega_B - \omega_C - \omega_D$ [61].

26

Our desired measurement is phase dependent, and is therefore sensitive to extremely slight changes in distance between the different interferometer arms. To control for this, we use passive phase stabilization in the form of a continuous wave (CW) reference laser. A CW Helium-Neon laser co-propagates with the pulsed laser through the interferometer. We send the combined AB and CD CW beams onto separate detectors, labeled REF1 and REF2 in Figure 2.10, which are used to obtain the reference for the detection frequency.

In practice, for a rephasing spectrum, we modulate the AOMs in the range of $80\,\mathrm{MHz}$, and set the difference frequencies $\omega_B - \omega_A$ and $\omega_D - \omega_C$, as well as the signal frequency $-\omega_A + \omega_B + \omega_C - \omega_D$, to values between 50 and $150\,\mathrm{kHz}$ so that these frequencies can be detected in the corresponding reference and signal detectors. The outputs of the reference detectors are fed into a field programmable gate array (FPGA), which digitally computes the sum and difference of the frequencies. The difference frequency is required for rephasing spectra, and is sent to the lock-in amplifier to isolate the signal.

Double-quantum spectra can also be taken with our setup, but a few things must be changed first. First, we set the difference frequencies $\omega_C - \omega_A$ and $\omega_B - \omega_D$ and the signal frequency $\omega_A + \omega_B - \omega_C - \omega_D$ similarly to the corresponding frequencies in the rephasing spectrum. This means to retrieve these frequencies from the reference laser, we must send all four CW beams onto a single detector. Then the FPGA applies filters to the detector output to isolate the two difference frequencies, before computing their difference to obtain the final reference frequency.

2.3.2 Detection Schemes

Now that we have determined the frequency reference, we need to find the signal itself. A collinear geometry enables multiple detection schemes, and we will focus on heterodyne and photoluminescence detection, whose implementations are described in Reference [62].

In heterodyne detection, only the first three pulses are sent to the sample, as shown in Figure 2.11 (a). They impinge normally to the sample, and the third-order coherent
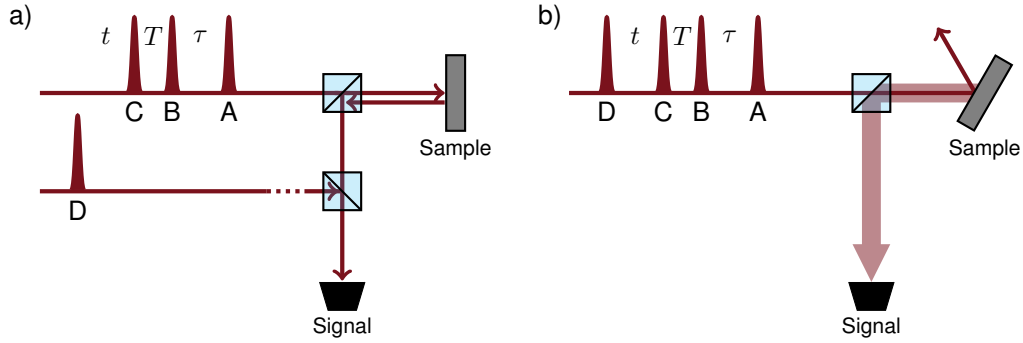
Figure 2.11: Schematics of (a) heterodyne detection and (b) photoluminescence detection.

four-wave-mixing signal propagates backward the beam path, where it is picked off by a beamsplitter. Another beamsplitter combines it with the fourth pulse to allow them to interfere, and both are sent onto a detector. The detector output is fed into a lock-in amplifier. Alternatively, some implementations of heterodyne detected MDCS find it more convenient to send all four pulses to the sample. In this case, it is assumed that the fourth pulse does not interfere with the sample. This form is easier to implement and align, and makes more complex imaging feasible [52].

In photoluminescence detection, all four pulses are sent to the sample and interfere with the sample, as shown in Figure 2.11 (b), making photoluminescence detection a fourth-order signal. Instead of measuring the four-wave-mixing signal directly, the nonlinear effects result in a modulation of the incoherent photoluminescence, which is collected. In order to isolate the photoluminescence, it is important to remove as much of the laser scatter as possible. One way we do this is by mounting the sample at a 30° angle, so that the laser is primarily reflected away from the beam path. Since the photoluminescence is generally not emitted in a single specific direction, it will still be collected. Additionally, we cross-polarize the detection, meaning we send a linear polarization of light to the sample, and use a polarizer to filter most of the reflected laser and collect only the perpendicular polarization. An anti-reflective coating can also help reduce reflections from the sample surface.

Photocurrent detection is very similar to photoluminescence detection, in that all four

pulses are sent to the sample. However, instead of measuring emitted light on a detector, a photocurrent signal is measured directly using electrical contacts on the sample. While the experiment I worked on for this thesis is capable of photocurrent detection, I did not use this functionality.

2.3.3   Other Experimental Details

Regardless of detection method, MDCS requires resonant excitation of the system being measured. Thus, the types of systems available for study are limited by the type of laser being used. Our laser is a tunable, $700 - 950 \, \text{nm}$, pulsed Ti:sapph with a $76 \, \text{MHz}$ repetition rate and $7 - 10 \, \text{nm}$ bandwidth. This makes it ideal for studying narrow resonance structures, such as that of the SiV center, since more of the laser spectrum is able to access the system. The narrow bandwidth also reduces the need for dispersion compensation. However, broader resonances structures, for instance those of transition-metal dichalcogenide (TMDC)s, cannot be effectively probed, since the laser is unable to interact with all resonances of a system at once.

To ensure that we are observing a third-order signal, we measure the magnitude of the signal as a function of laser power. Recall that heterodyne detection should be of third order and photoluminescence detection should be of fourth order. Since the intensity of the incident laser should follow $I \propto |E|^2$, for signal strength S, we ensure the laser power is within the range such that $S \propto I^{3/2}$ for heterodyne detection and $S \propto I^2$ for photoluminescence detection.

The systems being studied typically have narrower spectral peaks at low temperatures. Thus, to observe the system in more detail, it is advantageous to chill the sample. To this end, we use a closed-loop cryostat capable of keeping the sample at around $11 \, \text{K}$.

One advantage of a collinear design is the ability to achieve small spot sizes and use imaging. We send our recombined beams through a 20X/0.40 N.A. objective, giving a spot size of $1 - 4 \, \mu\text{m}$, depending on the diameter of the incident laser beam. Our objective also

has a long working distance of 19 mm, which allows us to focus on any part of the sample, even when it is mounted at an angle in the cryostat.

For simple imaging, the objective is mounted on a three-axis translation stage. A series of mirrors are mounted to the stages to keep the laser centered on the objective for all stage positions. Spectra can be taken at different points along the sample, down to a resolution of 1 µm.

CHAPTER 3

Silicon-Vacancy Center Background

It is well known that diamond is a special material, and it has been prized since antiquity for its beauty and strength. However, in recent years, there has been much scientific interest in diamond color centers, such as the NV and SiV color centers. These impurities can be found in naturally occurring diamond, and their presence can give these diamonds color.

There are many known impurities in diamond which can appear in absorption or photo-luminescence spectra [73]. Finding the physical defects responsible for the various spectral signatures was a challenge for researchers, however. The NV center was identified as a nitrogen-based defect in the 1970s by comparing the absorption and luminescence spectra from irradiated and annealed diamond with nitrogen impurities [13]. The physical structure for the SiV center was determined in the 1990s using silicon doped diamond [11] and ab initio calculations [25].

Since then, these defects have attracted attention due to their potential uses in quantum information and quantum sensing. For instance, these defects have shown promise as a single photon source [34] and as a quantum memory [23, 63], and they have been integrated into photonic circuits [20, 68]. Additionally, the NV center has demonstrated utility as a strain gauge in a diamond anvil cell [31] and has been used extensively to measure the magnetic fields of microscopic structures [64, 37].While much of this work has focused on the NV center, the SiV center has some key advantages over the NV center, its large zero-phonon line (ZPL) and inversion symmetry in particular, which has lead to an increased interest in

it over the past decade.

In this chapter, we will give an overview of the SiV center. In Section 3.1 we will discuss the physical crystal structure of diamond and the SiV center. Following that, Section 3.2 will have a brief discussion of of the electronic structure of the ZPL of the SiV center. Section 3.3 will give more specific background regarding how the SiV center responds to strain, including a general discussion of strain and a discussion of some previous results by Meesala, et al. [45]. Finally, Section 3.4 will briefly discuss a project I worked on using double-quantum MDCS to detect interactions between nearby SiV centers.

3.1 Physical Structure and Orientation

3.1.1 Diamond Crystal Structure

Diamond consists of a lattice of covalently bonded carbon atoms. More specifically, these carbon atoms are arranged in face-centered cubic lattice structure of side length 3.57 Å with a two-atom basis: atoms at $[000]$ and $[\frac{1}{4}\frac{1}{4}\frac{1}{4}]$ [3, pg. 76]. A view of the unit cell is shown in Figure 3.1 (a).

It is common to use Miller indices to describe directions and surfaces within the crystal, as described in Reference [3, pgs. 91-93]. They can be used to specify planes (with parentheses) or directions (with square brackets) using the basis vectors of the unit cell. If the basis vectors for the direct lattice are $\mathbf{a}_1$, $\mathbf{a}_2$, and $\mathbf{a}_3$, (which, for a cubic lattice, point along the edges of a unit cell), then directions defined with Miller indices $[hkl]$ will always be parallel to the vector $h\mathbf{a}_1 + k\mathbf{a}_2 + l\mathbf{a}_3$. Miller indices of lattice planes are defined using the reciprocal lattice, with basis vectors $\mathbf{b}_1$, $\mathbf{b}_2$, and $\mathbf{b}_3$, so the lattice plane (hkl) is defined to be normal to the reciprocal lattice vector $h\mathbf{b}_1 + k\mathbf{b}_2 + l\mathbf{b}_3$. For a cubic lattice, the reciprocal lattice vectors and direct lattice vectors are parallel to each other, so the plane defined by (hkl) will be normal to the direction $[hkl]$. It is also standard to represent negative numbers using bars, for example $\bar{k}$ instead of $-k$. Some common examples for the cubic lattice are shown in
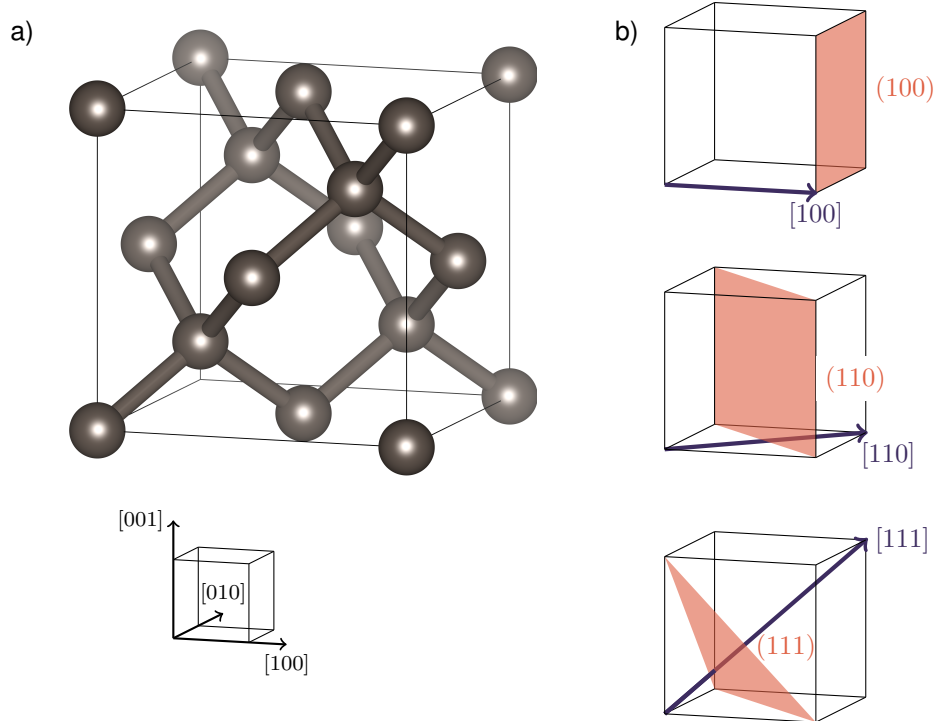
Figure 3.1: (a) The unit cell of the diamond lattice, with the axis labels shown for the crystal basis [46]. (b) Some commonly used Miller indices for the cubic lattice. Example directions are shown in purple, and planes are shown in orange.

Figure 3.1 (b).

Miller indices are used to describe the cut of a diamond surface, or the plane on which it is grown. The surfaces (100), (110), and (111) are all common growing surfaces. As will be discussed in Section 4.1.2, our sample is (110)-oriented. A top-down view of (110)-oriented diamond is shown in Figure 3.2.

The diamond lattice has four different orientations of carbon-carbon bonds, which can be expressed using Miller indices as $[111]$, $[1\bar{1}\bar{1}]$, $[\bar{1}1\bar{1}]$, and $[\bar{1}\bar{1}1]$. Due to the symmetry of the diamond lattice, this can also be represented more succinctly as $\langle 111 \rangle$, where the angle brackets indicate all equivalent lattice directions. Looking at these different directions in the (110)-oriented diamond, we see that the carbon-carbon bonds can be sorted into two groups: in-plane and out-of-plane orientations, as depicted in Figure 3.2. The in-plane orientations have the carbon-carbon bonds in the plane of the sample surface. The-out-of-
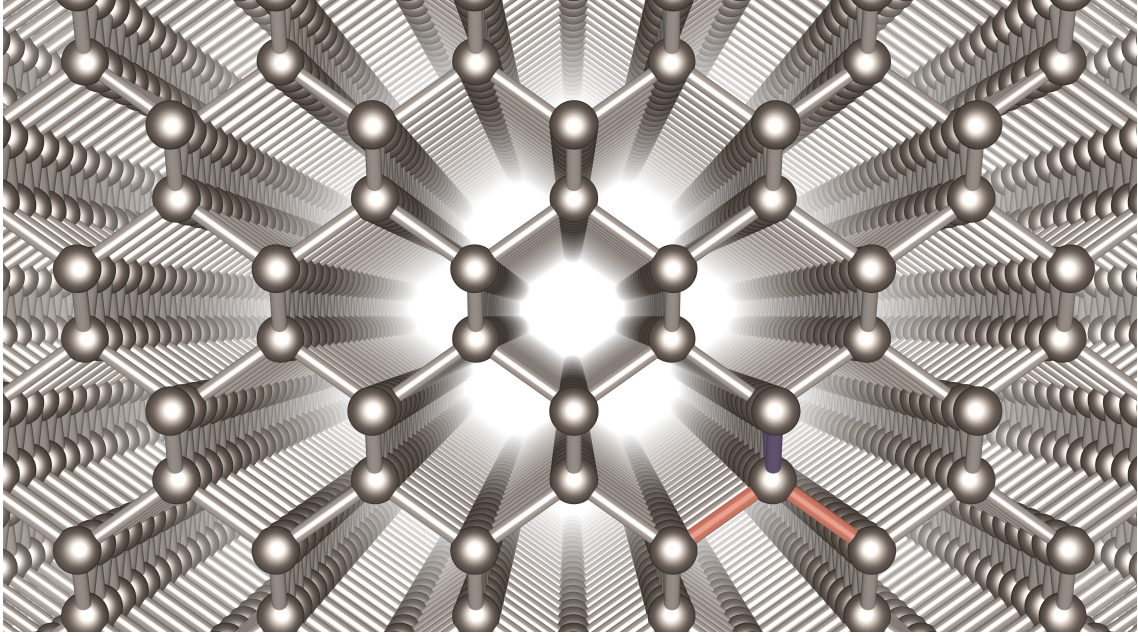
Figure 3.2: A top down view of (110)-oriented diamond. The four orientations of carbon-carbon bonds can be grouped into in-plane (orange) and out-of-plane (purple) directions.

plane orientations are at an angle of 54.7° from the sample surface.

3.1.2   Silicon-Vacancy Structure

The SiV center is one of many color centers in diamond, which are point defects in the diamond lattice. Point defects are so called because they occur around a single point in a crystal [3, pg. 616]. The SiV center is formed by replacing two adjacent carbon atoms from the diamond, and replacing them by a single silicon atom, as shown in Figure 3.3 (a). Since there is one fewer atom than before, we often say that the second lattice site is empty, or vacant, hence the name "silicon-vacancy" center.

The SiV center is often compared to the NV center, which is shown in Figure 3.3 (b), and has been the focus of much scientific research [18]. Both have similar construction, but for the NV center the two carbon atoms have been replaced by a single nitrogen atom. Unlike the nitrogen in the NV center, the silicon in the SiV center is located directly between two lattice sites in the crystal, as can be seen in Figure 3.3 [25]. This means that, unlike the NV
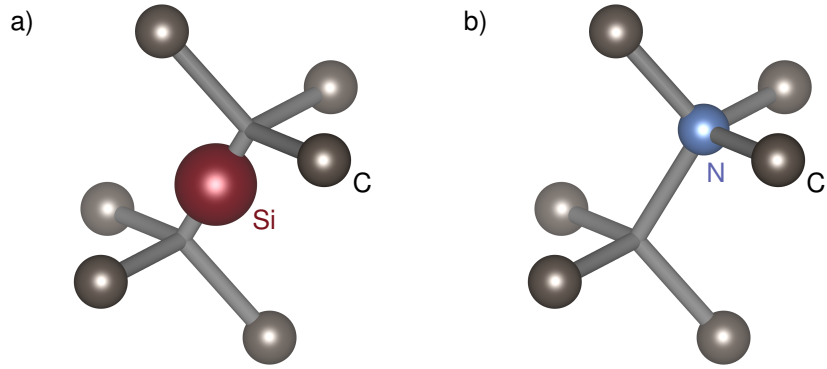
Figure 3.3: Diagrams of the (a) SiV and (b) NV center [46].

center, the SiV center is inversion symmetric, which makes it less susceptible to the Stark effect and other irregularities within the diamond.

Since the SiV center occurs between between two adjacent lattice sites, it is restricted to several possible orientations within the crystal. We will define the SiV axis as the axis which passes through the two vacant lattice sites in a given SiV center, and this axis is shown in Figure 3.4 (a). Using this definition, the SiV axis can only occur along the four possible directions of carbon-carbon bonds in the crystal. Thus, our discussion of carbon-carbon bond orientations in Section 3.1.1 also translates to SiV center orientations. In particular, for a (110)-oriented diamond, the SiV centers can be grouped into in-plane and out-of-plane centers. This will be further expanded upon in Section 4.2.1.
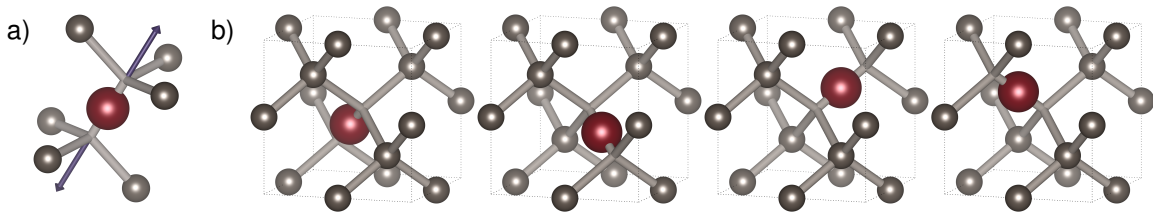
Figure 3.4: (a) A diagram of the SiV center with the SiV axis shown in purple. (b) The four possible orientations of a SiV center [46].

3.1.3 Bases

In this work, we will find it useful to define two different bases. The first of these is defined for the diamond crystal. Since our sample is (110) oriented, we will choose the y-axis to be normal to the sample surface, or in the [110] direction. We will fix the z-axis to the [001] direction, which puts the x-axis in the [1$\bar{1}$0] direction. These three axes are pictured in Figure 3.5 (a).

The second basis will be defined relative to a given SiV center. We will let the z'-axis be along the SiV axis shown in Figure 3.4 (a), which is also along the $\langle 111 \rangle$ direction. We will define the x'-axis and y'-axis as pictured in Figure 3.5 (b), or along the $\langle 1\bar{2}1 \rangle$ and $\langle 10\bar{1} \rangle$ directions, respectively. Because there the four orientations of SiV center, there are four different SiV bases.

It will be useful to be able to convert between these different bases. First we will define

$$\phi = 1/2 \arccos{(-1/3)} \approx 54.7°, \tag{3.1}$$

where 2ϕ is also the angle between adjacent bonds in the diamond lattice [3, pg. 82]. Let $R_\sigma(\theta)$ be the matrix representing a counterclockwise rotation of θ about the σ axis. We can
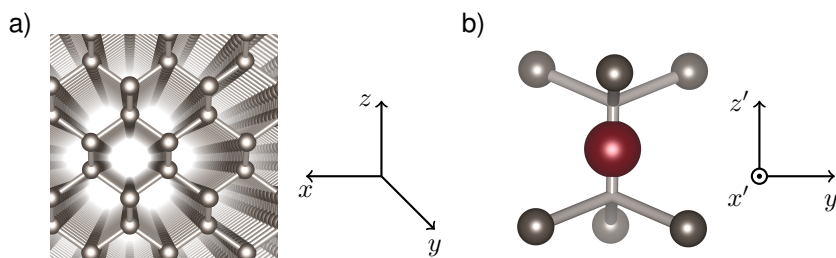
Figure 3.5: (a) The crystal basis for (110)-oriented diamond. (b) The SiV basis for a specific SiV center.

rotate a vector **r** from the crystal basis to each of the SiV bases using

$$\mathbf{r}' = R_y\left(\phi\right)\mathbf{r},$$

$$\mathbf{r}' = R_y\left(-\phi\right)R_z\left(\pi\right)\mathbf{r},$$

$$\mathbf{r}' = R_y\left(\phi\right)R_z\left(-\frac{\pi}{2}\right)\mathbf{r}, \qquad (3.2)$$

$$\mathbf{r}' = R_y\left(-\phi\right)R_z\left(\frac{\pi}{2}\right)\mathbf{r}.$$

To reverse these transformations, we can apply the transpose of the rotation matrices (corresponding to a clockwise rotation) in the opposite order.

3.1.4 Growing Diamond Samples

While diamond can form naturally and be mined, for scientific applications it is often desirable to grow the diamond under controlled conditions. This is commonly done with high-pressure high-temperature (HPHT) or chemical vapor deposition (CVD) growth processes [19]. There are several ways to introduce color centers into the diamond lattice. They can occur in natural diamond that is formed in the presence of a particular impurity. For lab-grown diamonds, defects can be added either during the growth process or afterward, through ion implantation .

For CVD grown diamond, an impurity can simply be added to the vapor, and atoms from this impurity will be incorporated into the lattice as the diamond grows [50]. This means there is no control over the position of individual defects, and they are randomly distributed across a given plane in the diamond. This method can also prefer a particular orientation (or several orientations) of defect centers, depending on the growth plane of the diamond [27].

Impurities can also be added to existing diamond through ion implantation [69]. In this case an accelerator is used to fire ions into diamond. This embeds the ions into the crystal, but they cause damage to the crystal along the path over which they travel [32], and are

likely not initially positioned as the desired defect center (e.g. an interstitial defect instead of a NV or a SiV center) [35]. At this point, the diamond is typically annealed, or heated at high temperatures, to allow the atoms to settle into a more regular and more favorable state. This method does give some control over the position of the implanted ions, and the depth of the ion can be controlled by varying the implantation energy. The density of implanted ions can also be controlled, but the orientation of the resultant color centers is random.

3.2   Electronic Structure

While the understanding the physical structure of these centers is important when interpreting results, the reason we want to study the SiV center is due to its electronic structure. We will also restrict our discussion to the negatively charged SiV^- center [24]. Other charge states do exist, most notably the neutral SiV^0 center [26, 17]. We will also continue to compare the SiV center with the NV center.

One advantage of diamond as a host material is its wide band gap of $5.5\,\text{eV}$ [15]. This means that electronic excitations can fit easily within the band gap and remain and isolated from the conduction band.

We care primarily about the ZPL of the SiV center. The ZPL corresponds to the electronic
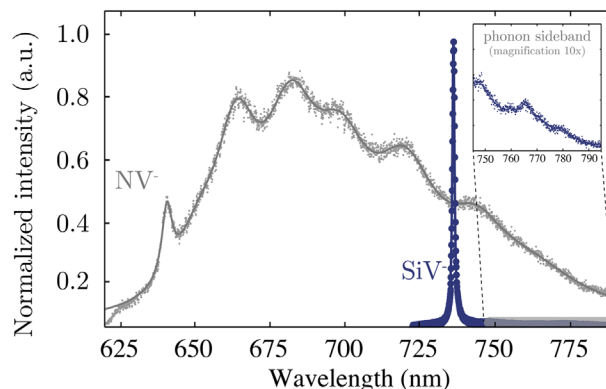
Figure 3.6: A plot comparing the the ZPLs and phonon sidebands of the NV and SiV centers, figure reproduced from Reference [6].

transition without contributions from phonons, or vibration modes within the crystal. It is often accompanied by a phonon sideband, for which phonons do contribute. The phonon sideband is typically much broader than the ZPL [11]. Many color center applications require the simpler physics of the ZPL, so it is desirable to have most photons absorbed by or emitted from the ZPL. Thus, the relatively weak phonon sideband and strong ZPL of the SiV center gives it an advantage over the NV center, which has a comparatively weaker ZPL as shown in Figure 3.6 [6, 55].

The ZPL of the SiV center is centered around $407\,\mathrm{THz}$ or $1.68\,\mathrm{eV}$ [11]. This makes it optically accessible with $737\,\mathrm{nm}$ light. The energy level diagram of the SiV center has split ground and excited states resulting in a four-level system as pictured in Figure 3.7 (a) [11, 30, 55]. These can also be split further with the application of a magnetic field due to the Zeeman effect [30], which is not pictured.

As shown in Figure 3.7, each transition between a given ground and excited state pair is allowed. This means there are four possible transitions in this level diagram, and a typical SiV spectrum will have four peaks as shown in Figure 3.7 (b). However, it has also been
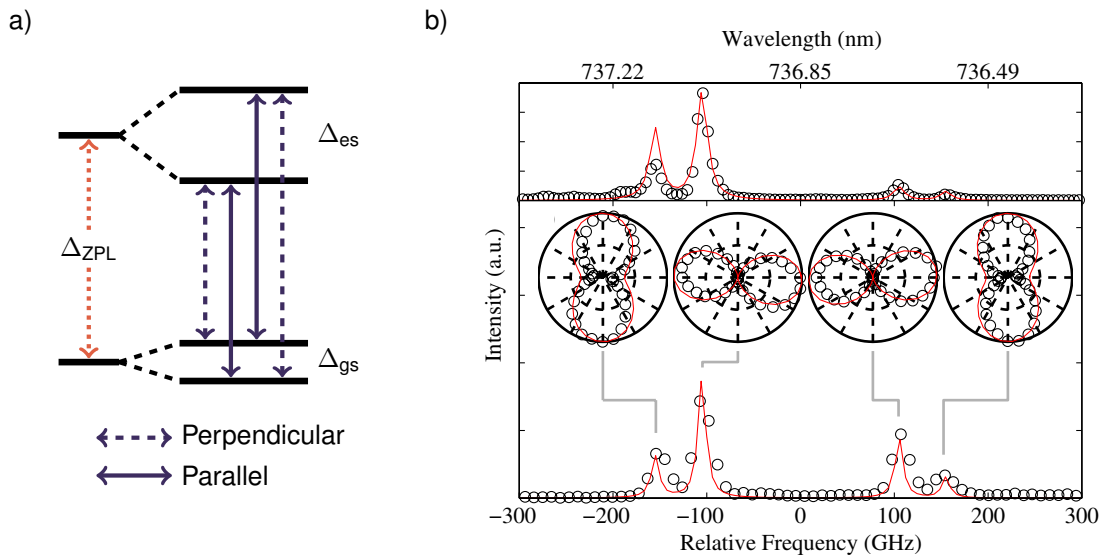
Figure 3.7: (a) The energy level diagram for the SiV center. (b) SiV spectra and polarization measurements, figure reproduced from Reference [30].

found that there is a polarization dependence for these peaks [30, 55], which is also shown in Figure 3.7 (b). These polarization selection rules are depicted in Figure 3.7 (a) using dashed and solid lines.

3.3   Strain

3.3.1   Strain Tensor

The strain tensor is a measure of how much a material is deformed. We begin by defining a function $\mathbf{u}(\mathbf{R})$, which measures how much the point $\mathbf{R}$ is displaced from equilibrium. For example, if we consider $\mathbf{R}$ to be the equilibrium position, and $\mathbf{R}'$ to be the position after a deformation, then

$$\mathbf{u}(\mathbf{R}) = \mathbf{R}' - \mathbf{R}. \tag{3.3}$$

Note that $\mathbf{u}$ is a vector an can be broken into components as $\mathbf{u} = u_x\hat{\mathbf{x}} + u_y\hat{\mathbf{y}} + u_z\hat{\mathbf{z}}$. Each strain tensor index can be written as [3, eq. 22.77]

$$\varepsilon_{\sigma\mu} = \frac{1}{2}\left(\frac{\partial}{\partial x_\sigma}u_\mu + \frac{\partial}{\partial x_\mu}u_\sigma\right). \tag{3.4}$$

Thus, the full strain tensor is

$$\boldsymbol{\varepsilon} = \begin{pmatrix} \varepsilon_{xx} & \varepsilon_{xy} & \varepsilon_{xz} \\ \varepsilon_{yx} & \varepsilon_{yy} & \varepsilon_{yz} \\ \varepsilon_{zx} & \varepsilon_{zy} & \varepsilon_{zz} \end{pmatrix} = \begin{pmatrix} \frac{\partial u_x}{\partial x} & \frac{1}{2}\left(\frac{\partial u_y}{\partial x} + \frac{\partial u_x}{\partial y}\right) & \frac{1}{2}\left(\frac{\partial u_x}{\partial z} + \frac{\partial u_z}{\partial x}\right) \\ \frac{1}{2}\left(\frac{\partial u_y}{\partial x} + \frac{\partial u_x}{\partial y}\right) & \frac{\partial u_y}{\partial y} & \frac{1}{2}\left(\frac{\partial u_z}{\partial y} + \frac{\partial u_y}{\partial z}\right) \\ \frac{1}{2}\left(\frac{\partial u_x}{\partial z} + \frac{\partial u_z}{\partial x}\right) & \frac{1}{2}\left(\frac{\partial u_z}{\partial y} + \frac{\partial u_y}{\partial z}\right) & \frac{\partial u_z}{\partial z}. \end{pmatrix} \tag{3.5}$$

Note that the strain tensor is symmetric, so there are only six different strain tensor indices, which we will divide into the normal strain tensor indices $(\varepsilon_{xx}, \varepsilon_{yy}, \varepsilon_{zz})$, and the shear strain tensor indices $(\varepsilon_{xy}, \varepsilon_{yz}, \varepsilon_{zx})$. Also note that the strain tensor indices are unitless.

Normal strain in the x, y, or z directions can be thought of simply as stretching or
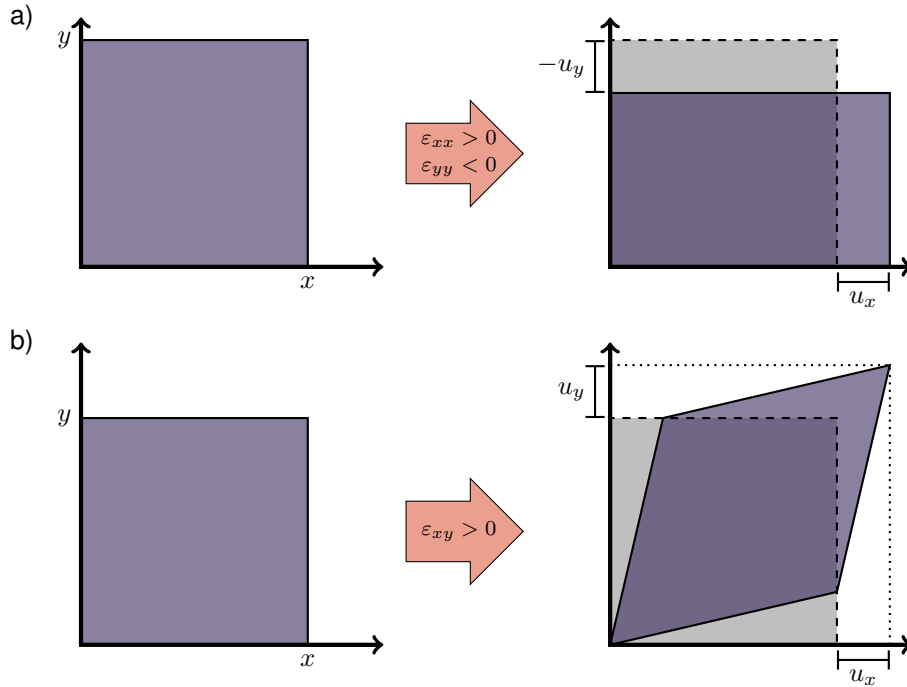
Figure 3.8: The effects of (a) normal strain and (b) shear strain on a square.

squeezing the material along that axis. Figure 3.8 (a) shows an example of an object under normal strain. In this example, $\varepsilon_{xx} > 0$, so as we move in the x direction, the displacement in that direction, u_x, increases. Similarly, $\varepsilon_{yy} < 0$, so as we move in the y direction, the displacement in that direction, u_y, decreases

Shear strain is not restricted to the x, y, or z directions. Figure 3.8 (b) shows an example of an object under shear strain, so $\varepsilon_{xy} > 0$. As we move in the x direction, the displacement in the y direction u_y increases. Similarly, as we move in the y direction, the displacement in the x direction u_x increases.

One last useful feature of the strain tensor is that we can change its reference frame using rotation matrices using

$$R_\sigma(\theta) \cdot \boldsymbol{\varepsilon} \cdot R_\sigma^T(\theta). \tag{3.6}$$

This often will turn normal strain into shear strain or vice versa, as normal strain in one reference frame can become shear strain in another.

3.3.2 The Effects of Strain on Silicon-Vacancy Centers

Previous experimental work has been done to characterize how the SiV center responds to strain. Meesala, et al. [45] fabricated a diamond cantilever including two electrodes on and below the cantilever. By applying a voltage to the electrodes, they could warp the diamond in a predictable way and observe the resulting shifts in the spectral peaks.

In order to interpret these results, they also derived peak locations in terms of the strain tensor indices and various constants. In the SiV reference frame described in Section 3.1.3, these equations can be written as [45]

$$
\begin{aligned}
\Delta_{\mathrm{ZPL}} &= \Delta_{\mathrm{ZPL},0} + \left(t_{\parallel,\mathrm{es}} - t_{\parallel,\mathrm{gs}}\right)\varepsilon'_{zz} + \left(t_{\perp,\mathrm{es}} - t_{\perp,\mathrm{gs}}\right)\left(\varepsilon'_{xx} + \varepsilon'_{yy}\right), \\
\Delta_{\mathrm{gs}} &= \sqrt{\lambda^2_{\mathrm{SO,gs}} + 4\left(d_{\mathrm{gs}}\left(\varepsilon'_{xx} - \varepsilon'_{yy}\right) + f_{\mathrm{gs}}\varepsilon'_{zx}\right)^2 + 4\left(-2d_{\mathrm{gs}}\varepsilon'_{xy} + f_{\mathrm{gs}}\varepsilon'_{yz}\right)^2}, \\
\Delta_{\mathrm{es}} &= \sqrt{\lambda^2_{\mathrm{SO,es}} + 4\left(d_{\mathrm{es}}\left(\varepsilon'_{xx} - \varepsilon'_{yy}\right) + f_{\mathrm{es}}\varepsilon'_{zx}\right)^2 + 4\left(-2d_{\mathrm{es}}\varepsilon'_{xy} + f_{\mathrm{es}}\varepsilon'_{yz}\right)^2}.
\end{aligned}
\tag{3.7}
$$

In these equations, Δ_{ZPL}, Δ_{gs}, and Δ_{es} represent the corresponding labeled quantities in the energy level diagram in Figure 3.7. These can be used to uniquely determine the frequencies of the four SiV peaks. The corresponding quantities at zero strain are represented by $\Delta_{\mathrm{ZPL},0}$, $\lambda_{\mathrm{SO,gs}}$, and $\lambda_{\mathrm{SO,es}}$. The strain tensor indices in the SiV basis are given by $\varepsilon_{i,j}$. The remaining quantities, $t_{\parallel}$, $t_{\perp}$, d, and f, are called the strain-susceptibility parameters, which they determine from the experimental results.

Some of the experimental data from Reference [45] is shown in Figure 3.9. Due to the crystal orientation relative to the cantilever, half of the SiV centers primarily saw changes in Δ_{gs} and Δ_{es}, while the other half primarily saw changes in Δ_{ZPL}.

By fitting this experimental data to the derived equations, they were able determine the
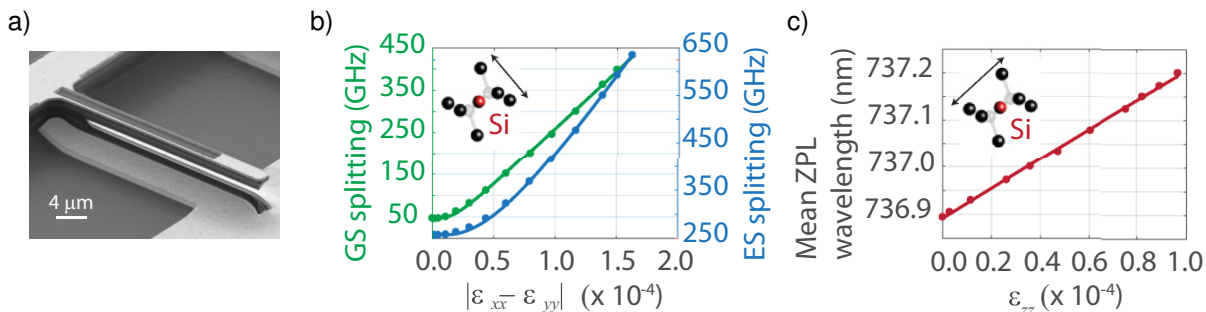
Figure 3.9: The effects of (a) transverse strain on the ground and excited state splitting of the SiV center, and (b) longitudinal strain on the mean ZPL wavelength. All three figures reproduced from Reference [45]

necessary strain susceptibility parameters. They found that [45]

$$
\begin{aligned}
\left(t_{\parallel,\text{es}} - t_{\parallel,\text{gs}}\right) &= -1.7 \pm 0.1 \,\text{PHz/strain}, \\
\left(t_{\perp,\text{es}} - t_{\perp,\text{gs}}\right) &= 0.078 \pm 0.009 \,\text{PHz/strain}, \\
d_{\text{gs}} &= 1.3 \pm 0.1 \,\text{PHz/strain}, \\
d_{\text{es}} &= 1.8 \pm 0.2 \,\text{PHz/strain}, \\
f_{\text{gs}} &= -1.7 \pm 0.1 \,\text{PHz/strain}, \\
f_{\text{es}} &= -3.4 \pm 0.3 \,\text{PHz/strain}.
\end{aligned}
\tag{3.8}
$$

These results, in particular Equation 3.7, will be especially important in Chapter 4.

3.4 Coherent Interactions between Silicon-Vacancy Centers in Diamond

While the strain results to be discussed in Chapter 4 make up my main experimental work, there are several other SiV center projects to which I made lesser contributions. The first of these measures MDCS spectra using both heterodyne and photoluminescence detection, whose implementation is discussed in Section 2.3.2. The heterodyne detected measurements reveal a single, inhomogeneously broadened peak. This is attributed to a large number of

dark SiV centers, possibly in highly strained environments, which do not photoluminesce [62]. The second result measures a double-quantum MDCS signal from an ensemble of SiV centers [14], and will be discussed here in more detail.

Double-quantum MDCS is discussed in Section 2.2.4. In order to measure a double-quantum signal, rather than the rephasing signal used in Chapter 4, we changed the detection frequency from $-\omega_A + \omega_B + \omega_C - \omega_D$ to $\omega_A + \omega_B - \omega_C - \omega_D$. This meant we no longer used separate reference detectors, as depicted in Figure 2.10. Instead, we used a single detector, and relied on filters in the FPGA to isolate the reference signals from the AD and BC CW beams. We also used photoluminescence detection. There was additionally a fifth pump pulse of variable intensity, which reached the sample before the four MDCS pulses. Otherwise, the experimental details are similar to those described in Section 4.1.

One example spectrum is shown in Figure 3.10 (a). Recall from Section 2.2.4 that double-quantum MDCS requires a doubly excited state. For the SiV center, this doubly excited state must be due to interactions between SiV centers. Thus, observing any double-quantum signal
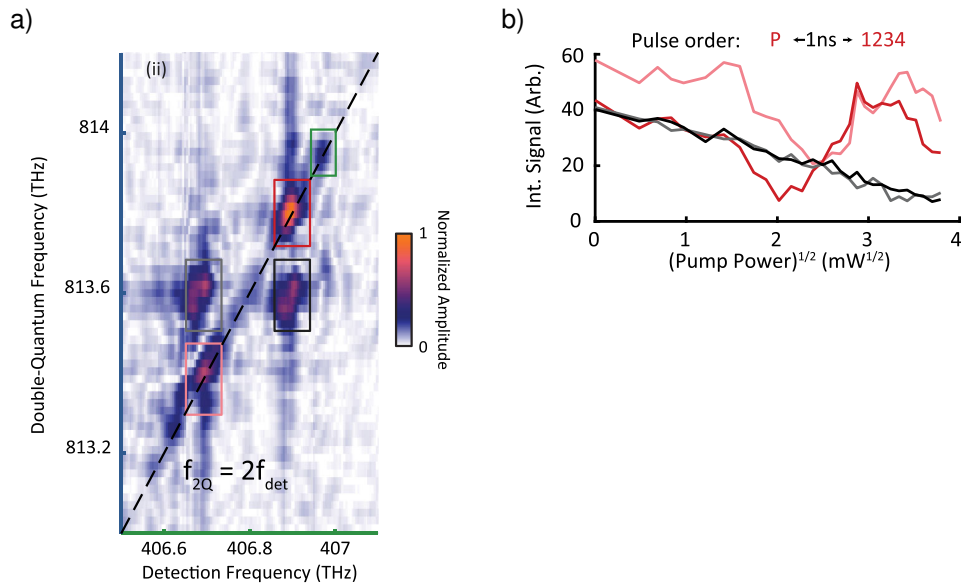
Figure 3.10: (a) A double-quantum MDCS spectrum of SiV centers. (b) Integrated peaks of the double quantum spectra, measured as a function of the power of the preceding pump pulse. Both figures reproduced from Reference [14].

at all requires the existence of such interactions. We attributed these interactions to dipole-dipole coupling between nearby SiV centers.

We also took spectra as a function of the power of the preceding pump pulse. For the off-diagonal peaks, we observe a decay in the peak strength as the pump power is increased. For the on-diagonal peaks, we observe oscillations in the peak strength as the pump power is increased. These trends are plotted in Figure 3.10 (b). Such oscillations are not present in similar rephasing spectra of the sample. We took data with several delay times between the pump pulse and MDCS pulses, with similar results. For each series of data, we also randomized the order in which the individual spectra were measured, to reduce the impact of slowly varying systematic error in the experiment.

The response to the pump pulse indicates that the interactions between nearby SiV centers is tunable. The interactions were also shown to last at least 1 ns, but we did not measure spectra with longer delay times between the pump and MDCS pulses.

CHAPTER 4

Using Silicon–Vacancy Centers in Diamond to Probe the Full Strain Tensor

NV centers have previously been used to sense strain in diamond [9, 66, 31]. The SiV center is similarly sensitive to strain, as was discussed in Section 3.3.2 using the results of Reference [45]. Here, we demonstrate the ability to use the SiV center to measure the full diamond strain tensor. Notably, our measurements are of an ensemble of SiV centers, due to the high implantation density of our sample. Since the strain in our sample has different effects on different SiV orientations, linear spectra can become quite crowded and difficult to read. Thus, we used the more powerful techniques of Chapter 2, in particular rephasing MDCS, to identify the peaks in our linear TPC spectra.

In this chapter, we will discuss our experimental results, including both TPC and MDCS spectra of the SiV center, and how we use them to find the strain present in our sample. While many of the experimental details are discussed in the preceding chapters, in Section 4.1 we will review some details regarding the specific spectroscopic techniques used here and the diamond sample used in these measurements. Section 4.2.3 will include the experimental results and their interpretation. It will also include the procedure used to calculate the strain

tensor using these results. The chapter will end with some concluding remarks in Section 4.3.

4.1 Experimental Methods

4.1.1 Spectroscopic Techniques

The experimental details are mostly discussed in Section 2.3. However, we will review and highlight a few relevant details.

We study an ensemble of SiV centers with two different coherent spectroscopy techniques. The first is a TPC measurement, as shown in Figure 4.1 (a), in which two optical pulses from a Ti:sapph laser are sent to a sample, much like the description in Section 2.2.1. We also use photoluminescence detection, as described in Section 2.3.2, in which we measure the modulated photoluminescence from the sample as a function of the temporal separation (t) between the pulses and isolate the signal using a lock-in amplifier. The photoluminescence intensity is Fourier transformed with respect to t, to yield a one-dimensional, coherently-detected absorption spectrum. The phase coherent spectra reject signal contributions from long-timescale effects, as the spectral response is recorded as a function of time delays between pulses which vary between 100 fs and 1 ns.

For this sample, the linear TPC spectra can be difficult to interpret on their own, as there
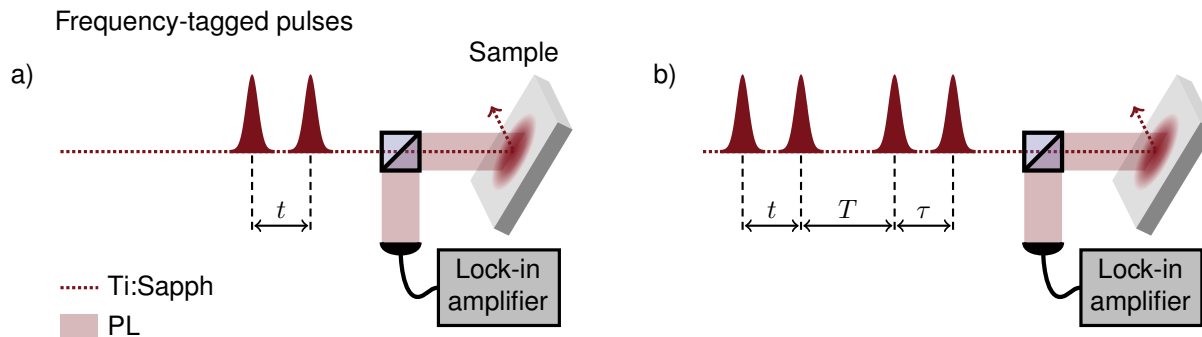
Figure 4.1: A depiction of the experimental setup, including both (a) TPC measurements and (b) MDCS measurements.

are many observed peaks to identify. Thus, we also employ rephasing MDCS, as discussed in Section 2.2.2 . Our collinear MDCS variant [65, 49, 62] is much like the TPC spectra discussed above, but with two additional optical pulses, as depicted in Figure 4.1 (b). For rephasing spectra, the first (τ) and third (t) time delays are varied, and these data are Fourier transformed with respect to these time delays to obtain a two dimensional map of the third-order signal as a function of excitation (ω_τ) and detection (ω_t) frequency axes [65, 49, 62].

Section 2.2.2 also mentioned two main advantages to using multidimensional rephasing spectra: the ability to easily distinguish between homogeneous and inhomogeneous broadening, and the ability to identify if two spectral peaks are coupled. The latter of these is more important to this work. If coupling exists between two transitions, a coupling crosspeak will occur where the excitation and detection frequencies correspond to those of the two coupled transitions. Since a single SiV center can emit at four different frequencies, a spectrum with multiple shifted families, or groups, of SiV centers can be difficult to interpret. In a rephasing MDCS spectrum, crosspeaks will be present for frequencies within a single family, but will not be present for pairs of frequencies from different families, so we can determine which spectral peaks correspond to a single family.

While the information contained in a TPC measurement is not as rich as that in a full MDCS spectrum, the main advantage is that the acquisition time for a TPC spectrum is much shorter. This enables us to take a large number of linear spectra to observe position dependent trends, while only taking a few select MDCS spectra when needed to assign the peaks.

As mentioned previously, both the TPC and MDCS spectra used here utilize collinear geometries, whose implementation is the focus of Section 2.3.3. This enables a smaller spot size than k-vector selection MDCS experiments [49], and allows us to compare spectra taken at nearby locations on the sample. Studies of color centers often take measurements of a single center, with no guarantees that the center is representative of neighboring centers. In

contrast, the high density of our sample and the ability of MDCS to untangle complicated spectra enable us to accurately measure the ensemble averaged optical response.

For both of these spectroscopic techniques, we linearly polarized the light incident on our sample. This was mainly so that the detected light could be cross-polarized to reduce laser scatter, which is important in photoluminescence detection. Additionally, since the four electronic transitions of the SiV center are polarization dependent [55], spectra taken at each polarization can be compared to understand the geometry of the sample.

4.1.2   Sample Information

Our sample is a CVD grown, (110)-oriented mono crystalline diamond. An ensemble of SiV centers was created by implanting silicon-29 ions with a focused ion beam, at a depth of $0.5-2.4\,\mu$m and number density $7.5 \times 10^{18}\,\mathrm{cm}^{-3}$. A plot detailing the expected implantation density as a function of depth is included in Figure 4.2 (a). The sample was then annealed at 1000–1050 °C and tri-acid cleaned. A picture of the sample is included in Figure 4.4. The sample has been cleaved, which explains its unusual shape, and an anti-reflective coating was applied. Additional information about the sample and its implantation can be seen in the Supplemental Material of Reference [62].

As discussed in Section 3.1, SiV centers can occur along four different orientations in diamond, corresponding to the four directions of carbon-carbon bonds in the diamond lattice. Figure 4.2 (b) shows the four orientations of SiV centers in our (110)-oriented sample, where the four vectors on the diamond correspond to the SiV axis shown in Fig. 3.4. Note that we can group these peaks into two orientation families. In-plane SiV centers (orange) lie parallel to the (110) surface plane, and out-of-plane SiV centers (purple) do not.

The sample was placed in a closed-loop cryostat at a temperature of 11 K. Data were taken using 76 MHz, 130 fs pulses from a Ti:sapph laser at a center wavelength of 736 nm. The output of each interferometer branch had power 1.25 mW, giving a total TPC power of 2.50 mW and a total MDCS power of 5.00 mW. This power was chosen to maximize
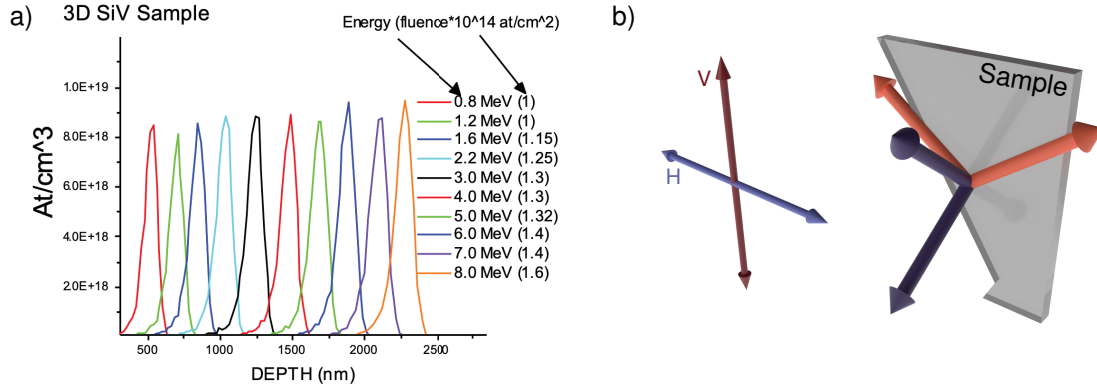
Figure 4.2: (a) A plot showing the density of implanted silicon versus depth in our sample. Reproduced from Reference [62] (b) The four orientations of SiV in our (110) oriented diamond sample. The orientations of the centers along the $\langle 111 \rangle$ axes of the lattice yield two in-plane (orange) and two out-of-plane (purple) orientations. The directions of vertical and horizontal polarizations relative to the sample are shown.

the signal while still ensuring the signal was of fourth-order. At these powers, we do not expect laser heating to impact our results since diamond is transparent at this wavelength. This is corroborated by the relatively sharp peak widths observed in our measured spectra. Pulses were focused onto the sample face using a home-built confocal microscope with a 20X/0.40 N.A. objective of focal length 10 mm. The Rayleigh range within the sample is long enough that these measurements address the entire column of implanted SiV centers. As shown in Figure 4.1, the sample was tilted by 30° from normal about the vertical axes in Figure 4.2 (b) and Figure 4.4 (a) to reject the reflected Ti:sapph beam and any coherent scatter that could corrupt the photoluminescence measurements. Due to the high index of refraction of diamond, this 30° tilt has a relatively small effect on the propagation direction of the laser within the sample. The two linear polarizations of light used here are depicted in Fig. 4.2 (b).

4.2 Results and Analysis

4.2.1 Peak Identification

As discussed in Section 3.2, previous experimental data taken of SiV centers [11, 55, 45, 62] show the four spectral peaks corresponding to the four optical transitions in Figure 3.7. Incoherent photoluminescence spectra taken from our sample have this structure as well [62]. However, the TPC photoluminescence spectrum in Figure 4.3 (a) shows many more peaks, indicating the presence of multiple groups of color centers.

These results, while initially suggestive, are greatly clarified by comparison to the results of full-fledged MDCS. Figure 4.3 (b) shows an example MDCS rephasing plot in which spectra taken with horizontally and vertically incident light have been summed together to better highlight all visible peaks. The insets (c-e) below this spectrum show more detail for some of the crosspeaks, both for the two polarized spectra and the combined spectrum. Note that in the combined spectrum, the seven visible crosspeaks can be grouped into two squares, which are highlighted in (c). Each square is formed from two lower energy crosspeaks, and two higher energy crosspeaks, and the peaks used in each square are distinct. This allows us to group the spectral peaks into two families, where peaks in a single family are coupled, and no coupling is observed between different families. Using this, we conclude that each family of peaks corresponds to a different type of SiV center. Additionally, the MDCS spectrum shows some inhomogeneity, which could be due to microscopic strain fluctuations [62] or interactions between nearby SiV centers [14].

To identify the origin of the two families of SiV centers, we can appeal to spectral peak polarization dependence. While the MDCS spectra can be used for this, it is easier to compare linear spectra, like the TPC spectra shown in Figure 4.3 (a). Note that the relative peak strengths of the two families of peaks under different polarizations of incident light are very different. This suggests that the two families of SiV centers are oriented differently in the diamond lattice. By relating the possible orientations of SiV centers in our sample to the
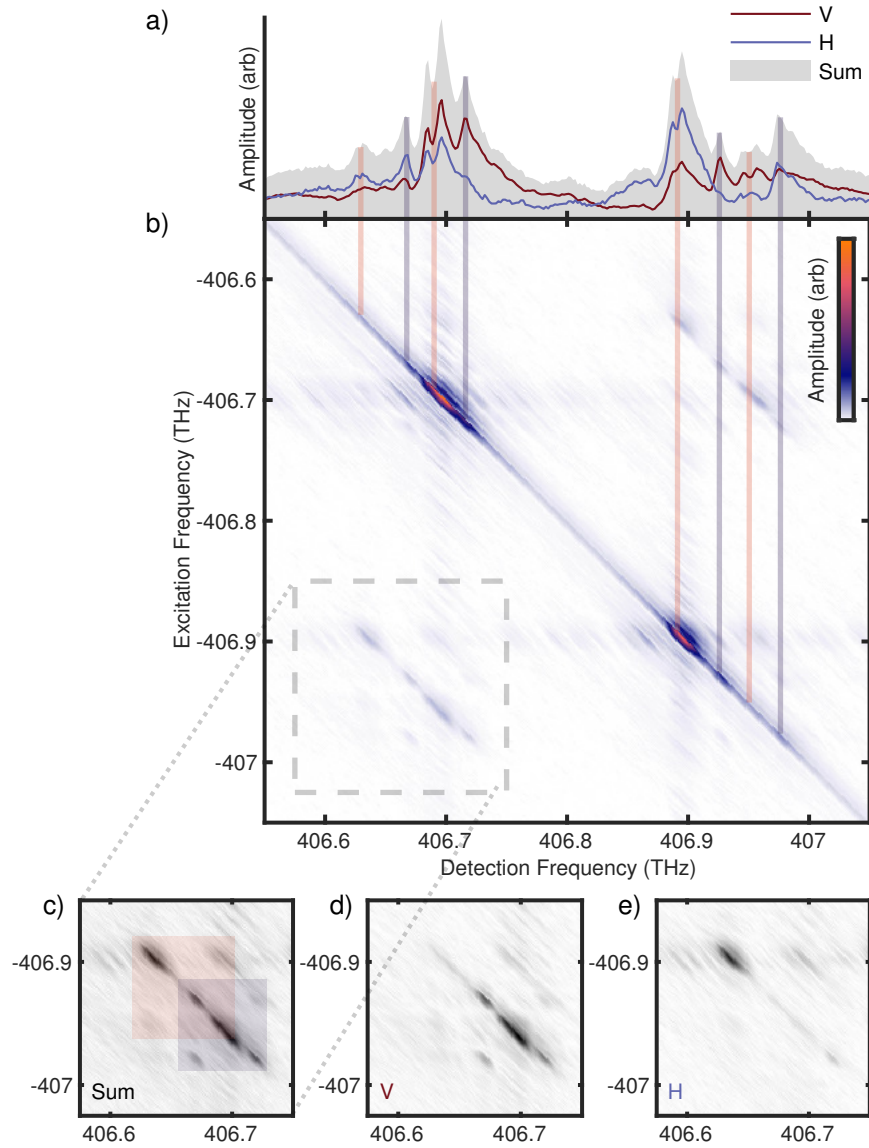
Figure 4.3: (a) TPC spectra of the SiV ZPL, including vertical and horizontal polarizations of the incident laser and their sum, taken at a single point on the sample. (b) A rephasing MDCS spectrum of the SiV ZPL, taken as the sum of spectra using both vertical and horizontal polarizations. The orange and purple vertical lines highlight the peaks corresponding to the two orientation families. (c-e) More detail of the outlined section in the MDCS spectrum, including both vertical and horizontal components. In (c), the crosspeak families are highlighted.

polarization selection rules shown in Figure 3.7, we find that the two sets of peak families correspond to the in-plane and out-of-plane orientations in Figure 4.2 (b). While it may be feasible to group the peaks into families based solely on polarization data, this would become increasingly difficult for higher amounts of strain, and the crosspeaks in the MDCS spectrum are easier to interpret and give a higher degree of certainty.

The peaks corresponding to these families are indicated in Figure 4.3 (a-b) using orange and purple vertical lines, corresponding to the in-plane and out-of-plane families. In the scans seen here, we do see additional splitting of the in-plane peaks. The specific in-plane orientation can be determined with additional linearly polarized spectra.

4.2.2 Strain Calculation

While the analysis of the previous section justifies the necessity of having two different color-center families, it does not yet explain the origin of the different families' peak shifts. We propose that the source of these shifts is due to strain intrinsic to our sample, mainly because the shifts are different for different SiV orientations. By assuming this hypothesis is true, we can solve for the full strain tensor in our sample.

Here we can apply the work completed by Meesala, et al. [45] and discussed in Section 3.3.2. They derived Equation 3.7 relating the four spectral peaks to the six strain tensor indices local to a given SiV center, using six strain susceptibility parameters. For convenience we have reproduced Equation 3.7 here [45]

$$
\begin{aligned}
\Delta_{\text{ZPL}} &= \Delta_{\text{ZPL},0} + \left(t_{\parallel,\text{es}} - t_{\parallel,\text{gs}}\right)\varepsilon'_{zz} + \left(t_{\perp,\text{es}} - t_{\perp,\text{gs}}\right)\left(\varepsilon'_{xx} + \varepsilon'_{yy}\right), \\
\Delta_{\text{gs}} &= \sqrt{\lambda^2_{\text{SO,gs}} + 4\left(d_{\text{gs}}\left(\varepsilon'_{xx} - \varepsilon'_{yy}\right) + f_{\text{gs}}\varepsilon'_{zx}\right)^2 + 4\left(-2d_{\text{gs}}\varepsilon'_{xy} + f_{\text{gs}}\varepsilon'_{yz}\right)^2}, \qquad (4.1) \\
\Delta_{\text{es}} &= \sqrt{\lambda^2_{\text{SO,es}} + 4\left(d_{\text{es}}\left(\varepsilon'_{xx} - \varepsilon'_{yy}\right) + f_{\text{es}}\varepsilon'_{zx}\right)^2 + 4\left(-2d_{\text{es}}\varepsilon'_{xy} + f_{\text{es}}\varepsilon'_{yz}\right)^2}.
\end{aligned}
$$

They combined these equations with experimental data and simulated strain tensor data to fit for the strain susceptibility parameters. In this work, we instead used experimental data

and the strain susceptibility parameters to estimate the strain tensor.

Note in Equation 4.1 that the expressions for Δ_{gs} and Δ_{es} are linearly dependent, as the ground state and excited state splitting respond similarly to strain. Recall that these equations are given in the SiV reference frame, which is depicted in Figure 3.5 (b). Since there are four different orientations of SiV centers in four distinct strain environments, we must first rotate these equations into a common basis. We choose the crystal basis depicted in Fig. 3.5 (a), which gives the rotated strain tensor elements in Appendix A. The results are substituted into Equation 4.1, yielding twelve total equations, eight of which are independent. Since (in the crystal basis) there are six strain tensor indices, these equations are overconstrained and we can use them to solve for the full strain tensor.

We took a series of TPC spectra at 23 locations on our sample, as shown in Figure 4.4 (b). These locations lie along a single line, with a gap in the middle where the implantation density is lower and reliable peak locations and strain estimates could not be measured. Slight shifts in the frequencies of the spectral peaks can be seen.

To use these data to solve for the strain, we first used the techniques in Section 4.2.1 to identify the peaks in our linear spectra (several MDCS spectra were collected at select locations to help with this). The peaks were fitted to find the locations of all 16 spectral peaks for each scan, taking advantage of both vertical and horizontal polarization spectra, since some peaks are more visible on a given polarization. In cases where two peaks could not be resolved (which sometimes occurs for two in-plane or two out-of-plane peaks), a single frequency was reported.

Next, we used Equation 4.1 to find analytical expressions for the frequencies of the 16 spectral peaks as a function of the six strain tensor indices in the crystal basis, $p_i^{\mathrm{calc}}(\varepsilon)$. We estimated the error (standard deviation) of our measured peaks p_i^{meas} to be $\sigma = 2\,\mathrm{GHz}$. This gives us an expression for χ^2,

$$\chi^2 = \sum_{i=1}^{16} \frac{\left(p_i^{\mathrm{meas}} - p_i^{\mathrm{calc}}(\varepsilon)\right)^2}{\sigma^2}. \tag{4.2}$$
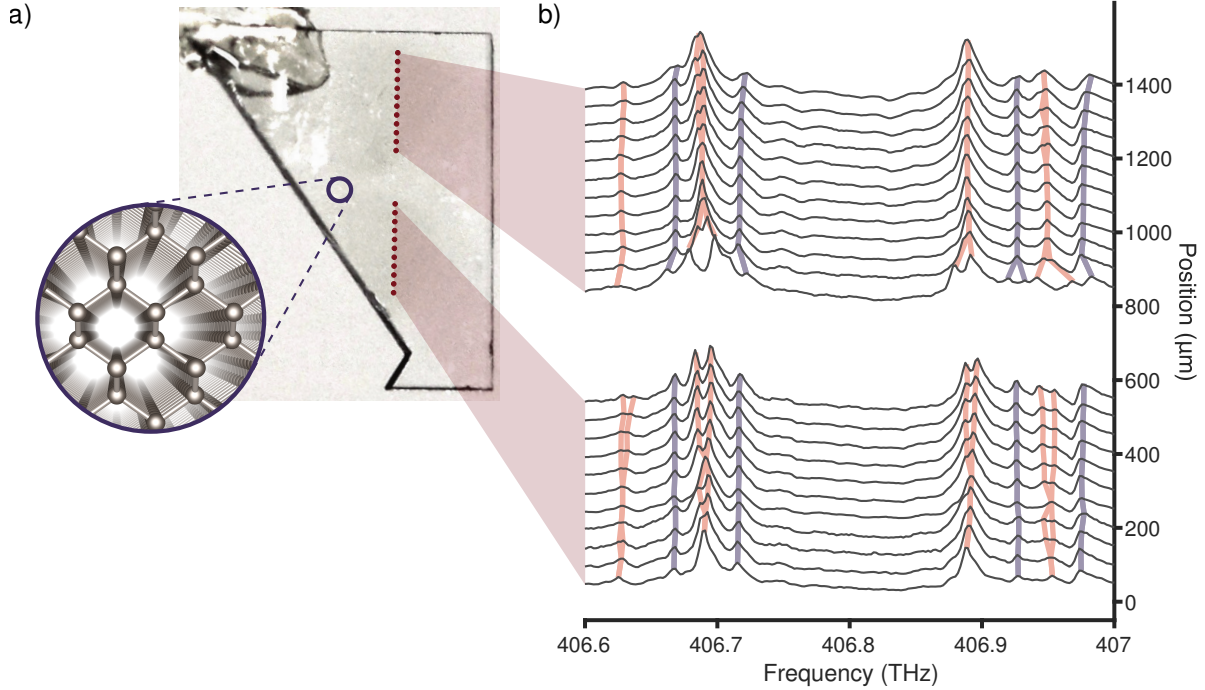
Figure 4.4: (a) An image of the sample illustrating both the locations of the 23 linear spectra used in the strain calculation, as well as the (110) crystal orientation [46]. (b) A series of TPC spectra, summing both horizontal and vertical polarizations. The centers of each peak are highlighted.

Next we found the strain tensor ε, or equivalently the six strain tensor indices, such that χ^2 is minimized. This tensor is our solved result[1].

To estimate the error in the calculation we note that if the error in our peak locations is random, then the χ^2 value from Equation 4.2 should indeed follow a chi-square distribution with 16 degrees of freedom for the true value of the strain tensor. Thus, there is a 90% chance that $\chi^2 < 23.5$. We explored the parameter space local to our solved strain tensor to find the range of strain tensors such that χ^2 is less than the desired value.

The strain-solving algorithm was also tested on simulated data. Peaks were generated with Equation 4.1 using random values for the strain tensor indices. Random errors were added to these peak values, and we attempted to recover the original strain tensor indices using the algorithm above. The algorithm behaved as expected and produced simulated

[1]Source code available at https://github.com/chocokels/strain-solving.

results that were within the range of observed strain values. The algorithm begins to break down as the shear strain tensor index ε_{xy} becomes large (greater than 0.8×10^{-5}).

4.2.3   Strain Results

Extracted strain tensor results are shown in Figure 4.5. Before drawing conclusions from these results, some limitations with the data should be noted. First, the values of the normal strain tensor indices are dependent on the mean ZPL frequency at zero strain, or $\Delta_{\text{ZPL,0}}$. We did not take a direct measurement of this, but we estimated it to be 406.795 THz. However, we find that changing this value results in a constant offset of the normal strain tensor indices ε_{xx}, ε_{yy} and ε_{zz}, and that their relative values are preserved. Next, we encountered a sign ambiguity for small values of ϵ_{xy}, and so we have elected to plot the absolute value of this parameter in Figure 4.5 instead of its sign-dependent form. Future work could attempt to resolve this sign ambiguity in a given sample by observing peak shifts due to ϵ_{zx} strain values that have been intensionally applied to calibrate the measurement. For all indices, the error bars in Figure 4.5 are only meant to represent error due to random error in the peak locations. They do not account for systematic errors, such as errors in the strain susceptibility parameters listed in Equation3.8. We estimate that the error due to the strain susceptibility parameters is less than 0.1×10^{-5} for the normal strain tensor indices and less than 0.03×10^{-5} for the shear strain tensor indices.

Despite these limitations, we are sensitive to strain differences of 2×10^{-5} to 3×10^{-5}, and we do see a varying strain in our sample. The normal strain indices are nonzero, and these values appear to vary across the sample. While we do not see statistically significant magnitudes for the shear strain tensor indices ε_{xy} and ε_{yz}, the shear strain tensor index ε_{zx} does show statistically significant variation.

Previous strain measurements [45] observe shifts in single SiV centers. By contrast, these measurements are taken on an ensemble of SiV centers, as mentioned in Section 4.1.1. This means we measure the strain tensor averaged over the area and depth of the laser spot,
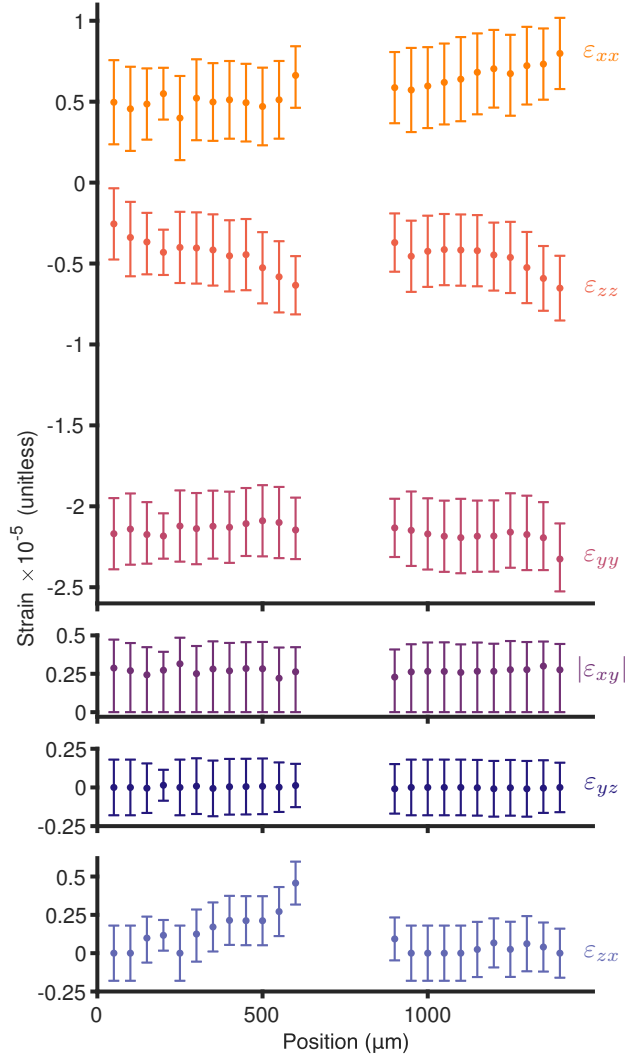
Figure 4.5: Calculated strain tensor indices across the points shown in Figure 4.4. The first plot shows the normal strain tensor indices, ε_{xx}, ε_{yy}, and ε_{zz}. The following three plots show the shear strain tensor indices, ε_{xy} (for which positive values are plotted due to a sign ambiguity), ε_{yz} and ε_{zx}. 90% confidence intervals are shown.

rather than at specific centers. Note that this variation in strain within a region is also different from the strain fluctuations of individual SiV centers proposed in Reference [62], as the latter concerns individual SiV centers in highly strained environments.

The source of this strain is likely due to the implantation and annealing processes, although it has been established that diamond, natural or otherwise, has some degree of strain due to existing defects [36]. As mentioned in Section 4.1.2, our sample has a rather high

number density of implanted silicon of $7.5 \times 10^{18}\,\mathrm{cm}^{-3}$. This density corresponds to about one silicon atom for every 2.3×10^4 carbon atoms. If we assume, as an approximation, implanting the silicon does not increase the size of the sample, but merely pushes the atoms uniformly closer together, then we can estimate the normal strain as -1.4×10^{-5}. While this simple estimation does not take into account many complexities of the system, it does agree with our experimental values to within an order of magnitude.

4.3   Conclusion and Outlook

By analyzing both MDCS and TPC measurements of SiV centers, we were able to measure the full strain tensor of our sample. We measure a nonzero strain, which varies across the sample. This strain is most likely due to the large amount of implanted silicon in our sample. One possible future direction would be to take measurements on a variable density sample, to further measure the relationship between implantation density and strain. In addition, the depth-dependent strain tensor could be studied using a sample containing thin layers of implanted SiV centers or a more tightly focused beam spot. Modifications to the experiment could be implemented or other spectroscopic techniques could be used to improve sensitivity and accuracy. This work may also be useful in using SiV centers in diamond, or other color centers with similar symmetries, as a strain gauge, potentially in a diamond anvil cell or atomic force microscope tip.

CHAPTER 5

Computationally Simulating

Multidimensional Coherent Spectroscopy

This chapter will discuss the code I have written to simulate MDCS spectra. It consists of two main functions, with one to generate Feynman diagrams and the other to perform the simulation. My code is not the most sophisticated MDCS simulation code [56, 57]; it does not account for finite pulse effects [60], for instance. However, its strength lies in its simplicity while still being flexible in the types of spectra and systems it can simulate. It can compute spectra quickly, and allows for arbitrary pulse sequences and energy level diagrams. All code is written in MATLAB (although there is also a version of the Feynman diagrammer in Python), and is available on Github[1].

Section 5.1 will focus on the Feynman diagrammer, which generates valid Feynman diagrams for a given system and pulse sequence. These Feynman diagrams can be used to generate MDCS spectra, as will be described in Section 5.2. Each section will describe both how to use the code and how it works. The code will ultimately be used in Chapter 6.

5.1 Feynman Diagrammer

The logical nature by which Feynman diagrams are formed, as described in Section 2.1.2 lends itself well to automation. While the initial goal of this code was to tabulate all valid

---

[1] https://github.com/chocokels/feynman-finder

rephasing Feynman diagrams for the SiV center, the generalized final product is useful for a variety of other systems and signal pathways.

The Feynman diagrammer `FeynmanFinderFunc` takes as input an arbitrary energy level diagram, a starting state, a signal pathway, and a detection scheme, and outputs all possible Feynman diagrams. It accomplishes this through recursion.

5.1.1 Using the Feynman Diagrammer

To implement arbitrary energy level diagrams, we use directed graphs. Each node on the graph represents a single state, and the edges represent the possible transitions between these states. The directions of the edges should point from lower energy to higher energy states. An example energy level diagram and corresponding directed graph are depicted in Figure 5.1. To implement the graphs, we use MATLAB's `digraph` object. This allows nodes to be given names, which is convenient for identification and readability.

The first two arguments of `FeynmanFinderFunc`, named `ket` and `bra`, are the names for both the starting ket and bra as character arrays. The following argument `graph` is the directed graph representing the energy level structure.

The next argument `eta` represents the signal pathway or, using the symbology of Equation 2.27, the conjugations η of the pulses. This is given as a vector array. Each element is either `1` for an unconjugated pulse, or `-1` for a conjugated pulse. As an example, `[-1 1 1 -1]` should be used for rephasing spectra, and `[1 1 -1 -1]` should be used for double quantum
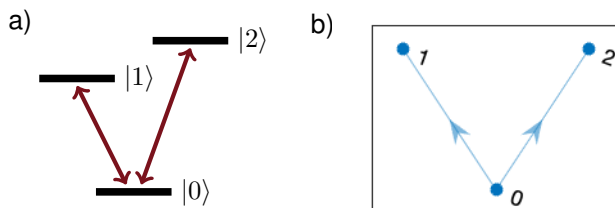
Figure 5.1: (a) The energy level digram for a V-shaped three-level system. (b) The corresponding directed graph.

60

spectra. There are no restrictions regarding the length of `eta`, so higher order spectra with more than four interactions [72, 40, 43] can be processed.

Finally, the last argument `heterodyne` indicates the detection scheme to be used. It should equal `1` for heterodyne detection and `0` for photoluminescence detection.

The output `feyn` of the function is a cell array of structure arrays, where each structure array element of the cell array represents a single Feynman diagram. Each structure array has four fields. The first two, `ket` and `bra`, are cell arrays of the kets and bras of the Feynman diagram, respectively, listed from bottom to top. Next is `sign`, which represents the pulse conjugations, and is simply a copy of `eta`. Last is `side`, which represents the side ζ of the interaction, `1` for left and `-1` for right.

There is an additional function, `PrintFeynman`, which takes a cell array of Feynman diagrams as input, and prints a visual representation of the Feynman diagrams. To simplify the output as text, de-excitation interactions, or interactions with arrows pointed away from the center of the diagram, are displayed one row below their expected position.

As an example, we will consider the rephasing pathway for the V-shaped three-level system depicted in Figure 5.1. We can compute the Feynman diagrams using

```
graph = digraph([1,1],[2,3]);        % Define graph
graph.Nodes.Name = {'0' '1' '2'}';   % Name nodes
eta = [-1 1 1 -1];                    % Rephasing
feyn = FeynmanFinderFunc('0','0',graph,eta,1);
```

We can view a single element of the cell array, both as a structure array, and using the function `PrintFeynman`

```
>> feyn{1}
ans =
  struct with fields:
      ket: {'0'  '0'  '1'  '1'  '0'}
```

61

```
    bra: {'0'  '1'  '1'  '0'  '0'}

   sign: [-1 1 1 -1]

   side: [-1 1 -1 1]

>> PrintFeynman(feyn(1));

 |0><0|

\|1><0|

 |1><1|/

/|0><1|

 |0><0|\
```

5.1.2 Implementation

The Feynman diagrammer uses recursion to achieve a flexible implementation. Each call of `FeynmanFinderFunc` will find the possibilities for one row of the Feynman diagram. For each of these possibilities, it will call `FeynmanFinderFunc` for the remaining interactions. This process is illustrated in Figure 5.2. To increase readability, in this section, we will summarize the content of `FeynmanFinderFunc` as pseudocode. We will divide the code into three sections. In the first, we have the terminating base case, in which there are no remaining interactions. In the second, we find all possible Feynman diagrams that satisfy the given conditions assuming an interaction from the left, and in the third, we do the same thing assuming an interaction from the right.

To start with, we will consider the case in which the input `eta` is empty, meaning there are no remaining interactions.

```
if eta is empty
    if the ket and bra are equal, and either heterodyne detection or the
    current (final) state is not a ground state
        return a Feynman diagram using:
```
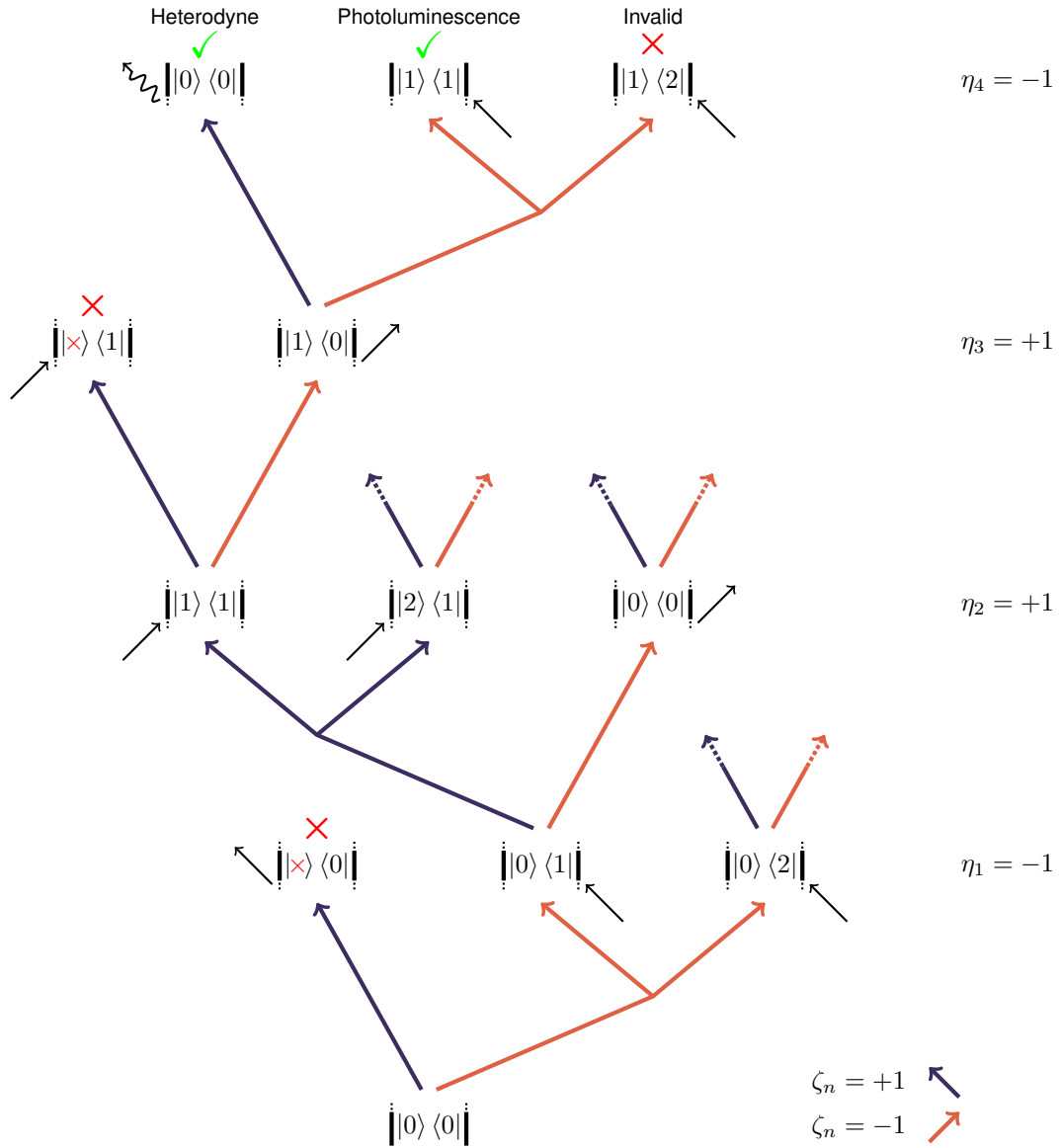
Figure 5.2: A schematic illustrating the operation of the Feynman diagrammer for the example computed in Section 5.1.1. It should be read from bottom to top, and each row represents one call of the recursive function which determines one row of the Feynman diagram. Note that not all possible outcomes are shown due to space constraints.

```
            current ket and bra as ket and bra arrays

            empty arrays as sign and side

    else

        return an empty cell array

    end
```

In this case, we have to start by checking that the Feynman diagram is valid. We want the system to end up in a population, so the input ket and bra should be equal. If we are using photoluminescence detection, we also want to check that this final population state is not a ground state, since otherwise there would be no photoluminescence to measure. If both of these conditions are met, we do have a valid Feynman diagram, and should begin the process of outputting our result. If the conditions are not met, no Feynman diagrams are returned.

If there are remaining interactions, we will first assume that the next one is from the left, which is represented by the purple arrows in Figure 5.2.

```
    else

        feyn = an empty cell array to store possible Feynman diagrams

        % Assume an interaction from the left

        if the interaction is conjugated

            states = possible de-excitations of the current ket

        elseif this is not the final interaction using heterodyne detection

            states = possible excitations of the current ket

        else

            there are no valid states

        end

        for each possible state

            next = the output of FeynmanFinderFunc with state as the ket and
                    eta without its first element
```

```
for each Feynman diagram in next

    modify the Feynman diagram:

        append current ket to the beginning of ket array

        append current bra to the beginning of bra array

        append current sign to the beginning of signs array

        append current side to the beginning of sides array

    end

    append this modified Feynman diagram to feyn

end
```

With an interaction from the left, we know that the ket will change as a result. Thus we use the conjugation of the pulse to determine if the ket will undergo excitation or de-excitation. Next, we look to the directed graph representing the energy level diagram to find the possible kets after the interaction. We also verify that the final interaction with heterodyne detection is a de-excitation, corresponding to the emitted signal. We apply `FeynmanFinderFunc` recursively, with this new ket as the starting ket, and without the first interaction. This will return a cell array of valid Feynman diagrams, which we will modify by adding the information corresponding to the current interaction.

Finally, we will assume that the next interaction is from the right, which is represented by the orange arrows in Figure 5.2.

```
% Assume an interaction from the right
if the interaction is unconjugated
    states = possible de-excitation of the current bra
elseif this is not the final interaction using heterodyne detection
    states = possible excitation of the current bra
else
    there are no valid states
```

```
        end

    for each possible state

        next = the output of FeynmanFinderFunc with state as the bra
                and eta without the first element

        for each Feynman diagram in next

            modify the Feynman diagram:

                append current ket to the beginning of kets array

                append current bra to the beginning of bras array

                append current sign to the beginning of signs array

                append current side to the beginning of sides array

        end

        append this modified Feynman diagram to feyn

    end

    return feyn

end
```

This proceeds like the previous section with one main difference: since the interaction is from the right, the bra will be changed instead of the ket.

5.2   Simulating Spectra

With the Feynman diagrams computed as in Section 5.1, we can now proceed with simulation of MDCS spectra. This simulation code, `SimulateMDScan`, will compute the time domain data for each Feynman diagram individually. The final result will be obtained by adding the individual data sets, and a spectrum in terms of frequency can be found by taking the Fourier transform.

5.2.1 Using the Simulator

The function `SimulateMDScan` has a total of four required inputs. The first of these, `ts`, holds the time delay information. It is a cell array of length $N - 1$, where N is the total number of interactions. Each element in the cell array is a vector array of time delays, where the first element corresponds to the first time delay, the second element corresponds to the second time delay, and so on. The values of the individual vector arrays should correspond to the desired probed time delays, and the length corresponds to the number of data points along that axis. Note that the length of the cell array should be one less than the length of the array `eta` used in `FeynmanFinderFunc`, since the length of `eta` should match the number of interactions.

This implementation means that any variety of MDCS, including but not limited to those described in Section 2.2, can be calculated with a single function. For instance, rephasing spectra can calculated using a single value for the second cell array element (T) and vector arrays for the first and third (τ and t), and zero-quantum spectra can be calculated using a single value for the first cell array element (τ) and vector arrays for the for the second and third (T and t). Higher order spectra can also be computed by adding additional cell array elements for the additional interactions.

The output of `FeynmanFinderFunc` should be included as the input `feyn`. Individual Feynman diagrams can also be used, to view the signal due to only that diagram.

The following input, `Omega`, is equivalent to $\Omega_{a,b}$ as defined in equation 2.2.2. It should be written as a square matrix whose rows and columns correspond to the energy levels, or equivalently the nodes of the directed graph as defined in Section 5.1.1. It can include both the transition frequencies $\omega_{a,b}$ and dephasing terms $\gamma_{a,b}$.

Lastly, to match the indices of `Omega` to the named nodes in the directed graph, the input `graph` should be the directed graph used in `FeynmanFinderFunc`.

There is an additional optional argument `inhom`, and its use and implementation are discussed in Appendix B. If nothing is included for the term `inhom`, no inhomogeneous

broadening will be added.

The output `res` of this function is a complex-valued N-dimensional array. Each dimension corresponds to one time axis in `ts`. Each point in the array corresponds to the signal at that collection of time delays.

There is an additional function, `PlotMDCSScan`, which can be used to plot either the time or frequency domain spectra generated from the output of `SimulateMDScan`. It is intended to be used for a two-dimensional dataset, so while any number of interactions is valid, only two of the time delays between them should be varied. The first input, `ts`, is the same cell array inputted into `SimulateMDScan`, and the second input, `dat`, is the corresponding output. If the third input, `four`, is set to `0`, the time domain is plotted, and if it is set to `1`, the data is Fourier transformed and the frequency domain is plotted. Since the data is complex-valued, the final input `compx` indicates how to convert it to a real value, where `0` will use the absolute value, `1` will use the real part, and `2` will use the imaginary part.

As an example, we will consider the V-shaped three-level system from Section 5.1.1. We will also assume that `graph` and `feyn` are already defined as in that section. We can simulate this system using

```
axtau = (0:2000-1)/3;      % tau axis
axt   = (0:2000-1)/3;      % t axis
ts = [{axtau} {0} {axt}];
freqs = [0 0.67 1.33];     % Freqs measured relative to ground state
gamma =  0.04;             % All states have the same dephasing rates
Omega = ((freqs' - freqs) - 1i * gamma);
res = SimulateMDScan(ts,feyn,Omega,graph);
```

We can also plot the time domain data with

```
PlotMDCSScan(ts,res,0,0);      % For time domain
xlim([0,100]);ylim([0,100]);
```

and the frequency domain spectrum with

```
PlotMDCSScan(ts,res,1,0);        % For frequency domain
xlim([0,2]);ylim([-2,0]);
```

The resulting plots are shown in Figure 5.2.
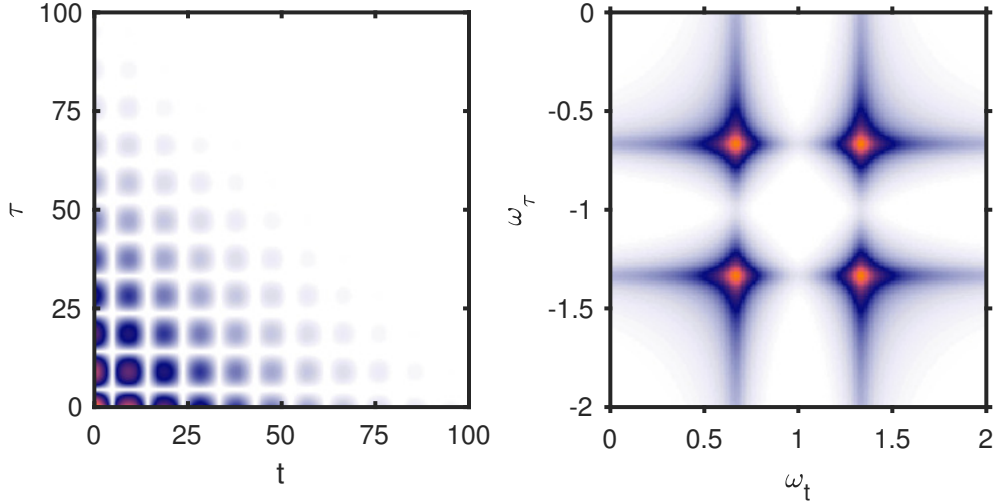
Figure 5.3: The result of a simulation of a V-shaped three-level system, plotted in both the time and frequency domains.

5.2.2   Delta-Function Pulses

Before discussing the simulation code, we will return to the theoretical framework discussed in Section 2.1, and include delta-function pulses. While finite pulse effects do influence the final spectrum [60], we can simplify the mathematics by assuming our pulses are infinitely short [38, pg. 42].

To do this, we first recall Equation 2.27 from Section 2.1.2. We are trying to find the nth order density matrix element

$$\rho^{(n)}_{k_n,b_n;d}(t) = \zeta_{n,d}\frac{i\mu_{\zeta_{n,d}}}{\hbar}e^{i\eta_{n,d}\mathbf{k}_n\cdot\mathbf{x}}\int_{-\infty}^{t}\hat{E}_n^{\eta_{n,d}}(t')\,e^{-i\eta_{n,d}\omega_n t'}e^{-i\Omega_{k_n,b_n}(t-t')}\rho^{(n-1)}_{k_{n-1},b_{n-1},d}(t')\,dt'. \quad (5.1)$$

We will write the envelope of the nth pulse as

$$\hat{E}_n^{\eta_{n,d}}(t) = \mathcal{E}^{\eta_{n,d}} \delta(t).$$ (5.2)

Next, we will substitute this envelope into the equation above, and add a time offset t'_n for the pulse (which will eventually allow our pulses to arrive at different times). This gives

$$\rho_{k_n,b_n;d}^{(n)}(t) = \zeta_{n,d} \frac{i\mu_{\zeta_{n,d}}}{\hbar} e^{i\eta_{n,d}\mathbf{k}_n\cdot\mathbf{x}}$$

$$\int_{-\infty}^{t} \mathcal{E}^{\eta_{n,d}} \delta(t' - t'_n) e^{-i\eta_{n,d}\omega_n(t'-t'_n)} e^{-i\Omega_{k_n,b_n}(t-t')} \rho_{k_{n-1},b_{n-1},d}^{(n-1)}(t') \, dt' \quad (5.3)$$

$$= \zeta_{n,d} \frac{i\mu_{\zeta_{n,d}}\mathcal{E}^{\eta_{n,d}}}{\hbar} e^{i\eta_{n,d}\mathbf{k}_n\cdot\mathbf{x}} e^{-i\Omega_{k_n,b_n}(t-t'_n)} \rho_{k_{n-1},b_{n-1},d}^{(n-1)}(t'_n).$$

Note that we will need to find $\rho_{k_{n-1},b_{n-1},d}^{(n-1)}(t'_n)$. To facilitate repetitive applications of this equation, we will find it more convenient to write it in terms of t'_{n+1} instead of t

$$\rho_{k_n,b_n;d}^{(n)}(t'_{n+1}) = \zeta_{n,d} \frac{i\mu_{\zeta_{n,d}}\mathcal{E}^{\eta_{n,d}}}{\hbar} e^{i\eta_{n,d}\mathbf{k}_n\cdot\mathbf{x}} e^{-i\Omega_{k_n,b_n}(t'_{n+1}-t'_n)} \rho_{k_{n-1},b_{n-1},d}^{(n-1)}(t'_n).$$ (5.4)

Thus, $N-1$ repeated applications of this equation give

$$\rho_d^{(N-1)}(t'_N) = \prod_{n=1}^{N-1} \zeta_{n,d} \frac{i\mu_{\zeta_{n,d}}\mathcal{E}^{\eta_{n,d}}}{\hbar} e^{i\eta_{n,d}\mathbf{k}_n\cdot\mathbf{x}} e^{-i\Omega_{k_n,b_n}(t'_{n+1}-t'_n)}.$$ (5.5)

This is written in terms of t'_n, which is the arrival time of the nth pulse. We can rewrite it in terms of t_n, which we will define as the time difference between pulse n and pulse $n+1$, so $t_n = t'_{n+1} - t'_n$. Thus we write the density matrix elements after N interactions as

$$\rho_d^{(N-1)}(t_1,\ldots,t_{N-1}) = \prod_{n=1}^{N-1} \zeta_{n,d} \frac{i\mu_{\zeta_{n,d}}\mathcal{E}^{\eta_{n,d}}}{\hbar} e^{i\eta_{n,d}\mathbf{k}_n\cdot\mathbf{x}} e^{-i\Omega_{k_n,b_n}t_n}.$$ (5.6)

Next we will assume that only the first $N-1$ interactions are due to the laser interacting with the sample, so the final Nth interaction corresponds to an emitted signal which can be

70

heterodyne detected. In this case, we can use Equation 2.28, and ignore some constants, to find that the measured signal S for a given Feynman diagram d is proportional to

$$S_d^{(N)}(t_1, \ldots, t_{N-1}) \propto i\zeta_{N,d}\mu_{\zeta_{N,d}} \prod_{n=1}^{N-1} i\zeta_{n,d}\mu_{\zeta_{n,d}} e^{-i\Omega_{k_n,b_n} t_n}. \tag{5.7}$$

5.2.3 Implementation

Now that we have built up the required math, we can proceed with using it to simulate spectra. The function `SimulateMDScan` will compute Equation Equation 5.7 for each Feynman diagram input, and find the sum of the results. The function does not currently account for differing values of the dipole elements μ, but this could be added. We will ignore the code which handles inhomogeneous broadening, which is contained within several conditional statements and is explained in Appendix B. As in Section 5.1.2, we will summarize the content of `SimulateMDScan` as pseudocode.

```
for each axis in ts
    reshape each axis so it is a vector array along the nth dimension
end
res = initialized array of zeros
for each Feynman diagram in feyn
    resn = initialized array of ones
    for each of N-1 interactions (excluding emitted signal)
        % Compute using values from this row of this Feynman diagram
        resn = resn * (i * zeta * exp(-i * Omega * nth axis))
    end
    % Compute using values from this emitted signal
    resn = i * zeta * resn
    res = res + resn;
end
```

Most of this function is as expected. The function iterates over each Feynman diagram, and over each interaction. For each iteration, the program computes the interior of the product in Equation 5.7.

Reshaping the time axes in `ts` enables the flexibility of the code. When multiple dimensions are used, the product step is executed element-by-element. Thus, every combination of time delays is calculated, and the final result is an N-dimensional array.

CHAPTER 6

Correlated Dephasing in Multidimensional Spectroscopy of Interacting Systems

As discussed in Chapter 2, many features of a MDCS spectrum are due to the oscillation of various coherent superpositions over time. If we are observing a collection of systems, their phases will gradually desynchronize, resulting in a decaying signal. While there are multiple possible sources for dephasing, our discussion here will be focused on scattering events in the Markovian limit.

Some possible coherences can be due to multiple different energy transitions in the system. For instance, a zero-quantum coherence may be given by the difference of two energy transitions, and a double-quantum coherence may be given by the sum of two energy transitions. This means the dephasing rate of the coherence is affected by both transitions' scattering events. Correlations between these scattering events will similarly affect the dephasing rate.

The effects of correlated and anti-correlated dephasing on a zero-quantum coherence have been previously observed experimentally [21, 8, 67, 47]. For double-quantum or higher order n-quantum coherences, the type and strength of correlations may be able to be controlled by adjusting the distance between multiple interacting systems.

In this chapter, we will use the simulations from Chapter 5 to explore how correlated dephasing affects MDCS spectra, with a particular focus on double-quantum and higher-order n-quantum spectra. In Section 6.1, we will build a mathematical model for Markovian scattering both with and without correlations. We will apply this model first to the simplest

case of double-quantum spectra in Section 6.2. Then we will generalize these results to higher-order n-quantum spectra in Section 6.3. We will finish with some concluding remarks in Section 6.4.

6.1 Correlated Dephasing

One source of dephasing in MDCS scans is scattering events, which can be caused by collisions of the system with atoms or phonons. Such collisions can cause the resonance frequency between two states in the system to fluctuate. If there is a superposition between these two states when a scattering event occurs, the phase of the evolution of the superposition will jump, as is shown in Figure 6.1. If there is a collection of many such states undergoing random scattering events, over time these phase jumps will cause them to dephase with respect to one another.

Under the Markovian limit, we assume that the timescales of these scattering events are smaller than the relevant timescale of the experiment. Thus, we can approximate them with delta functions.

In Section 6.1.1, we will use this to mathematically describe how Markovian dephasing affects the density matrix. With this mathematical framework in place, in Sections 6.1.2 and
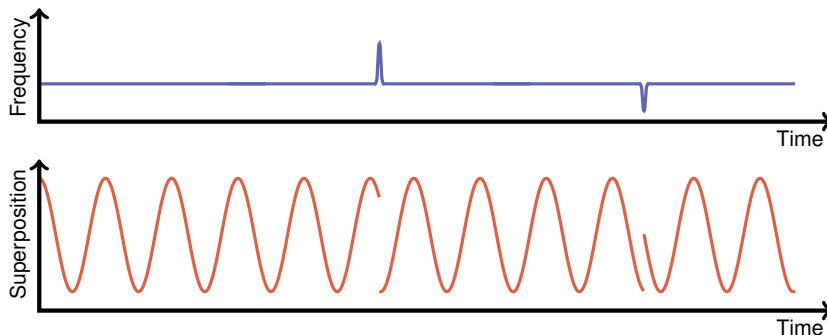
Figure 6.1: A depiction of how Markovian scattering events affect a system. The top plot shows how individual scattering events cause fluctuations in an energy level, or oscillation frequency, in the system. The bottom plot shows how the energy fluctuations create phase jumps in the evolution of a superposition between two states in the system.

6.1.3 we can begin to investigate the effects of correlated dephasing.

6.1.1 Markovian Scattering

Consider the evolution of a density matrix element, as in Equation 2.23, but absent any electric field interactions

$$\frac{\partial \rho_{a,b}^{(n)}}{\partial t} = -i\Omega_{a,b}\rho_{a,b}^{(n)} = -\left(i\omega_{a,b} - i\gamma_{a,b}\right)\rho_{a,b}^{(n)}. \tag{6.1}$$

To account for Markovian scattering, we will use the following derivation from Reference [59, pgs. 86-87]. We can represent the random fluctuations due to Markovian scattering by adding a random frequency shift $\delta\omega_{a,b}(t)$. We will also assume that this frequency shift follows Gaussian statistics. This gives

$$\frac{\partial \rho_{a,b}^{(n)}}{\partial t} = -\left(i\omega_{a,b} + i\delta\omega_{a,b}(t) - i\gamma_{a,b}\right)\rho_{a,b}^{(n)}. \tag{6.2}$$

We can integrate this to get

$$\rho_{a,b}(t) = \rho_{a,b}(0)\exp\left(-\left(i\omega_{a,b} + \gamma_{a,b}\right)t - i\int_0^t dt'\, \delta\omega(t')\right). \tag{6.3}$$

The integral $\int_0^t dt'\, \delta\omega(t')$ would represent the frequency drift over time of a single system. We care about the dephasing of an ensemble of systems, which all experience different scattering events. Thus, to find the dephasing of the ensemble, we perform an ensemble average.

Isolating just the integral term, and expanding it as a series, we see that

$$
\left\langle \exp\left(-i \int_0^t dt' \, \delta\omega\left(t'\right)\right)\right\rangle
$$
$$
= \left\langle 1 - i \int_0^t dt' \, \delta\omega\left(t'\right) - \frac{1}{2} \int_0^t dt' \int_0^t dt'' \, \delta\omega\left(t'\right)\delta\omega\left(t''\right) + \cdots \right.
$$
$$
\left. + \frac{(-i)^{2n}}{(2n)!} \int_0^t dt_1 \cdots \int_0^t dt_{2n} \, \delta\omega\left(t_1\right)\cdots\delta\omega\left(t_{2n}\right) + \cdots \right\rangle \quad (6.4)
$$
$$
= 1 - i \int_0^t dt' \, \left\langle \delta\omega\left(t'\right)\right\rangle - \frac{1}{2} \int_0^t dt' \int_0^t dt'' \, \left\langle \delta\omega\left(t'\right)\delta\omega\left(t''\right)\right\rangle + \cdots
$$
$$
+ \frac{(-i)^{2n}}{(2n)!} \int_0^t dt_1 \cdots \int_0^t dt_{2n} \, \left\langle \delta\omega\left(t_1\right)\cdots\delta\omega\left(t_{2n}\right)\right\rangle \cdots .
$$

Since the fluctuations are as likely to be positive as negative, $\left\langle \delta\omega\left(t'\right)\right\rangle = 0$. For the later terms, we need to find $\left\langle \delta\omega\left(t'\right)\delta\omega\left(t''\right)\right\rangle$. If we assume Markovian scattering, then the scattering events are infinitely fast, and the frequency shift for differing times $t' \neq t''$ is uncorrelated. Thus this average will be nonzero only when $t' = t''$. We can write it as

$$
\left\langle \delta\omega\left(t'\right)\delta\omega\left(t''\right)\right\rangle = 2\gamma_{\mathrm{ph}}\delta\left(t' - t''\right), \quad (6.5)
$$

where γ_{ph} represents the amplitude of the fluctuations. Using this we can compute the second term Equation 6.4 as

$$
-\frac{1}{2} \int_0^t dt' \int_0^t dt'' \, \left\langle \delta\omega\left(t'\right)\delta\omega\left(t''\right)\right\rangle = -\gamma_{\mathrm{ph}} \int_0^t dt'' \, \delta\left(t' - t''\right) = -\gamma_{\mathrm{ph}}t. \quad (6.6)
$$

If we assume Gaussian statistics, we can compute the later terms by grouping $\left\langle \delta\omega\left(t_1\right)\cdots\delta\omega\left(t_{2n}\right)\right\rangle$ into distinguishable pairs like that in Equation 6.5. Since this cannot be done for the odd terms in Equation 6.4, those terms vanish. The number of arrangements of $2n$ terms into n pairs is $\frac{(2n)!}{2^n}$. Since we want distinguishable arrangements, we divide this

by $n!$. Thus, we can compute the even terms of Equation 6.4 as

$$\frac{(-i)^{2n}}{(2n)!} \int_0^t dt_1 \cdots \int_0^t dt_{2n} \left\langle \delta\omega\left(t_1\right) \cdots \delta\omega\left(t_{2n}\right) \right\rangle$$
$$= \frac{(-1)^n (2n)! \left(2\gamma_{\mathrm{ph}}\right)^n}{(2n)! \, n! \, 2^n} \int_0^t dt_1 \cdots \int_0^t dt_{2n} \, \delta\left(t_1 - t_2\right) \cdots \delta\left(t_{2n-1} - t_{2n}\right) \quad (6.7)$$
$$= \frac{\left(-\gamma_{\mathrm{ph}} t\right)^n}{n!}.$$

Using this, we can collapse Equation 6.4 back into an exponential, giving

$$\left\langle \exp\left(-i \int_0^t dt' \, \delta\omega\left(t'\right)\right) \right\rangle = \sum_{n=0}^{\infty} \frac{\left(-\gamma_{\mathrm{ph}} t\right)^n}{n!} = \exp\left(-\gamma_{\mathrm{ph}} t\right). \quad (6.8)$$

Our integrated expression from Equation 6.3 therefore becomes

$$\rho_{a,b}\left(t\right) = \rho_{a,b}\left(0\right) \exp\left(-\left(i\omega_{a,b} + \gamma_{a,b} + \gamma_{a,b}^{\mathrm{ph}}\right)\right) t. \quad (6.9)$$

Thus, the energy fluctuations due to Markovian scattering can be modeled as another dephasing term in the evolution of the density matrix. We can easily fit it into our model of MDCS in Chapter 2 and our simulations in Chapter 5 by modifying our definition of $\Omega_{a,b}$ in Equation 2.2.2 to be

$$\Omega_{a,b} = \omega_{a,b} - i\gamma_{a,b} - i\gamma_{a,b}^{\mathrm{ph}}. \quad (6.10)$$

6.1.2 Correlations Between Two Transitions

If we have a system with multiple energy transitions, it is possible that the energies of the different transitions are correlated. If one transition fluctuates, the other will fluctuate similarly (for a specific system). Anticorrelation, where if one transition fluctuates up, the other will fluctuate down, is also possible. Correlated dephasing has been previously observed in excitons in GaAs [21], GaAs quantum wells [8, 67], and InAs quantum dots [47].

Figure 6.2: (a) A V-shaped three-level system. (b) An illustration of the effects of correlated ($\rho = 1$), uncorrelated ($\rho = 0$), and anticorrelated ($\rho = -1$) dephasing processes on the energy levels of this system.

All three of these instances concern a V-shaped three-level system, such as that in Figure 6.2 (a). To simplify the problem, we will measure all fluctuations relative to the ground state. Correlated, uncorrelated, and anticorrelated scattering events for this system are shown in Figure 6.2 (b). We will assume (for now) that the coherences $|0\rangle \langle 1|$ and $|0\rangle \langle 2|$ have equal scattering dephasing rates $\gamma_{0,1}^{\text{ph}} = \gamma_{0,2}^{\text{ph}}$. We wish to find the dephasing rate of the zero-quantum coherence $|1\rangle \langle 2|$, which evolves at frequency $\omega_{2,1} = \omega_{2,0} - \omega_{1,0}$.

For the uncorrelated case, $\rho = 0$, we see that the fluctuations of the two energy levels are independent. We would expect the zero-quantum coherence to dephase twice as fast as the single-quantum coherences, since the fluctuations will be twice as frequent for the zero-quantum coherence. This expectation can be written mathematically as

$$\gamma_{1,2}^{\text{ph}} = \gamma_{0,1}^{\text{ph}} + \gamma_{0,2}^{\text{ph}} = 2\gamma_{0,2}^{\text{ph}}. \tag{6.11}$$

For the completely correlated case, $\rho = 1$, the fluctuations in the two energy levels are identical. Since $\omega_{2,1} = \omega_{2,0} - \omega_{1,0}$, we have that

$$\delta\omega_{2,1} = \delta\omega_{2,0} - \delta\omega_{1,0} = \delta\omega_{2,0} - \delta\omega_{2,0} = 0. \tag{6.12}$$

Thus, the dephasing of the zero-quantum coherence is not affected by the scattering events,

so

$$\gamma_{1,2}^{\mathrm{ph}} = 0. \tag{6.13}$$

For the completely anticorrelated case, $\rho = -1$, the fluctuations in the two energy levels are exactly opposite. Since $\omega_{2,1} = \omega_{2,0} - \omega_{1,0}$, we have that

$$\delta\omega_{2,1} = \delta\omega_{2,0} - \delta\omega_{1,0} = \delta\omega_{2,0} + \delta\omega_{2,0} = 2\delta\omega_{2,0}. \tag{6.14}$$

Looking at equation 6.5, we see that a factor of two increase in $\delta\omega$ will increase γ_{ph} by a factor of four, so

$$\gamma_{1,2}^{\mathrm{ph}} = 4\gamma_{0,2}^{\mathrm{ph}}. \tag{6.15}$$

These simplistic and intuitive results agree with the general result of Reference [21]

$$\gamma_{1,2}^{\mathrm{ph}} = \gamma_{0,1}^{\mathrm{ph}} + \gamma_{0,2}^{\mathrm{ph}} - 2\rho\sqrt{\gamma_{0,1}^{\mathrm{ph}}\gamma_{0,2}^{\mathrm{ph}}}. \tag{6.16}$$

This equation allows for any $-1 \leq \rho \leq 1$ and $\gamma_{0,1}^{\mathrm{ph}} \neq \gamma_{0,2}^{\mathrm{ph}}$. Additionally, we will provide a more rigorous justification for this equation in Section 6.1.3.

While prior experimental results used systems like the three-level system just discussed, the diamond-shaped four-level system seen in Figure 6.3 (a) is more relevant to this work. In particular, we are concerned with the dephasing rate of the double-quantum coherence.

The effects of scattering events on this system are illustrated in Figure 6.3 (b). We would expect the uncorrelated case to be the same as that of the three-level system, since we similarly see twice as many fluctuations of the double-quantum coherence. For the correlated and anticorrelated cases, we look to the origin of the doubly excited state. The zero-quantum coherence frequency was found by taking the difference of the single-quantum coherences, but the double-quantum coherence frequency is approximately the sum of the single-quantum coherences (minus a term due to the interaction). Thus, we would expect the effects of correlation and anticorrelation on the double-quantum coherence to be opposite those of the
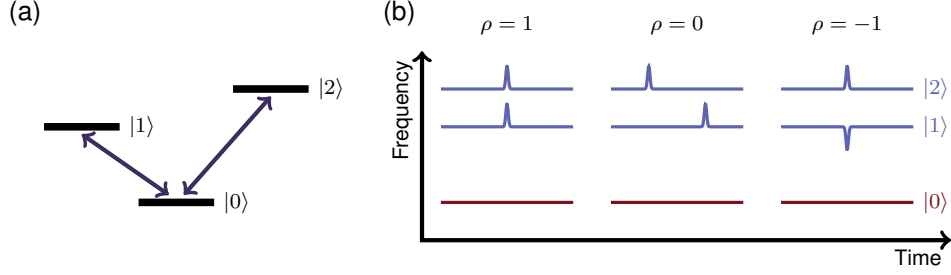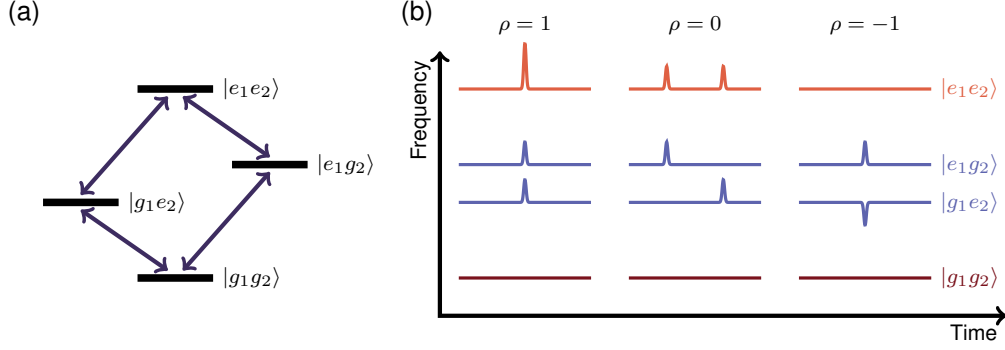
Figure 6.3: (a) A diamond-shaped four-level system. (b) An illustration of the effects of correlated ($\rho = 1$), uncorrelated ($\rho = 0$), and anticorrelated ($\rho = -1$) dephasing processes on the energy levels of this system.

zero-quantum coherence.

Thus, referencing Equation 6.16 we would expect the general equation for the double-quantum dephasing rate to be

$$\gamma^{\mathrm{ph}}_{g_1 g_2, e_1 e_2} = \gamma^{\mathrm{ph}}_{g_1, e_1} + \gamma^{\mathrm{ph}}_{g_2, e_2} + 2\rho\sqrt{\gamma^{\mathrm{ph}}_{g_1, e_1} \gamma^{\mathrm{ph}}_{g_2, e_2}}. \tag{6.17}$$

This equation will also agree with the results of Section 6.1.3.

Equations 6.16 and 6.17 are sufficient to describe all the coherences possible in a diamond-shaped four-level system, which can be probed using double-quantum MDCS. However, we would like to be able to simulate higher-order n-quantum MDCS as well. This will require calculating dephasing rates for coherences which are comprised of more than two single-quantum coherences, so we will need to generalize these results.

6.1.3   Generalized Correlations

In order to generalize this to more complicated energy level structures, we will turn to statistics. Recall that we are assuming that the fluctuations follow Gaussian statistics, and assume that all fluctuations $\delta\omega$ are measured relative to some ground state. We already

know that the mean of these fluctuations is zero

$$\mu_a = \langle \delta \omega_a \rangle = 0. \tag{6.18}$$

We can also find the variance of a single transition, which we would expect to be proportional to the Markovian dephasing rate, as defined in Equation 6.5

$$\sigma_a^2 = \langle (\delta \omega_a - \mu_a)^2 \rangle = \langle \delta \omega_a^2 \rangle \propto \gamma_a^{\text{ph}}. \tag{6.19}$$

If we have two fluctuating states, we can also define their covariance

$$\text{cov}\left(\delta \omega_a, \delta \omega_b\right) = \langle (\delta \omega_a - \mu_a)(\delta \omega_b - \mu_b) \rangle = \langle \delta \omega_a \delta \omega_b \rangle, \tag{6.20}$$

as well as their correlation

$$\rho_{a,b} = \frac{\text{cov}\left(\delta \omega_a, \delta \omega_b\right)}{\sigma_a \sigma_b.} \tag{6.21}$$

Using these, we can define the covariance matrix in a basis of fundamental energy transitions

$$
\begin{aligned}
\boldsymbol{\Sigma} &=
\begin{pmatrix}
\sigma_1^2 & \text{cov}\left(\delta \omega_1 \delta \omega_2\right) & \cdots & \text{cov}\left(\delta \omega_1 \delta \omega_k\right) \\
\text{cov}\left(\delta \omega_2 \delta \omega_1\right) & \sigma_2^2 & \cdots & \text{cov}\left(\delta \omega_2 \delta \omega_k\right) \\
\vdots & \vdots & \ddots & \vdots \\
\text{cov}\left(\delta \omega_k \delta \omega_1\right) & \text{cov}\left(\delta \omega_k \delta \omega_2\right) & \cdots & \sigma_k^2
\end{pmatrix} \\
&=
\begin{pmatrix}
\sigma_1 & & & 0 \\
& \sigma_2 & & \\
& & \ddots & \\
0 & & & \sigma_k
\end{pmatrix}
\begin{pmatrix}
1 & \rho_{1,2} & \cdots & \rho_{1,k} \\
\rho_{1,2} & 1 & \cdots & \rho_{2,k} \\
\vdots & \vdots & \ddots & \vdots \\
\rho_{1,k} & \rho_{2,k} & \cdots & 1
\end{pmatrix}
\begin{pmatrix}
\sigma_1 & & & 0 \\
& \sigma_2 & & \\
& & \ddots & \\
0 & & & \sigma_k
\end{pmatrix},
\end{aligned} \tag{6.22}
$$

and the correlation matrix

$$\mathbf{R} = \begin{pmatrix} 1 & \rho_{1,2} & \cdots & \rho_{1,k} \\ \rho_{1,2} & 1 & \cdots & \rho_{2,k} \\ \vdots & \vdots & \ddots & \vdots \\ \rho_{1,k} & \rho_{2,k} & \cdots & 1 \end{pmatrix}. \tag{6.23}$$

Note that the covariance matrix must be symmetric and positive semi-definite [28, pg. 122]. This restriction is necessary to prevent impossible correlations. For instance, if a and b are fully correlated, and b and c are fully correlated, then it is impossible for a and c to be anticorrelated.

Since the fluctuations follow Gaussian statistics, they can be modeled as a multivariate normal distribution,

$$f\left(\boldsymbol{\delta\omega}\right) = \frac{1}{\sqrt{(2\pi)^k \det \boldsymbol{\Sigma}}} \exp\left(-\frac{1}{2}\boldsymbol{\delta\omega}^T \boldsymbol{\Sigma}^{-1} \boldsymbol{\delta\omega}\right). \tag{6.24}$$

One convenient result of this is that every linear combination of its components $(\delta\omega_1, \ldots, \delta\omega_k)$ is itself normal [28, pg. 123, def. I].

Consider any vector $\mathbf{s}$ of length k. We know that the linear combination $\mathbf{s}^T \boldsymbol{\delta\omega}$ follows normal statistics. We can find its variance by taking [28, pg. 124, thm 3.1]

$$\sigma_{\mathbf{s}}^2 = \mathbf{s}^T \boldsymbol{\Sigma} \mathbf{s}. \tag{6.25}$$

Because we have $\sigma^2 \propto \gamma_{\mathrm{ph}}$, we can get a similar expression for γ_{ph}

$$\gamma_{\mathbf{s}}^{\mathrm{ph}} = \mathbf{s}^T \boldsymbol{\gamma}^{1/2} \mathbf{R} \boldsymbol{\gamma}^{1/2} \mathbf{s}, \tag{6.26}$$

where

$$\gamma^{1/2} = \begin{pmatrix} \sqrt{\gamma_1^{\mathrm{ph}}} & & & 0 \\ & \sqrt{\gamma_2^{\mathrm{ph}}} & & \\ & & \ddots & \\ 0 & & & \sqrt{\gamma_k^{\mathrm{ph}}} \end{pmatrix}. \tag{6.27}$$

Alternatively, we can write this matrix product as

$$\gamma_{\mathbf{s}}^{\mathrm{ph}} = \sum_a \gamma_a^{\mathrm{ph}} + 2 \sum_{a \neq b} s_a s_b \rho_{a,b} \sqrt{\gamma_a^{\mathrm{ph}} \gamma_b^{\mathrm{ph}}}. \tag{6.28}$$

Using this, we can reproduce the results of Section 6.1.2. For instance, if we want to find the dephasing rate of the sum of two energy levels with individual dephasing rates γ_a^{ph} and γ_a^{ph}, then $\mathbf{s} = \begin{pmatrix} 1 \\ 1 \end{pmatrix}$, so

$$\gamma_{a+b}^{\mathrm{ph}} = \gamma_a^{\mathrm{ph}} + \gamma_b^{\mathrm{ph}} + 2\rho_{a,b} \sqrt{\gamma_a^{\mathrm{ph}} \gamma_b^{\mathrm{ph}}}, \tag{6.29}$$

which matches Equation 6.17. Similarly, if we want to find the dephasing rate of the difference of the two energy levels, then $\mathbf{s} = \begin{pmatrix} 1 \\ -1 \end{pmatrix}$, so

$$\gamma_{a-b}^{\mathrm{ph}} = \gamma_a^{\mathrm{ph}} + \gamma_b^{\mathrm{ph}} - 2\rho_{a,b} \sqrt{\gamma_a^{\mathrm{ph}} \gamma_b^{\mathrm{ph}}}, \tag{6.30}$$

which matches Equation 6.16.

6.2 Double-Quantum Results

We begin by investigating the effects of correlated dephasing on a system consisting of two interacting two-level systems using double-quantum MDCS, which was first introduced in Section 2.2.4. This system can be represented as a diamond-shaped four-level system, as shown at the center of Figure 6.4. Note that the doubly excited state is still reduced by an interaction term Δ, as described in Section 2.2.4 and depicted in Figure 2.9. The simulations that follow do include this term, but it is set to be small relative to the other values in the
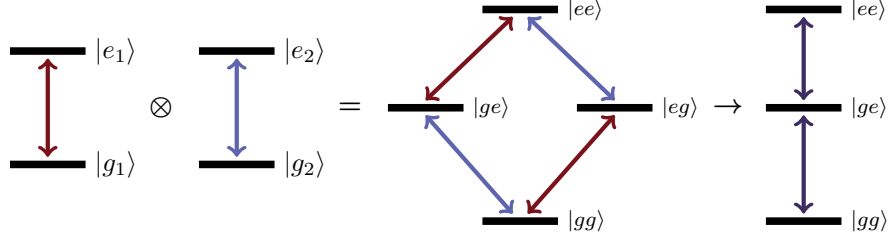
Figure 6.4: Two two-level systems combining to form a diamond-shaped four-level system, which we can represent as a three-level ladder system.

simulation.

We should also be sure to distinguish this work from Reference [42]. This earlier work concerns correlations between the frequencies of interacting systems and how these correlations affect double-quantum lineshapes. Such correlations result in inhomogeneous broadening. The work presented here instead concerns correlations in scattering events, which results in correlations in the dephasing rates of interacting systems. We will set the frequencies of the different transitions to be equal to simplify the problem, but these computations could also be calculated using different frequencies for individual single-quantum coherences, or including inhomogeneous broadening as well.

6.2.1 Double-Quantum Dephasing

To simulate this system, we need an expression for $\mathbf{\Omega}$ as defined in Equation 6.10. In particular, $\boldsymbol{\gamma}_{\mathrm{ph}}$ needs to be written concisely in the basis of the possible system states. Note that this is different from the basis used in the covariance matrix $\mathbf{\Sigma}$. For this system of two interacting two-level systems, the basis for $\mathbf{\Sigma}$ consists of the two transitions of the two individual interacting states, and the basis for $\mathbf{\Omega}$ and $\boldsymbol{\gamma}_{\mathrm{ph}}$ is the four states in the combined four-level system.

Let γ_1 and γ_2 be the dephasing rates of the two individual two-level systems, and ρ be the correlation between the dephasing of these two states, so the correlation matrix $\mathbf{R} = \left(\begin{smallmatrix} 1 & \rho \\ \rho & 1 \end{smallmatrix} \right)$.

Using the results of Equation 6.28, we find

$$\boldsymbol{\gamma}_{\mathrm{ph}} = \begin{array}{c} \\ |gg\rangle \\ |eg\rangle \\ |ge\rangle \\ |ee\rangle \end{array} \overset{\displaystyle \langle gg| \qquad\quad \langle eg| \qquad\qquad \langle ge| \qquad\qquad \langle ee|}{\left(\begin{array}{cccc} 0 & \gamma_1 & \gamma_2 & \gamma_1 + \gamma_2 + 2\rho\sqrt{\gamma_1\gamma_2} \\ \gamma_1 & 0 & \gamma_1 + \gamma_2 - 2\rho\sqrt{\gamma_1\gamma_2} & \gamma_2 \\ \gamma_2 & \gamma_1 + \gamma_2 - 2\rho\sqrt{\gamma_1\gamma_2} & 0 & \gamma_1 \\ \gamma_1 + \gamma_2 + 2\rho\sqrt{\gamma_1\gamma_2} & \gamma_2 & \gamma_1 & 0 \end{array} \right)}. \tag{6.31}$$

Here, the rows and columns are labeled with the kets and bras of the corresponding coherences.

All possible coherences for this system are represented in this matrix. However, not all of them can be reached in a double-quantum signal. In particular, a zero-quantum coherence, such as $|ge\rangle \langle eg|$, will not occur. If we assume $\omega_1 = \omega_2$ and $\gamma_1 = \gamma_2$, then we can treat $|eg\rangle$ and $|ge\rangle$ as a single state, and represent this system by the three-level ladder system as shown in the right side of Figure 6.4. In this case, $\boldsymbol{\gamma}_{\mathrm{ph}}$ can be written as

$$\boldsymbol{\gamma}_{\mathrm{ph}} = \begin{array}{c} \\ |gg\rangle \\ |ge\rangle \\ |ee\rangle \end{array} \overset{\displaystyle \langle gg| \quad\;\; \langle ge| \quad\;\; \langle ee|}{\left(\begin{array}{ccc} 0 & \gamma & (2+2\rho)\,\gamma \\ \gamma & 0 & \gamma \\ (2+2\rho)\,\gamma & \gamma & 0 \end{array} \right)}. \tag{6.32}$$

This simplification reduces the number of Feynman diagrams needed to simulate this system. While not strictly necessary for double-quantum spectra, this simplification will become much more useful for the higher-order n-quantum spectra explored in Section 6.3.1, since as n increases, the number of valid Feynman diagrams increases dramatically.

6.2.2   Double-Quantum Simulations

We can now simulate double-quantum spectra using the dephasing matrix written in and the simulation code described in Chapter 5. Some resulting simulations are shown in Figure 6.5 (a). The frequency axes are defined relative to the frequency difference of one of the

two-level systems, so $\omega_{eg} = 1$. It is assumed that the dephasing due to Markovian scattering events is much greater than other sources of dephasing, so the rate of dephasing is dominated by γ_{ph}. The dephasing due to Markovian scattering for the individual two-level systems for this set of spectra is set to be $\gamma_{\text{ph}} = 0.05\omega_{eg}$. The spectra are taken at differing values of correlation, ρ. We also do not include any inhomogeneous broadening, and all spectra are normalized independently.

As we would expect for this system, all spectra show a single peak with double-quantum frequency of $2\omega_{eg}$ and emission frequency ω_{eg}. However, what is more relevant is the linewidths along the two axes, which are portrayed more clearly in Figure 6.5 (b) and (c).
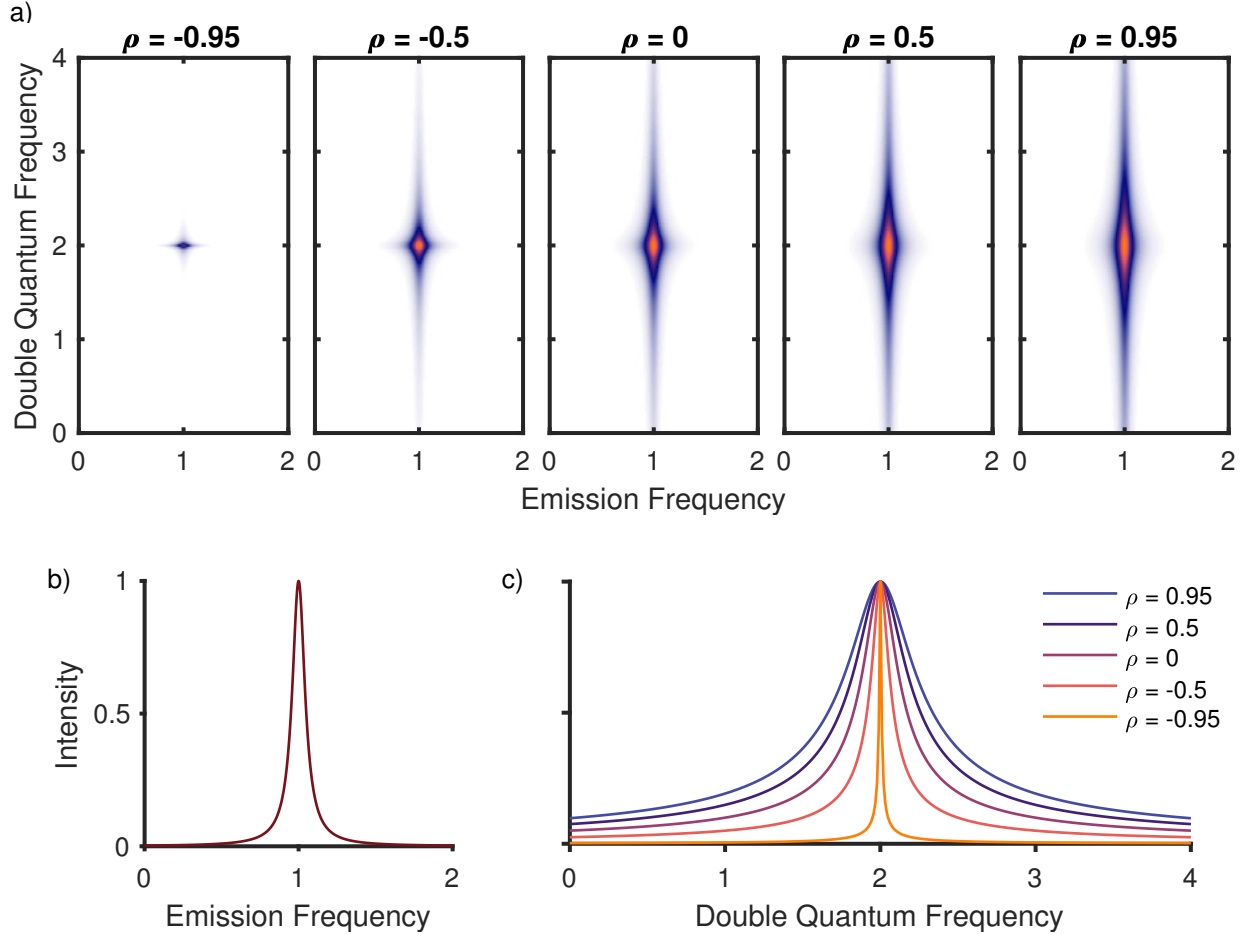
Figure 6.5: (a) Simulated double-quantum spectra at a variety of correlation values. (b) Horizontal cross section of double-quantum spectra at $\omega_T = 2$. (c) Vertical cross section of double-quantum spectra at $\omega_t = 1$.

The linewidth along the emission frequency axis is determined by the rate of dephasing during the t time delay. Since this time delay probes single-quantum coherences, and since the correlation coefficient does not impact these single quantum coherences, the linewidth along the emission frequency axis does not depend on ρ. The linewidth along the double-quantum frequency axis is determined by the rate of dephasing during the T time delay, which probes the double-quantum coherence. We determined above that this dephasing rate is given by $(2 + 2\rho)\gamma$, so the linewidth along the double-quantum axis is strongly affected by γ. In particular, note that when $\rho = -1$ the dephasing rate of the double-quantum coherence becomes 0, and the linewidth becomes arbitrarily small (although in practice it would be limited by other sources of dephasing).

To be more exact, we can mathematically represent the lineshapes of cross sections of the peaks, as plotted in 6.5 (b) (c). The single-quantum coherence has a Lorentzian lineshape, described by

$$I_t(\omega) = \left(\left(\frac{\omega - \omega_{eg}}{\gamma} \right)^2 + 1 \right)^{-1}, \tag{6.33}$$

and the lineshape of the double-quantum coherence is the root of a Lorentzian, as in

$$I_T(\omega) = \left(\left(\frac{\omega - 2\omega_{eg}}{(2 + 2\rho)\gamma} \right)^2 + 1 \right)^{-1/2}. \tag{6.34}$$

6.3 n-Quantum Results

6.3.1 Higher-Order n-Quantum Spectra

In Section 2.2.4 we discussed double-quantum spectra, which are used to probe double-quantum coherences. By allowing the second and third pulses to interact with the system multiple times, higher-order coherences can be observed [72, 40]. Written generally, we can probe a coherence between the ground and nth excited state through n-quantum spectra.

The pulse sequence for an n-quantum scan is shown in Figure 6.6. For a double-quantum
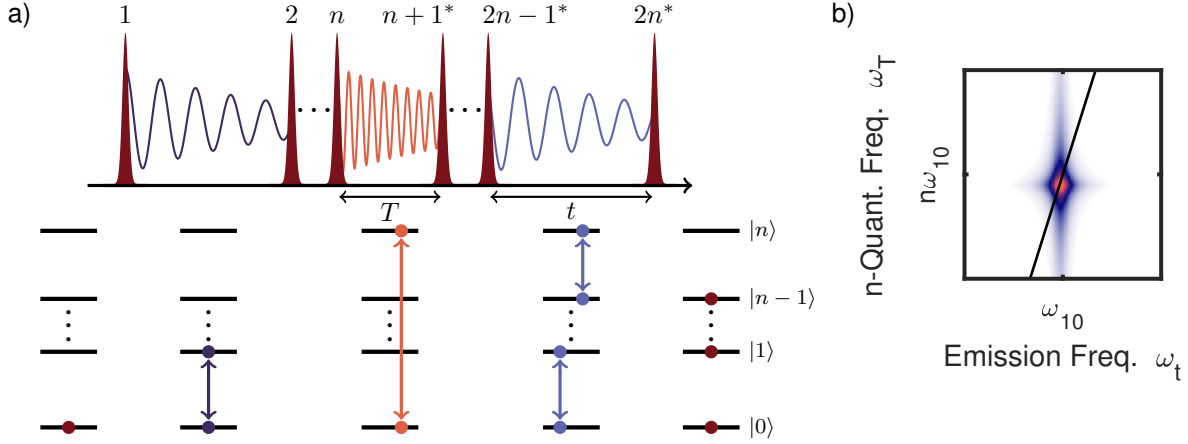
Figure 6.6: (a) A pulse sequence for an n-quantum spectrum. (b) The corresponding n-quantum spectrum.

signal, the first two pulses have the same conjugation, which forces the system into a coherent superposition between the ground and doubly excited states. Similarly, for an n-quantum signal, the first n interactions have the same conjugation, which forces the system into a coherent superposition between the ground and nth excited states. Much like in double-quantum spectra, in n-quantum spectra the later interactions have the opposite conjugation, and can act on the left or right. After the next $n-1$ pulses, the system is in a single-quantum coherence, and the final signal can be detected using the same methods as in Section 2.2.

To remain consistent, we will label the time delay of the n-quantum coherence, which is between the nth and $n+1$th interactions, as T, and time time delay of the final single-quantum coherence, which is between the $2n-1$th and $2n$th interactions, as t. This is shown in Figure 6.6 (a). The frequencies corresponding to these time delays are represented as the axes in the example n-quantum spectrum in Figure 6.6 (b). The plotted diagonal in this spectrum is $\omega_T = n\omega_t$.

Where double-quantum spectra are useful in observing interactions between two nearby systems, n-quantum spectra are able to observe interactions between n nearby systems, such as multi-atom Dicke states [72, 40].

6.3.2 n-Quantum Dephasing

We can make similar simplifications to those in Section 6.2.1 for larger numbers of interacting two-level systems, such as the three-level system shown in Figure 6.7, although again we need a few conditions. First, we need $\omega_1 = \omega_2 = \cdots = \omega_n$ and $\gamma_1 = \gamma_2 = \cdots = \gamma_n$. If all of the $\rho_{a \neq b} = \rho$ are also equal, using Equation 6.28 we can write for a four-level ladder system

$$
\boldsymbol{\gamma}_{\text{ph}} =
\begin{array}{c}
\\
|ggg\rangle \\
|gge\rangle \\
|gee\rangle \\
|eee\rangle
\end{array}
\begin{array}{c}
\langle ggg| \quad\; \langle gge| \quad\;\; \langle gee| \quad\;\; \langle eee| \\
\left(
\begin{array}{cccc}
0 & \gamma & (2+2\rho)\gamma & (3+6\rho)\gamma \\
\gamma & 0 & \gamma & (2+2\rho)\gamma \\
(2+2\rho)\gamma & \gamma & 0 & \gamma \\
(3+6\rho)\,\gamma & (2+2\rho)\gamma & \gamma & 0
\end{array}
\right),
\end{array}
\qquad (6.35)
$$

or more generally, for a $(n+1)$-level ladder system

$$
\boldsymbol{\gamma}_{\text{ph}} =
\begin{array}{c}
\\
|0\rangle \\
|1\rangle \\
\vdots \\
|n\rangle
\end{array}
\begin{array}{c}
\langle 0| \qquad\quad \langle 1| \quad\;\; \cdots \qquad \langle n| \\
\left(
\begin{array}{cccc}
0 & \gamma & \cdots & (n+n(n-1)\rho)\gamma \\
\gamma & 0 & \ddots & \vdots \\
\vdots & \vdots & \ddots & \gamma \\
(n+n(n-1)\rho)\gamma & \cdots & \gamma & 0
\end{array}
\right),
\end{array}
\qquad (6.36)
$$
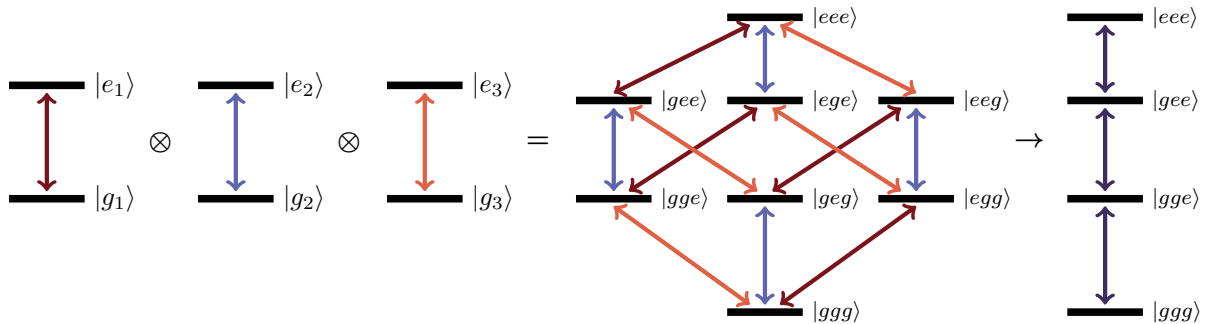
Figure 6.7: Three two-level systems combining to form a eight-level system, which we can represent as a four-level ladder system.

Note that we are once again ignoring coherences which do not occur in a valid n-quantum scan, such as $|gge\rangle\langle eeg|$ and $|gge\rangle\langle egg|$.

Alternatively, if we ensure that the 2nd through nth interactions occur simultaneously, and the $n+1$th through $2n-1$th interactions also occur simultaneously, then we can again represent the system by a $(n+1)$-level ladder system, even with differing values for the correlation coefficients $\rho_{a\neq b}$. The reason for this additional condition is that coherences such as $|gee\rangle\langle ggg|$ and $|eeg\rangle\langle ggg|$ would have different dephasing rates, while being represented by a single coherence under the four-level ladder system. However, if we require certain interactions to occur simultaneously, then there is only phase evolution during one-quantum and n-quantum coherences, so these dephasing ambiguities are irrelevant. The one-quantum coherences are not affected by ρ, since there is no correlation for a single transition. For the n-quantum coherence, we have

$$\gamma_{|e\cdots e\rangle\langle g\cdots g|} = \left(n + 2\sum_{a\neq b}\rho_{a,b}\right)\gamma. \tag{6.37}$$

6.3.3 n-Quantum Simulations

The simulations for the n-quantum spectra will be quite similar to the double-quantum spectra in Section 6.2.2. In particular, the linewidth along the emission frequency axis is determined by the rate of dephasing during the t time delay, and its corresponding lineshape is again described by Equation 6.33. Similarly, the linewidth along the n-quantum axis is determined by the rate of dephasing during the T time delay, and we can write its corresponding lineshape using Equation 6.37,

$$I_T(\omega) = \left(\left(\frac{\omega - n\omega_{eg}}{\left(n + 2\sum_{a\neq b}\rho_{a,b}\right)\gamma}\right)^2 + 1\right)^{-1/2}. \tag{6.38}$$

With this in mind, we can analyze the results for various values of n.

First we will consider no correlation, so $\rho_{a,b} = 0$ for all $a \neq b$. In this case, we see that

the n-quantum dephasing rate is simply $n\gamma$, and scales linearly with n. Simulated spectra for this case are shown in Figure 6.8 (a). The displayed spectra look identical because the n-quantum frequency axes are scaled at the same rate as the n-quantum dephasing rate. It is worth noting that this agrees with the experimental results of Reference [72], in which the decoherence rate is found to scale linearly with atom number as shown in Figure 6.9 (a). However, this experimental measurement also contains other sources of decoherence.

The next simplest case to consider is positive correlation, where all $\rho_{a,b} > 0$ and are equal for all $a \neq b$. Here, the n-quantum dephasing rate is $(n + n(n-1)\rho)\gamma$, which is notably quadratic in n. This can be seen in Figure 6.8 (b), which plots simulated spectra with $\rho = 1$. The quadratic nature is more easily seen when plotting the n-quantum dephasing rate as
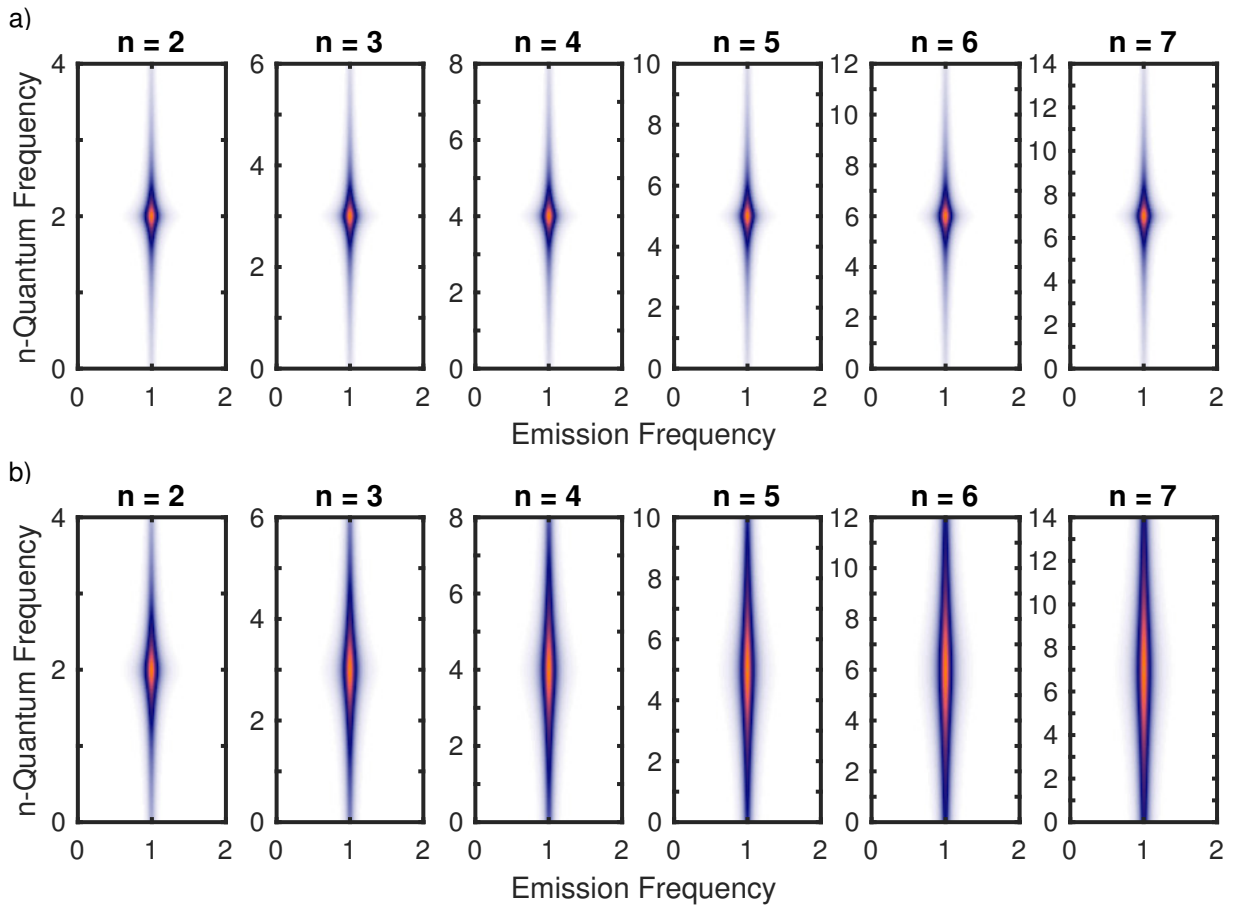
Figure 6.8: Simulated n-quantum spectra at a variety of values of n, with (a) $\rho = 0$ and (b) $\rho = 1$.
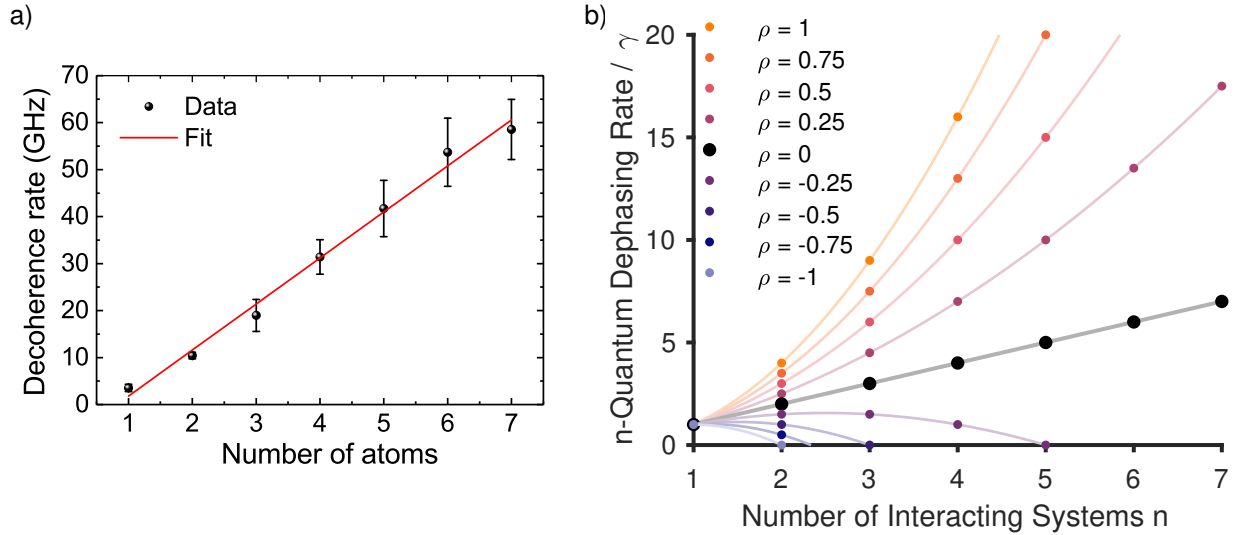
Figure 6.9: (a) A plot of the experimental measurement of the decoherence rate as a function of n, figure reproduced from Reference [72]. (b) A similar plot for the theoretic dephasing rate, relative to γ. Curves corresponding to $n + n\,(n-1)\,\rho$ are included to improve readability.

a function of n, as is seen in Figure 6.9 (b). An instance of correlated dephasing could be verified using a similar plot of experimental data. In particular, there is no clear evidence for correlated dephasing measured in Reference [72], due to the linear relationship in Figure 6.9 (a).

Figure 6.9 (b) also gives us some insight into the anticorrelated case. Recall from Section 6.1.3 that the covariance matrix must be positive semi-definite. We find that, if all $\rho_{a,b}$ are equal, this is true if

$$
\begin{aligned}
n + n\,(n-1)\,\rho &\geq 0 \\
\rho &\geq -\frac{1}{n-1.}
\end{aligned}
$$
(6.39)

Note that in Figure 6.9, if $\rho < -\frac{1}{n-1.}$, the n-quantum dephasing rate would be negative, which does not make physical sense. We also see that for a given n, we can find $\rho = -\frac{1}{n-1}$ such that the n-quantum dephasing rate equals zero and the linewidth of the coherence becomes arbitrarily small.

We can also consider the case where the $\rho_{a,b}$ are not equal. The linewidth is still given by Equation 6.37. However, note that setting

$$n + 2 \sum_{a \neq b} \rho_{a,b} \geq 0 \tag{6.40}$$

is not by itself sufficient to ensure the covariance matrix is positive semi-definite. For instance,

$$\mathbf{R} = \begin{pmatrix} 1 & -1 & -1 \\ -1 & 1 & 0.5 \\ -1 & 0.5 & 1 \end{pmatrix} \tag{6.41}$$

does satisfy Equation 6.40, but is not positive semi-definite.

If we take care to ensure the covariance matrix is positive semi-definite, we still can find valid matrices for which the n-quantum dephasing rate is zero and the values of $\rho_{a,b}$ are different. One such example is

$$\mathbf{R} = \begin{pmatrix} 1 & 1 & -1 & -1 \\ 1 & 1 & -1 & -1 \\ -1 & -1 & 1 & 1 \\ -1 & -1 & 1 & 1 \end{pmatrix}. \tag{6.42}$$

Note that this satisfies

$$n + 2 \sum_{a \neq b} \rho_{a,b} = 0. \tag{6.43}$$

For any valid covariance matrix in which the above relation is satisfied, the linewidth of the double-quantum coherence can in theory be arbitrarily small regardless of the dephasing rate due to scattering events.

6.4   Conclusion and Outlook

We have found a mathematical model that can describe correlations between Markovian scattering events, and can calculate dephasing rates due to correlated scattering events. This model was applied to view how correlated dephasing affects double-quantum and higher-order n-quantum spectra. We saw that correlations have a direct effect on the linewidth along the n-quantum axis.

The main result that should be highlighted is that anticorrelated dephasing can reduce the linewidth along the n-quantum axis. In particular, there exist configurations where the theoretical linewidth is arbitrarily small, although in practice the linewidth would be limited by other sources of dephasing.

One possible application of this work is in quantum sensing. One limit to the sensitivity of a quantum sensor is the decoherence time of the system [16]. If an appropriate anti-correlated system can be found or engineered, possibly by controlling the distance between the individual interacting systems, the ensemble could be used to improve the sensitivity or reduce the sensing time of a quantum sensor.

CHAPTER 7

Conclusion

This thesis investigated two projects using MDCS, one experimental and one theoretical. MDCS is an incredibly useful technique due to its combined power and flexibility. It is excellent at untangling complicated systems and a single MDCS spectrum, and such a spectrum can contain information that would typically require multiple measurements using more traditional techniques.

The first result we discussed concerns experimental measurements of the SiV center in diamond [5]. We used MDCS to identify the peaks in complicated spectra. We associated the different families of spectral peaks to different orientations of SiV centers separated by strain in the sample. Then we used the locations of these peaks combined with preexisting strain equations [45] to calculate the strain local to our laser spot. We did measure a non-zero strain which varied slightly at different points across the sample.

We did not purposely apply any strain to the diamond. We suspect the strain in the sample may be due to the implantation and annealing processes, especially because our sample has a high implantation density. In the future, it would be interesting to measure the spectra and strain of a sample with varying implantation density to investigate the possible relationship between strain and implantation density further. This may require improving the sensitivity of the measurement.

We also briefly discussed some double-quantum spectra of the SiV center [14]. These measurements allowed us to observe dipole-dipole coupling between nearby SiV centers.

By adding a pre-pulse before the MDCS pulses, we also demonstrated the ability to tune these interactions. This is another measurement that would be interesting to repeat with a variable density sample, since it would allow us to measure the strength of the interactions as a function of the average distance between adjacent SiV centers. It would also be interesting to take higher-order n-quantum spectra of these systems to observe interactions between more than two SiV centers.

Later, we discussed the simulation software written for the theoretical results in this thesis. This simplicity and flexibility of this code is designed to make it easy to use on a wide variety of problems. Ideally, it could continue to be used to simulate MDCS, and by including explanations about how to use the code in this thesis, I hope to encourage this.

This code was used to simulate double-quantum and higher-order n-quantum MDCS spectra of interacting systems with correlated dephasing. We developed a mathematical model describing different types of correlations and how they affect the dephasing rate of a collection of systems. These results were then integrated into simulations of spectra. Generally, we found that correlated dephasing typically results in a broadening of the spectral peak along the n-quantum frequency axis, and anticorrelated dephasing typically results in a narrowing of the spectral peak along the n-quantum frequency axis. We also found that there exist correlations with arbitrarily long dephasing times, or arbitrarily narrow spectral peaks, although in practice other sources of dephasing would limit the linewidth.

An ideal next step would be to try to confirm these results experimentally. Comparing the linewidths of n-quantum spectra for varying values of n would be useful in identifying different amounts and types of correlations. It may be desirable to try to engineer ensembles of interacting systems with the desired properties. An ensemble with anticorrelated dephasing could be useful in creating more sensitive quantum sensors, as anticorrelated dephasing can lengthen the dephasing time of the n-quantum coherence.

We have seen that both the results in this thesis use MDCS to further the field of quantum sensing. In particular, the experimental work uses SiV centers in diamond as a strain

gauge, and the theoretical work suggests a possible way to improve the sensitivity of quantum sensors. Both the topics of MDCS and quantum sensing remain exciting areas of research. Researchers are still finding new ways to use or advance MDCS techniques, and such techniques are increasingly available to researchers to study new and novel materials. New methods of quantum sensing continue to be developed, and old methods continue to be improved. The ideas presented in this thesis are built on top of the ideas of many other researchers. I hope that the projects I have worked on while completing this work continue on through the further advancement of these fields and the inspiration new ideas.

APPENDIX A

Elements of the Rotated Strain Tensor

In this appendix, we give the rotated strain tensor elements needed in Chapter 4. These are computed using the rotations from Equation 3.2.

For the two in-plane SiV centers we can compute

$$\varepsilon' = R_y\left(-\phi\right)\varepsilon R_y\left(\phi\right), \tag{A.1}$$

which gives

$$
\begin{aligned}
\epsilon'_{xx} &= \tfrac{1}{3}\epsilon_{xx} + \tfrac{2}{3}\epsilon_{zz} - \tfrac{2\sqrt{2}}{3}\epsilon_{zx}, &\qquad
\epsilon'_{xy} &= \tfrac{\sqrt{3}}{3}\epsilon_{xy} - \tfrac{\sqrt{6}}{3}\epsilon_{yz}, \\
\epsilon'_{yy} &= \epsilon_{yy}, &\qquad
\epsilon'_{yz} &= \tfrac{\sqrt{6}}{3}\epsilon_{xy} + \tfrac{\sqrt{3}}{3}\epsilon_{yz}, \\
\epsilon'_{zz} &= \tfrac{2}{3}\epsilon_{xx} + \tfrac{1}{3}\epsilon_{zz} + \tfrac{2\sqrt{2}}{3}\epsilon_{zx}, &\qquad
\epsilon'_{zx} &= \tfrac{\sqrt{2}}{3}\epsilon_{xx} - \tfrac{\sqrt{2}}{3}\epsilon_{zz} - \tfrac{1}{3}\epsilon_{zx},
\end{aligned}
\tag{A.2}
$$

and we can compute

$$\varepsilon' = R_z\left(\pi\right)R_y\left(\phi\right)\varepsilon R_y\left(-\phi\right)R_z\left(-\pi\right), \tag{A.3}$$

which gives

$$
\begin{aligned}
\epsilon'_{xx} &= \tfrac{1}{3}\epsilon_{xx} + \tfrac{2}{3}\epsilon_{zz} + \tfrac{2\sqrt{2}}{3}\epsilon_{zx}, &\qquad
\epsilon'_{xy} &= \tfrac{\sqrt{3}}{3}\epsilon_{xy} + \tfrac{\sqrt{6}}{3}\epsilon_{yz}, \\
\epsilon'_{yy} &= \epsilon_{yy}, &\qquad
\epsilon'_{yz} &= \tfrac{\sqrt{6}}{3}\epsilon_{xy} - \tfrac{\sqrt{3}}{3}\epsilon_{yz}, \\
\epsilon'_{zz} &= \tfrac{2}{3}\epsilon_{xx} + \tfrac{1}{3}\epsilon_{zz} - \tfrac{2\sqrt{2}}{3}\epsilon_{zx}, &\qquad
\epsilon'_{zx} &= \tfrac{\sqrt{2}}{3}\epsilon_{xx} - \tfrac{\sqrt{2}}{3}\epsilon_{zz} + \tfrac{1}{3}\epsilon_{zx}.
\end{aligned}
\tag{A.4}
$$

For the two out-of-plane SiV centers we can compute

$$\varepsilon' = R_z\left(\tfrac{\pi}{2}\right) R_x\left(-\phi\right) \varepsilon R_x\left(\phi\right) R_z\left(-\tfrac{\pi}{2}\right), \tag{A.5}$$

which gives

$$\epsilon'_{xx} = \tfrac{1}{3}\epsilon_{yy} + \tfrac{2}{3}\epsilon_{zz} + \tfrac{2\sqrt{2}}{3}\epsilon_{yz}, \qquad\qquad \epsilon'_{xy} = -\tfrac{\sqrt{3}}{3}\epsilon_{xy} - \tfrac{\sqrt{6}}{3}\epsilon_{zx},$$

$$\epsilon'_{yy} = \epsilon_{xx}, \qquad\qquad \epsilon'_{yz} = -\tfrac{\sqrt{6}}{3}\epsilon_{xy} + \tfrac{\sqrt{3}}{3}\epsilon_{zx}, \tag{A.6}$$

$$\epsilon'_{zz} = \tfrac{2}{3}\epsilon_{yy} + \tfrac{1}{3}\epsilon_{zz} - \tfrac{2\sqrt{2}}{3}\epsilon_{yz}, \qquad\qquad \epsilon'_{zx} = \tfrac{\sqrt{2}}{3}\epsilon_{yy} - \tfrac{\sqrt{2}}{3}\epsilon_{zz} + \tfrac{1}{3}\epsilon_{yz},$$

and we can compute

$$\varepsilon' = R_z\left(-\tfrac{\pi}{2}\right) R_x\left(\phi\right) \varepsilon R_x\left(-\phi\right) R_z\left(\tfrac{\pi}{2}\right), \tag{A.7}$$

which gives

$$\epsilon'_{xx} = \tfrac{1}{3}\epsilon_{yy} + \tfrac{2}{3}\epsilon_{zz} - \tfrac{2\sqrt{2}}{3}\epsilon_{yz}, \qquad\qquad \epsilon'_{xy} = -\tfrac{\sqrt{3}}{3}\epsilon_{xy} + \tfrac{\sqrt{6}}{3}\epsilon_{zx},$$

$$\epsilon'_{yy} = \epsilon_{xx}, \qquad\qquad \epsilon'_{yz} = -\tfrac{\sqrt{6}}{3}\epsilon_{xy} - \tfrac{\sqrt{3}}{3}\epsilon_{zx}, \tag{A.8}$$

$$\epsilon'_{zz} = \tfrac{2}{3}\epsilon_{yy} + \tfrac{1}{3}\epsilon_{zz} + \tfrac{2\sqrt{2}}{3}\epsilon_{yz}, \qquad\qquad \epsilon'_{zx} = \tfrac{\sqrt{2}}{3}\epsilon_{yy} - \tfrac{\sqrt{2}}{3}\epsilon_{zz} - \tfrac{1}{3}\epsilon_{yz}.$$

These elements can be plugged into Equation 3.7 to give the twelve strain equations in the crystal basis, as described in Section 4.2.2.

APPENDIX B

Simulating Inhomogeneous Broadening

This appendix will further discuss the function `SimulateMDScan`, whose basic implementation was the topic of Section 5.2. In particular, we will discuss the simulation of inhomogeneous broadening in MDCS spectra.

B.1 Using the Simulator

As mentioned in Section 5.2.1, `SimulateMDScan` has a fifth, optional argument, `inhom`. Inhomogeneous broadening is only included in the simulation if all five arguments are included in the function call. The argument `inhom` should be a structure array with three fields.

In order to understand the fields of `inhom`, we must make the distinction between the possible energy states, and the base frequency differences for the system. A similar distinction is made at the start of Section 6.2.1. The possible energy states are represented by the nodes in the `graph` defined in Section 5.1.1, and used to describe the rows and columns of `Omega` defined in Section 5.2.1. The base frequency differences are a set of frequencies that can be used to calculate the relative frequencies of each of the different energy states. For a simple example, this set of frequency differences may be the set of frequency differences between each excited state and a single ground state, or the set of the frequency differences between each state (excited or ground) and a single arbitrary frequency. However, this is not the only possibility. For instance, a diamond-shaped four-level system can be due to the interactions between two two-level systems, as in Figure 2.9. In this case, the frequency

difference between the doubly excited state and the ground state is approximately the sum of the two frequency differences between each singly excited state and the ground state. The differences due to interactions are not necessary to include here, since `inhom` will concern correlations between these frequency differences, rather than their actual values. Thus, for the diamond-shaped four-level system, the set of frequency differences could consist of only the two frequency differences between each singly excited state and the ground state.

The first field of the structure array `inhom` is the correlation matrix `rho`, where the rows and columns correspond to the base frequency differences. Note that this is analogous to the correlation matrix defined in Equation 6.23, except here the correlations concern the frequencies of the interacting systems (as in Reference [42]) while Chapter 6 concerns correlations in dephasing rates.

The second field of `inhom` is a vector array `sigma` of the inhomogeneous linewidths of the base frequency differences. If we convert `sigma` to a diagonal matrix, then the matrix product `diag(sigma) * rho * diag(sigma)` should be positive semi-definite, analogously to the covariance matrix defined in Equation 6.22.

The final field of `inhom` is an array `key` used to convert between the possible energy states, and the base frequency differences. The columns should correspond to the possible energy states, and the rows should correspond to the base frequency differences.

To better understand this array, we will consider a few examples. First, we consider the V-shaped three-level system in Figure B.1 (a). We can define two base frequency differences, $E_{e_1} - E_g$ and $E_{e_2} - E_g$. In this case, we will set

$$
\texttt{key} =
\begin{array}{c}
\\
E_{e_1} - E_g \\
E_{e_2} - E_g
\end{array}
\begin{array}{ccc}
|g\rangle & |e_1\rangle & |e_2\rangle \\
\left(\begin{array}{ccc}
0 & 1 & 0 \\
0 & 0 & 1
\end{array}\right)
\end{array}. \tag{B.1}
$$

Next, we consider the diamond-shaped four-level system in Figure B.1 (b). We can define
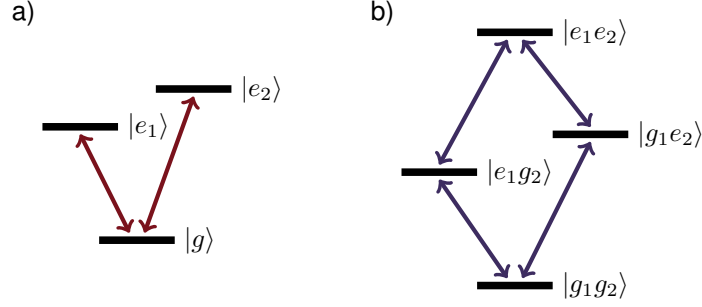
Figure B.1: (a) A V-shaped three-level system. (b) A diamond-shaped four-level system.

two base frequency differences, $E_{e_1g_2} - E_{g_1g_2}$ and $E_{g_1e_2} - E_{g_1g_2}$. In this case, we will set

$$\texttt{key} = \begin{array}{c} \\ E_{e_1g_2} - E_{g_1g_2} \\ E_{g_1e_2} - E_{g_1g_2} \end{array} \begin{array}{cccc} |g_1g_2\rangle & |e_1g_2\rangle & |g_1e_2\rangle & |e_1e_2\rangle \\ \left(\begin{array}{cccc} 0 & 1 & 0 & 1 \\ 0 & 0 & 1 & 1 \end{array} \right) \end{array}. \tag{B.2}$$

In this example, note that the last column represents the doubly excited state, which is found by summing the two singly excited states.

As an example, we will simulate an inhomogeneously broadened V-shaped three-level system. First, some of the code is identical to the homogeneously broadened example in Sections 5.1.1 and 5.2.1, and is reproduced here for convenience

```
% Generate Feynman diagrams
graph = digraph([1,1],[2,3]);
graph.Nodes.Name = {'0' '1' '2'}';
eta = [-1 1 1 -1];
feyn = FeynmanFinderFunc('0','0',graph,eta,1);
% Initialize simulation parameters
axtau = (0:2000-1)/3;
axt   = (0:2000-1)/3;
ts = [{axtau} {0} {axt}];
```

```
freqs = [0 0.67 1.33];

gamma =  0.04;

Omega = ((freqs' - freqs) - 1i * gamma);
```

Next, we need to initialize the structure array `inhom`

```
r = 1;

inhom.rho = [1 r; r 1];

inhom.sigma = 0.12 * ones(N,1);

inhom.key = deph.key;
```

Finally, we can perform the simulation using

```
res = SimulateMDScan(ts,feyn,Omega,graph,inhom);
```

We can plot the resulting spectra as in Section 5.1.1.

Figure B.2 plots some example simulated inhomogeneously spectra for several correlation values r. The correlation affects the crosspeaks, since it represents correlation between multiple frequency differences. For $r < 0$, the crosspeaks blur due to the complex phase of the peaks.
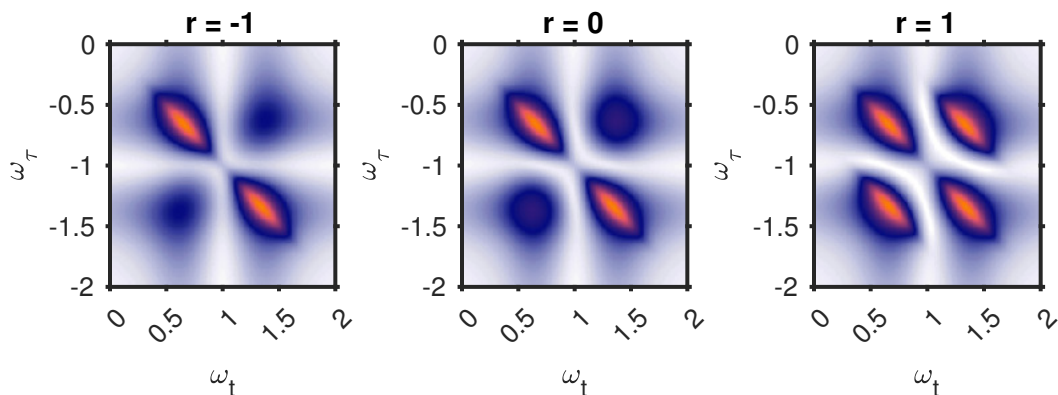

Figure B.2: The result of a simulation of a V-shaped three-level system with inhomogeneous broadening, with a variety of correlation values r.

B.2 Theoretical Background

A more rigorous mathematical treatment of inhomogeneous broadening can be found in Reference [38], and the calculated lineshape for double-quantum spectra can be found in Reference [42].

For our purposes, it will be simplest to think of inhomogeneous broadening as a convolution of a spectral peak in the frequency domain with a multivariate Gaussian function. Let $\boldsymbol{\omega}$ represent values along the frequency axes (for instance, $\boldsymbol{\omega} = \left(\begin{smallmatrix} \omega_\tau \\ \omega_t \end{smallmatrix} \right)$ could be used for a rephasing spectrum, and $\boldsymbol{\omega} = \left(\begin{smallmatrix} \omega_T \\ \omega_t \end{smallmatrix} \right)$ could be used for a two-quantum spectrum). Then we can write the homogeneous spectral signal as $s_{\text{single}}(\boldsymbol{\omega})$ and the multivariate Gaussian function as

$$f(\boldsymbol{\omega}) = \sqrt{\frac{(2\pi)^k}{\det \boldsymbol{\Sigma}}} \exp\left(-\frac{1}{2}\boldsymbol{\omega}^T \boldsymbol{\Sigma}^{-1} \boldsymbol{\omega} \right) \tag{B.3}$$

with covariance matrix $\boldsymbol{\Sigma}$. The inhomogeneous spectral signal is therefore the multivariate convolution

$$s_{\text{ensemble}}(\boldsymbol{\omega}) = (s_{\text{single}} * f)(\boldsymbol{\omega}). \tag{B.4}$$

The covariance matrix $\boldsymbol{\Sigma}$ is defined similarly to that in Equation 6.22, and is still required to be positive semi-definite. It can be different for the different peaks (defined by different Feynman diagrams) within a single spectrum, and is determined by frequencies of the coherences during each time delay, and how they are correlated.

For instance, consider a rephasing spectrum for the three level system in Figure B.1 (a). There will be two on-diagonal peaks, and two off-diagonal peaks. For the on-diagonal peaks, the probed coherences are the same, and are therefore the frequencies are perfectly correlated. Thus, if the inhomogeneous linewidth is σ_1, then

$$\boldsymbol{\Sigma} = \begin{pmatrix} \sigma_1 & 0 \\ 0 & \sigma_1 \end{pmatrix} \begin{pmatrix} 1 & 1 \\ 1 & 1 \end{pmatrix} \begin{pmatrix} \sigma_1 & 0 \\ 0 & \sigma_1 \end{pmatrix}. \tag{B.5}$$

The correlation of the off-diagonal peaks depends on the system, as the frequencies can be uncorrelated, correlated, or anti-correlated. Thus, if the inhomogeneous linewidths of the two on-diagonal peaks are σ_1 and σ_2, then

$$\Sigma = \begin{pmatrix} \sigma_1 & 0 \\ 0 & \sigma_2 \end{pmatrix} \begin{pmatrix} 1 & r \\ r & 1 \end{pmatrix} \begin{pmatrix} \sigma_1 & 0 \\ 0 & \sigma_2 \end{pmatrix}. \tag{B.6}$$

for any $-1 \leq r \leq 1$, and the results for $r = -1$, $r = 0$, and $r = 1$ are shown in Figure B.2.

Double-quantum spectra are more complicated. Let the inhomogeneous broadening for the two individual single-quantum coherences be σ_1 and σ_2. The frequency along the ω_T axis is approximately the sum of the two single-quantum frequencies, and the frequency along the ω_t axis corresponds to one of single-quantum frequencies (depending on the specific Feynman diagram used). In this case, (assuming the peak frequency along the ω_t axis is $\omega_1 = \omega_{e_1 g_2} - \omega_{g_1 g_2}$)

$$\Sigma = \begin{pmatrix} \sigma_1^2 + 2r\sigma_1\sigma_2 + \sigma_2^2 & \sigma_1^2 + r\sigma_1\sigma_2 \\ \sigma_1^2 + r\sigma_1\sigma_2 & \sigma_1^2 \end{pmatrix}, \tag{B.7}$$

in agreement with Reference [42]. We can rewrite this as the product

$$\Sigma = \begin{pmatrix} \sigma_1 & \sigma_2 \\ \sigma_1 & 0 \end{pmatrix} \begin{pmatrix} 1 & r \\ r & 1 \end{pmatrix} \begin{pmatrix} \sigma_1 & \sigma_1 \\ \sigma_2 & 0 \end{pmatrix}. \tag{B.8}$$

Note that $\begin{pmatrix} 1 & r \\ r & 1 \end{pmatrix}$ is not the correlation matrix corresponding to this covariance matrix, since $\begin{pmatrix} \sigma_1 & \sigma_1 \\ \sigma_2 & 0 \end{pmatrix}$ and its transpose $\begin{pmatrix} \sigma_1 & \sigma_2 \\ \sigma_1 & 0 \end{pmatrix}$ are not diagonal. However, it is the correlation matrix in the basis of the base frequency differences (rho in Section B.1). The matrix $\begin{pmatrix} \sigma_1 & \sigma_1 \\ \sigma_2 & 0 \end{pmatrix}$ and its transpose serve to add the inhomogeneous linewidths and convert between the basis of frequency axes $\begin{pmatrix} \omega_T \\ \omega_t \end{pmatrix}$, and the basis of the base frequency differences $\begin{pmatrix} \omega_1 \\ \omega_2 \end{pmatrix}$. For instance, the first column of $\begin{pmatrix} \sigma_1 & \sigma_1 \\ \sigma_2 & 0 \end{pmatrix}$ is $\begin{pmatrix} \sigma_1 \\ \sigma_2 \end{pmatrix}$, since the peak along the ω_T axis is approximately located at $\omega_1 + \omega_2$. Similarly, the second column of $\begin{pmatrix} \sigma_1 & \sigma_1 \\ \sigma_2 & 0 \end{pmatrix}$ is $\begin{pmatrix} \sigma_1 \\ 0 \end{pmatrix}$, since the peak along the ω_t axis is

located at ω_1 for this Feynman diagram.

Next, we return to Equation B.4. So far, we have been working in the frequency domain, but the existing code for `SimulateMDScan` is in the time domain. To convert back to the time domain, we will take an inverse Fourier transform. The inverse Fourier transform of a convolution is equal to the product of the inverse Fourier transforms of the individual functions. Thus,

$$
\begin{aligned}
S_{\text{ensemble}}(\mathbf{t}) &= \mathcal{F}^{-1}\left(s_{\text{ensemble}}(\boldsymbol{\omega})\right) \\
&= \mathcal{F}^{-1}\left(\left(s_{\text{single}} * f\right)(\boldsymbol{\omega})\right) \\
&= \mathcal{F}^{-1}\left(s_{\text{single}}(\boldsymbol{\omega})\right) \cdot \mathcal{F}^{-1}\left(f(\boldsymbol{\omega})\right) \\
&= S_{\text{single}}(\mathbf{t}) \cdot F(\mathbf{t}),
\end{aligned}
\tag{B.9}
$$

where the homogeneous spectral signal and the inhomogeneously broadened spectral signal in the time domain are $S_{\text{single}}(\mathbf{t})$ and $S_{\text{ensemble}}(\mathbf{t})$ respectively, and $F(\mathbf{t})$ is the inverse Fourier transform of Equation B.3, or

$$
F(\mathbf{t}) = \exp\left(-\frac{1}{2}\mathbf{t}^T\boldsymbol{\Sigma}\mathbf{t}\right).
\tag{B.10}
$$

Thus, to compute an inhomogeneously broadened spectrum, we will simply multiply the calculated signal at each time step by Equation B.10.

B.3   Implementation

Before we can compute the Fourier transformed Gaussian, $F(\mathbf{t})$, for each Feynman diagram, we need to find $\boldsymbol{\Sigma}$. It can be computed from the correlation matrix of the base frequency differences, `inhom.rho`, similarly to Equation B.8. We will define a new matrix `sigma` (which is distinct from the structure array field `inhom.sigma`), such that our desired matrix $\boldsymbol{\Sigma}$ or `Sigma` can be computed as

```
Sigma = sigma' * inhom.rho * sigma
```

This new matrix `sigma` is built up column by column using `inhom.sigma` and `inhom.key`.

Next, we can compute the Fourier transformed Gaussian itself. We want it to be computed at each time step in the cell array `ts`, so that it is an N-dimensional array like the output `res`. Because of the necessary combination of matrix multiplication and cell arrays, a custom function is used to do this. Each row and column of `Sigma` corresponds to one of the time axes in `ts`. This function will iterate over these rows `k` and columns `l` to compute the pointwise product

```
ts{k} .* Sigma(k,l) .* ts{l}
```

and sum these products for each `k` and `l`. We can easily compute Equation B.10 from the result, and multiply it by the calculated signal `resn` for the corresponding Feynman diagram.

The parts of `SimulateMDScan` which compute inhomogeneous broadening are contained within a couple conditional statements. To summarize the above, and show how these additions fit into the existing code, we will rewrite the pseudocode summarizing `SimulateMDScan` from Section 5.2.3, but include lines for the inhomogeneous calculations.

```
for each axis in ts
    reshape each axis so it is a vector array along the nth dimension
end
res = initialized array of zeros
sigma = initialized array of zeros
for each Feynman diagram in feyn
    resn = initialized array of ones
    for each of N-1 interactions (excluding emitted signal)
        % Compute using values from this row of this Feynman diagram
        set nth column of sigma  % From inhom.sigma and inhom.key
        resn = resn * (i * zeta * exp(-i * Omega * nth axis))
```

```matlab
    end

    % Compute using values from this emitted signal

    resn = i * zeta * resn

    res = res + resn * computed F(t)
end
```

BIBLIOGRAPHY

[1] I. D. Abella, N. A. Kurnit, and S. R. Hartmann, "Photon echoes," *Phys. Rev.* **141** (1966) 391–406.

[2] C. F. Araujo, M. M. Nolasco, A. M. Ribeiro, and P. J. Ribeiro-Claro, "Identification of microplastics using Raman spectroscopy: latest developments and future prospects," *Water Res.* **142** (2018) 426–440.

[3] N. W. Ashcroft and N. D. Mermin, *Solid State Physics.* Harcourt, 1st ed., 1976. ISBN: 0-03-083993-9.

[4] C. G. Atkins, K. Buckley, M. W. Blades, and R. F. Turner, "Raman spectroscopy of blood and blood components," *Appl. Spectrosc.* **71** (2017) 767–793.

[5] K. M. Bates, M. W. Day, C. L. Smallwood, R. C. Owen, T. Schröder, E. Bielejec, R. Ulbricht;, and S. T. Cundiff, "Using silicon-vacancy centers in diamond to probe the full strain tensor," *J. Appl. Phys.* **130** (2021) 024301.

[6] J. N. Becker and C. Becher, "Coherence properties and quantum control of silicon vacancy color centers in diamond," *Phys. Status Solidi A* **214** (2017) 1700586.

[7] J. N. Becker and E. Neu, "The silicon vacancy center in diamond," *Semicond. and Semimet.* **103** (2020) 201–235.

[8] C. N. Borca, A. G. V. Spivey, and S. T. Cundiff, "Anomalously fast decay of the LH-HH exciton Raman coherence," *Phys. Status Solidi B* **238** (2003) 521–524.

[9] J. Cai, F. Jelezko, and M. B. Plenio, "Hybrid sensors based on colour centres in diamond and piezoactive layers," *Nat. Commun.* **5** (2014) 4065.

[10] D. Charbonneau, T. M. Brown, R. W. Noyes, and R. L. Gilliland, "Detection of an extrasolar planet atmosphere," *Astrophys. J.* **568** (2002) 377–384.

[11] C. D. Clark, H. Kanda, I. Kiflawi, and G. Sittas, "Silicon defects in diamond," *Phys. Rev. B* **51** (1995) 16681–16688.

[12] S. T. Cundiff and S. Mukamel, "Optical multidimensional coherent spectroscopy," *Phys. Today* **66** (2013) 44–49.

[13] G. Davies and M. F. Hamer, "Optical studies of the 1.945 eV vibronic band in diamond," *Proc. R. Soc. Lond. A* **348** (1976) 285âĂŞ–298.

[14] M. W. Day, K. M. Bates, C. L. Smallwood, , R. C. Owen, T. Schröder, E. Bielejec, R. Ulbricht, and S. T. Cundiff, "Coherent interactions between silicon-vacancy centers in diamond," *Phys. Rev. Lett.* **128** (2022) 203603.

[15] P. Deák, A. Gali, B. Aradi, and T. Frauenheim, "Accurate gap levels and their role in the reliability of other calculated defect properties," *Phys. Status Solidi B* **248** (2011) 790–798.

[16] C. L. Degen, F. Reinhard, and P. Cappellaro, "Quantum sensing," *Rev. Mod. Phys.* **89** (2017) 035002.

[17] S. Dhomkar, P. R. Zangara, J. Henshaw, and C. A. Meriles, "On-demand generation of neutral and negatively charged silicon-vacancy centers in diamond," *Phys. Rev. Lett.* **120** (2018) 117401.

[18] M. W. Doherty, N. B. Manson, P. Delaney, F. Jelezko, J. Wrachtrup, and L. C. Hollenberg, "The nitrogen-vacancy colour centre in diamond," *Phys. Rep.* **528** (2013) 1–45.

[19] E. A. Ekimov and M. V. Kondrin, "Vacancy-impurity centers in diamond: prospects for synthesis and applications," *Phys.-Uspekhi* **60** (2017) 539–558.

[20] A. Faraon, P. E. Barclay, C. Santori, K.-M. C. Fu, and R. G. Beausoleil, "Resonant enhancement of the zero-phonon emission from a colour centre in a diamond cavity," *Nat. Photonics* **5** (2011) 301–305.

[21] K. B. Ferrio and D. G. Steel, "Raman quantum beats of interacting excitons," *Phys. Rev. Lett.* **80** (1998) 786–789.

[22] J. Fraunhofer, "Bestimmung des Brechungs- und des Farbenzerstreungs-Vermögens verschiedener Glasarten, in Bezug auf die Vervollkommnung achromatischer Fernröhre," *Ann. Phys.* **56** (1817) 264âĂŞ–313.

[23] G. D. Fuchs, G. Burkard, P. V. Klimov, and D. D. Awschalom, "A quantum memory intrinsic to single nitrogen-vacancy centres in diamond," *Nat. Phys.* **7** (2011) 789–793.

[24] A. Gali and J. R. Maze, "*Ab initio* study of the split silicon-vacancy defect in diamond: electronic structure and related properties," *Phys. Rev. B* **88** (2013) 235205.

[25] J. P. Goss, R. Jones, S. J. Breuer, P. R. Briddon, and S. Öberg, "The twelve-line 1.682 eV luminescence center in diamond and the vacancy-silicon complex," *Phys. Rev. Lett.* **77** (1996) 3041–3044.

[26] B. L. Green, M. W. Doherty, E. Nako, N. B. Manson, U. F. S. D'Haenens-Johansson, S. D. Williams, D. J. Twitchen, and M. E. Newton, "Electronic structure of the neutral silicon-vacancy center in diamond," *Phys. Rev. B* **99** (2019) 161112.

[27] Y. Guo, Y. Feng, and L. Zhang, "Revealing the growth mechanism of SiV centers in chemical vapor deposition of diamond," *Diam. Relat. Mater.* **61** (2016) 91–96.

[28] A. Gut, *An Intermediate Course in Probability*. Springer, 1st ed., 1995. ISBN: 978-0-387-94507-1.

[29] P. Hamm and M. Zanni, *Concepts and Methods of 2D Infrared Spectroscopy*. Cambridge University Press, 2011. ISBN: 978-1-107-00005-6.

[30] C. Hepp, T. Müller, V. Waselowski, J. N. Becker, B. Pingault, H. Sternschulte, D. Steinmüller-Nethl, A. Gali, J. R. Maze, M. Atatüre, and C. Becher, "Electronic structure of the silicon vacancy color center in diamond," *Phys. Rev. Lett.* **112** (2014) 036405.

[31] S. Hsieh, P. Bhattacharyya, C. Zu, T. Mittiga, T. J. Smart, F. Machado, B. Kobrin, T. O. Höhn, N. Z. Rui, M. Kamrani, S. Chatterjee, S. Choi, M. Zaletel, V. V. Struzhkin, J. E. Moore, V. I. Levitas, R. Jeanloz, and N. Y. Yao, "Imaging stress and magnetism at high pressures using a nanoscale quantum sensor," *Science* **366** (2019) 1349–1354.

[32] R. Kalish, A. Reznik, K. W. Nugent, and S. Prawer, "The nature of damage in ion-implanted and annealed diamond," *Nucl. Instrum. Methods Phys. Res. B* **148** (1999) 626–633.

[33] S. Kang, K. Kim, B. H. Kim, J. Kim, K. I. Sim, J.-U. Lee, S. Lee, K. Park, S. Yun, T. Kim, A. Nag, A. Walters, M. Garcia-Fernandez, J. Li, L. Chapon, K.-J. Zhou, Y.-W. Son, J. H. Kim, H. Cheong, and J.-G. Park, "Coherent many-body exciton in van der Waals antiferromagnet NiPS$_3$," *Nature* **583** (2020) 785–789.

[34] C. Kurtsiefer, S. Mayer, P. Zarda, and H. Weinfurter, "Stable solid-state source of single photons," *Phys. Rev. Lett.* **85** (2000) 290–293.

[35] S. Lagomarsino, A. M. Flatae, H. Kambalathmana, F. Sledz, L. Hunold, N. Soltani, P. Reuschel, S. Sciortino, N. Gelli, M. Massi, C. Czelusniak, L. Giuntini, , and M. Agio, "Creation of silicon-vacancy color centers in diamond by ion implantation," *Front. Phys.* **8** (2021) 601362.

[36] A. R. Lang, "Causes of birefringence in diamond," *Nature* **213** (1967) 248–251.

[37] D. Le Sage, K. Arai, D. R. Glenn, S. J. DeVience, L. M. Pham, L. Rahn-Lee, M. D. Lukin, A. Yacoby, A. Komeili, and R. L. Walsworth, "Optical magnetic imaging of living cells," *Nature* **496** (2013) 486âĂŞ–489.

[38] H. Li, B. Lomsadze, G. Moody, C. Smallwood, and S. Cundiff, *Optical Multidimensional Coherent Spectroscopy*. Oxford University Press, 2023. ISBN: 978-0-19-284386-9.

[39] H. Li and S. T. Cundiff, "2D coherent spectroscopy of electronic transitions," *Adv. At. Mol. Opt. Phys.* **66** (2017) 1–48.

[40] D. Liang and H. Li, "Optical two-dimensional coherent spectroscopy of many-body dipole-dipole interactions and correlations in atomic vapors," *J. Chem. Phys.* **154** (2021) 214301.

[41] B. Lomsadze and S. T. Cundiff, "Frequency combs enable rapid and high-resolution multidimensional coherent spectroscopy," *Science* **357** (2017) 1389–1391.

[42] B. Lomsadze and S. T. Cundiff, "Line-shape analysis of double-quantum multidimensional coherent spectra," *Phys. Rev. A* **102** (2020) 043514.

[43] J. Lüttig, S. Mueller, P. Malý, J. J. Krich, and T. Brixner, "Higher-order multidimensional and pump-probe spectroscopies," *J. Phys. Chem. Lett.* **14** (2023) 7556–âĹŠ7573.

[44] R. Maiwald, D. Leibfried, J. Britton, J. C. Bergquist, G. Leuchs, and D. J. Wineland, "Stylus ion trap for enchanced access and sensing," *Nat. Phys.* **5** (2009) 551âĂŞ–554.

[45] S. Meesala, Y.-I. Sohn, B. Pingault, L. Shao, H. A. Atikian, J. Holzgrafe, M. Gündoğan, C. Stavrakas, A. Sipahigil, C. Chia, R. Evans, M. J. Burek, M. Zhang, L. Wu, J. L. Pacheco, J. Abraham, E. Bielejec, M. D. Lukin, M. Atatüre, and M. Lončar, "Strain engineering of the silicon-vacancy center in diamond," *Phys. Rev. B* **97** (2018) 205444.

[46] K. Momma and F. Izumi, "*VESTA3* for three-dimensional visualization of crystal, volumetric and morphology data," *J. Appl. Crystallogr.* **44** (2011) 1272–1276.

[47] G. Moody, R. Singh, H. Li, I. A. Akimov, M. Bayer, D. Reuter, A. D. Wieck, and S. T. Cundiff, "Correlation and dephasing effects on the non-radiative coherence between bright excitons in an InAs QD ensemble measured with 2D spectroscopy," *Solid State Commun.* **163** (2013) 65–69.

[48] S. Mukamel, *Principles of Nonlinear Optical Spectroscopy*. Oxford University Press, 1995. ISBN: 0-19-509278-3.

[49] G. Nardin, T. M. Autry, K. L. Silverman, and S. T. Cundiff, "Multidimensional coherent photocurrent spectroscopy of a semiconductor nanostructure," *Opt. Express* **21** (2013) 28617–28627.

[50] E. Neu, D. Steinmetz, J. Riedrich-Möller, S. Gsell, M. Fischer, M. Schreck, and C. Becher, "Single photon emission from silicon-vacancy colour centres in chemical vapour deposition nano-diamonds on iridium," *New J. Phys.* **13** (2011) 025012.

[51] I. Newton, *Opticks: or, A treatise of the reflections, refractions, inflexions and colours of light*. Printed for Sam. Smith, and Benj. Walford, London, 1704.

[52] T. L. Purz, B. T. Hipsley, E. W. Martin, R. Ulbricht, and S. T. Cundiff, "Rapid multiplex ultrafast nonlinear microscopy for material characterization," *Opt. Express* **30** (2022) 45008–45019.

[53] T. L. Purz, E. W. Martin, W. G. Holtzmann, P. Rivera, A. Alfrey, K. M. Bates, H. Deng, X. Xu, and S. T. Cundiff, "Imaging dynamic exciton interactions and coupling in transition metal dichalcogenides," *J. Chem. Phys.* **156** (2022) 214704.

[54] LIGO Collaboration, "A gravitational wave observatory operating beyond the quantum shot-noise limit," *Nat. Phys.* **7** (2011) 962âĂŞ–965.

[55] L. J. Rogers, K. D. Jahnke, M. W. Doherty, A. Dietrich, L. P. McGuinness, C. Müller, T. Teraji, H. Sumiya, J. Isoya, N. B. Manson, and F. Jelezko, "Electronic structure of the negatively charged silicon-vacancy center in diamond," *Phys. Rev. B* **89** (2014) 235101.

[56] P. A. Rose and J. J. Krich, "Automatic Feynman diagram generation for nonlinear optical spectroscopies and application to fifth-order spectroscopy with pulse overlaps," *J. Chem. Phys.* **154** (2021) 034109.

[57] P. A. Rose and J. J. Krich, "Efficient numerical method for predicting nonlinear optical spectroscopies of open systems," *J. Chem. Phys.* **154** (2021) 034108.

[58] J. J. Sakurai and J. Napolitano, *Modern Quantum Mechanics*. Addison-Wesley, 2nd ed., 1994. ISBN: 978-0-8053-8291-4.

[59] M. Sergent III, M. O. Scully, and J. Willis E. Lamb, *Laser Physics*. Westview Press, 6th ed., 1993. ISBN: 0-201-06718-8.

[60] C. L. Smallwood, T. M. Autry, and S. T. Cundiff, "Analytical solutions to the finite-pulse Bloch model for multidimensional coherent spectroscopy," *J. Opt. Soc. Am. B* **34** (2017) 419–429.

[61] C. L. Smallwood and S. T. Cundiff, "Multidimensional coherent spectroscopy of semiconductors," *Laser Photonics Rev.* **12** (2018) 1800171.

[62] C. L. Smallwood, R. Ulbricht, M. W. Day, T. Schröder, K. M. Bates, T. M. Autry, G. Diederich, E. Bielejec, M. E. Siemens, and S. T. Cundiff, "Hidden silicon-vacancy centers in diamond," *Phys. Rev. Lett.* **126** (2021) 213601.

[63] D. D. Sukachev, A. Sipahigil, C. T. Nguyen, M. K. Bhaskar, R. E. Evans, F. Jelezko, and M. D. Lukin, "Silicon-vacancy spin qubit in diamond: a quantum memory exceeding 10 ms with single-shot state readout," *Phys. Rev. Lett.* **119** (2017) 223602.

[64] J. M. Taylor, P. Cappellaro, L. Childress, L. Jiang, D. Budker, P. R. Hemmer, A. Yacoby, R. Walsworth, and M. D. Lukin, "High-sensitivity diamond magnetometer with nanoscale resolution," *Nat. Phys.* **4** (2008) 810–816.

[65] P. F. Tekavec, G. A. Lott, and A. H. Marcus, "Fluorescence-detected two-dimensional electronic coherence spectroscopy by acousto-optic phase modulation," *J. Chem. Phys.* **127** (2007) 214307.

[66] M. E. Trusheim and D. Englund, "Wide-field strain imaging with preferentially aligned nitrogen-vacancy centers in polycrystalline diamond," *New J. Phys.* **18** (2016) 123023.

[67] A. G. VanEngen Spivey, C. N. Borca, and S. T. Cundiff, "Correlation coefficient for dephasing of light-hole excitons and heavy-hole excitons in GaAs quantum wells," *Solid State Commun.* **145** (2008) 303–307.

[68] N. H. Wan, T.-J. Lu, K. C. Chen, M. P. Walsh, M. E. Trusheim, L. De Santis, E. A. Bersin, I. B. Harris, S. L. Mouradian, I. R. Christen, E. S. Bielejec, and D. Englund, "Large-scale integration of artificial atoms in hybrid photonic circuits," *Nature* **583** (2020) 226âĂŞ–231.

[69] C. Wang, C. Kurtsiefer, H. Weinfurter, and B. Burchard, "Single photon emission from SiV centres in diamond produced by ion implantation," *J. Phys. B* **39** (2006) 37–41.

[70] W. H. Wollaston, "A method of examining refractive and dispersive powers, by prismatic reflection," *Philos. Trans. R. Soc.* **92** (1802) 365âĂŞ–380.

[71] L. Yang and S. Mukamel, "Two-dimensional correlation spectroscopy of two-exciton resonances in semiconductor quantum wells," *Phys. Rev. Lett.* **100** (2008) 057402.

[72] S. Yu, M. Titze, Y. Zhu, X. Liu, and H. Li, "Observation of scalable and deterministic multi-atom dicke states in an atomic vapor," *Opt. Lett.* **44** (2019) 2795–2798.

[73] A. M. Zaitsev, "Vibronic spectra of impurity-related optical centers in diamond," *Phys. Rev. B* **61** (2000) 12909–12922.

[74] L. Zhang, Z. Zhang, F. Wu, D. Wang, R. Gogna, S. Hou, K. Watanabe, T. Taniguchi, K. Kulkarni, T. Kuo, S. R. Forrest, and H. Deng, "Twist-angle dependence of moiré excitons in WS_2/$MoSe_2$ heterobilayers," *Nat. Commun* **11** (2020) 5888.